Design and Simulation for the Fabrication of Integrated Semiconductor Optical Logic Gates

by

Aleksandra Markina

S.B., Massachusetts Institute of Technology (1999)
S.M., Massachusetts Institute of Technology (2001)

Submitted to the
Department of Electrical Engineering and Computer Science
in partial fulfillment of the requirements for the degree of

Doctor of Philosophy in Electrical Engineering

at the

MASSACHUSETTS INSTITUTE OF TECHNOLOGY

September 2005

Author ....
Department of Electrical Engineering and Computer Science
September 19, 2005

Certified by ....
Leslie A. Kolodziejski
Professor of Electrical Engineering
Thesis Supervisor

Accepted by ....
Arthur C. Smith
Chair, Department Committee on Graduate Students

Design and Simulation for the Fabrication of Integrated Semiconductor Optical Logic Gates

by

Aleksandra Markina

Submitted to the
Department of Electrical Engineering and Computer Science
in partial fulfillment of the requirements for the degree of
Doctor of Philosophy in Electrical Engineering

ABSTRACT

Development of ultrafast all-optical logic requires accurate and efficient modeling of optical components and interfaces. In this research, we present an all-optical logic unit cell with complete Boolean functionality as a representative circuit for modeling and optimization of monolithically integrated components. Proposed optical logic unit cell is based on an integrated balanced Mach-Zehnder interferometer (MZI) with semiconductor optical amplifiers (SOAs) in each arm and includes straight ridge waveguides, ridge waveguide bends, and multimode interference (MMI) devices.

We use beam propagation method (BPM) to model, design and optimize dilute ridge waveguides, MMIs, and asymmetric twin waveguide (ATG) adiabatic taper couplers. We assess device robustness with respect to variations in fabrication, including lateral pattern transfer and etching. Bending losses in curved waveguides are evaluated using complex-frequency leaky mode computations with perfectly matched layer (PML) boundary conditions. Finite difference time domain (FDTD) method with PML is utilized in calculating reflections produced by abrupt interfaces, including a tip of an adiabatic taper coupler. We demonstrate that evaluating reflections based on local effective indices on two sides of the junction offers a simple, accurate, and time-efficient alternative to FDTD. We show a strategy for development of SOAs for linear amplification and phase shifting using the same layered semiconductor structure. Our model of optical pulse propagation in SOA is based on rate equations for carrier density and photon density and using a wavelength-dependent parametric model for gain. We demonstrate a tradeoff between injection current density and device length for both linear and non-linear SOAs.

Thesis Supervisor: Professor Leslie A. Kolodziejski
Title: Professor of Electrical Engineering

ACKNOWLEDGEMENTS

I am grateful to my research advisor Professor Leslie Ann Kolodziejski for an opportunity to work on research projects in her lab. Her patient support and guidance extended far beyond the area of molecular beam epitaxy and semiconductor optical devices. In addition to her virtues as a supervisor, I would like to thank her for bringing together a group of most friendly, gracious, and helpful individuals I had a pleasure to work with. I hope at some point in my future professional life to be part of the team of colleagues half as wonderful.

This work would not be a success without the tireless support of Dr. Gale Petrich. His willingness to sacrifice his time and to share his vast expertise with graduate students does much to brighten many of their days.

I am indebted to Professor Rajeev Ram for his guidance and invaluable insights, especially crucial in my study of semiconductor optical amplifiers. I would also like to thank Professor Erich Ippen and Dr. Scott Hamilton for valuable discussions of all-optical signal processing.

The following people made significant contributions to various parts of my research project. Professor Vinod Menon helped me to get started with the simulations of taper couplers. Miloš Popović shared his script for calculating modes of leaky dielectric structures, making calculation of losses in bent waveguides possible. Dmitry Vasilyev was of immense help with his Matlab wizardry. Fuwan Gan performed FDTD calculations of reflections from abrupt semiconductor interfaces.

It was my honor and my pleasure to work alongside graduate students of Integrated Devices and Materials Group. Solomon Assefa was a fellow physics undergrad. During our graduate studies he shared with me his contagious energy and optimism. Reginald Bryant was my neighbor both in the office and, for almost a year, in the dorm as a fellow GRT. I was grateful to Reggie for all those times we spent working quietly on our projects as well as those time when we distracted ourselves with a conversation. I truly enjoyed his sense of humor. Eric Mattson joined us briefly in our office, and his fellowship was very welcome as well. Sheila Tandon inspired me with her focus and hard work. Thanks and wishes of good luck go to Ryan Williams, my main collaborator on the optical logic unit cell project.

Many thanks are due to my family for their patience, support, encouragement, and help. Everything I ever achieved I owe to my parents, Anatoliy and Vera. It is also hard to overestimate the support I always receive from my extended family as well as my husband's: Michael's parents, Boris and Yelena, and all of our grandparents and relatives. My grandfather Leonid should be especially noted for taking full care of my family in the final week of my graduate work. Michael and I enjoy the loyalty and help of many wonderful friends who are like family to us here in Boston, none more than Kathryn Myer who adopted me as her sister.

I am indebted to my husband Michael for his unyielding support of my graduate studies as well as his exquisite skill with Microsoft Office tools which he generously shared with me in the preparation of this document and my defense presentation. Michael accompanied me on my entire MIT journey. A little less than a year ago we were joined by our daughter, Xenia. I was delighted to have her constantly by my side in the final chapter of my MIT saga.

TABLE OF CONTENTS

TABLE OF FIGURES

1 Introduction

1.1 Motivation

Currently, network services impose bottlenecks on fiber optic communications. While network management complexity increases with the number of wavelengths fibers carry, most signal processing operations, such as switching and routing, are still performed electronically after opto-electronic (OE) conversion [1, 2]. An average internet session takes 16 hops, with OE-EO conversions for electronic switching at each node. Development of ultrafast all-optical logic would make it possible to avoid multiple conversions and to distribute low-level network functionality in the optical core. High-level slow processing would then be pushed to network edges. Desired functionality of all-optical signal processing includes routing, synchronization, header processing, and cascadability [2-4]. Developing a family of optical logic with complete Boolean functionality—an optical equivalent of Transistor-Transistor Logic (TTL)—is an important step in this direction.

A fast non-linear element is required to implement optical signal processing functions. Semiconductor Optical Amplifier (SOA) represents an especially attractive choice. SOA is integrable, relatively compact, and boasts good thermal stability and high non-linearity [5]. To utilize fast nonlinear response of SOAs and mask their slow recovery, SOAs can be inserted into interferometer arms [6]. Symmetric Mach-Zehnder configurations with identical SOAs placed in each arm of Mach-Zehnder interferometer (MZI) are especially effective. When nonlinear refractive index change is induced in the two SOAs with an appropriate delay, cross-phase modulation is utilized to change the amplitude of the interferometer output [4]. MZIs with SOAs are robust and highly integrable, and thus represent a valuable platform for realization of optical signal processing functions.

A wide variety of optical components is required in order to perform every function currently carried out by electronic circuits. These include optical clocks [7, 8], polarization splitters [9-12], polarization rotators [13-15], TE/TM mode converters [16, 17], straight and bent waveguides [18-20], Semiconductor Optical Amplifiers [21-23], various filters (for example, Bragg filters [24], side coupled resonator filters [25-29], tunable Fabry-Perot filters [30, 31]), isolators [32-34], time delay components [35-39], phase shifters [40-43], multimode interference couplers [44, 45], and fiber-to-chip couplers [46-48]. As evidenced by an abundance of literature describing design, building and operation of the above components, significant progress has been achieved in creating discrete elements for future optical networks. Despite these considerable research efforts, many existing devices are bulky and barely compatible. Therefore, effective integration of optical components on a chip represents a bottleneck in all-optical circuit development.

To address the bottleneck issue we need to monolithically integrate optical logic gates. Such gates need to be easy to fabricate, robust and reliable in operation. Development of photonic integrated circuits and their components requires accurate and efficient modeling tools. In contrast to the electronic devices and circuits field, optical design field lacks standard, universal design and simulation tools.

The goal of this research is to develop and test a strategy for design of the integrated optical circuit components. This task requires mastery of a set of semiconductor device modeling tools. The challenge is to optimize the performance of each component while all the components are monolithically integrated on a semiconductor chip. The reach the goal of monolithic integration, it is crucial to develop a simulation environment for the selection of device design and performance optimization. Numerical modeling needs to address all relevant material properties, fabrication techniques and their tolerances, device performance and optimization based on tradeoffs between device parameters and performance priorities.

Device modeling serves a range of invaluable functions. First of all, it allows a designer to monitor internal variables in order to gain better understanding of device physics. Second, modeling yields an estimate of device performance without the need to build the device. Since fabrication and testing of novel semiconductor devices typically requires significant resources of time, labor, materials and equipment, accurate modeling results in significant savings. In addition, simulations provide a way to optimize device performance by varying device parameters, testing parameter range, and finding optimal operating conditions for required device functionality. Numerical modeling also helps to identify tradeoffs between device specifications and operating parameters. Once such tradeoffs are recognized, intelligent choices can be made based on the design priorities. Finally, modeling allows for robustness analysis of the design with respect to possible variations in fabrication results.

1.2 Master example—optical logic unit cell

An all-optical circuit based on Mach-Zehnder interferometer (MZI) geometry capable of performing all operations of Boolean algebra (AND, NAND, XOR) is an optical analog of Transistor-Transistor Logic (TTL). It is useful in a wide variety of applications for all-optical data processing. Such unit logic cell can be built on an optical bench from an assortment of discrete semiconductor components connected with optical fiber [49]. In order to make the circuit practical for real-world optical networks, it needs to be integrated on a semiconductor chip. An integrated implementation of the optical circuit will make the unit logic cell compact and cascadable: several unit cells can be arranged to perform more involved optical data processing.

In this work, an all-optical logic unit cell serves as a representative circuit for modeling and optimization of monolithically integrated components. Proposed optical logic unit cell is based on an integrated balanced Mach-Zehnder interferometer with an SOA in each arm (Figure 1-1). The basic version of this photonic integrated circuit consists of straight ridge waveguides, ridge waveguide bends, multimode interference (MMI) power splitters and combiners, and semiconductor optical amplifiers (SOAs). The basic implementation does not address the issues of timing, reflections, and separating multiple co-propagating wavelengths.

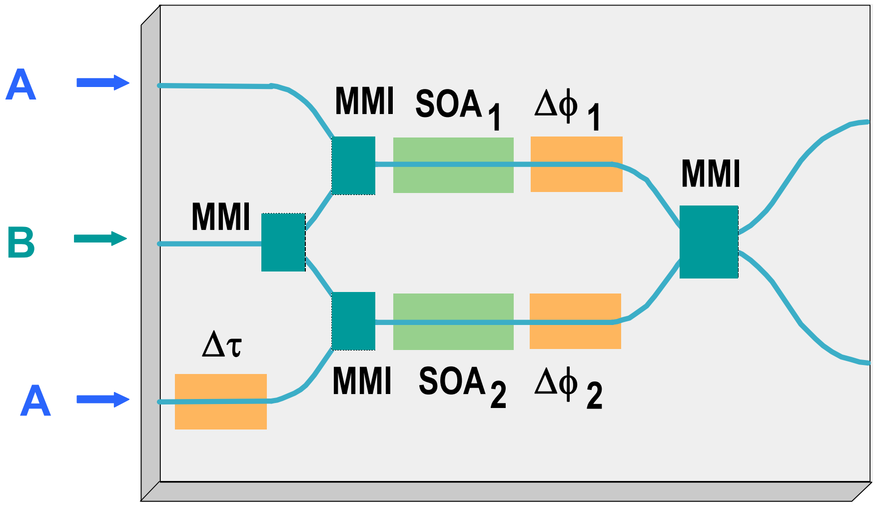

Figure 1-1. Optical logic unit cell.

1.2.1 Materials

Material system of choice for this project is (In,Ga)(As,P) grown on InP substrates. This material system has a number of advantages compared to other photonic materials such as GaAs, silicon, silica, and polymers. InGaAsP/InP has high refractive index which makes compact, high index contrast structures possible. Our chosen material system also possesses high electrical conductivity and medium thermal conductivity. Most importantly, InGaAsP/InP system offers significantly higher gain at 1.55 µm wavelength than does any other material system listed above.

$In_{1-x}Ga_xAs_yP_{1-y}$ lattice matched to InP offers a bandgap range from 0.73eV (InGaAs) to 1.35eV (InP) which makes it highly compatible with all-optical fiber networks. Quaternary material of a desired bandgap can be obtained by choosing the appropriate ratios of group III and group V elements [50]. It is necessary to identify materials with desirable properties for both passive and active devices. Passive waveguides has to be transparent to 1.55 μm light, exhibit low loss and minimal polarization sensitivity. Active device layers need to provide sufficient gain at 1.55 μm. A suitable quaternary material for an active core is $In_{0.56}Ga_{0.44}As_{0.93}P_{0.07}$ because it is lattice matched to InP and has a bandgap corresponding to 1.57 μm.

1.2.2 Fabrication

A vertical semiconductor structure is realized by a crystal growth. An epitaxial growth provides excellent control over composition and thickness of semiconductor layers. Molecular beam epitaxy (MBE) is characterized by direct physical transport of material components from effusion cells to a heated substrate wafer. The process takes place under high vacuum conditions. These conditions allow the use of various diagnostic tools and in-situ processes including thermal or ion beam cleaning, Auger electron spectroscopy, mass spectroscopy, x-ray photoelectron spectroscopy, and radiation high energy electron diffraction [50, 51]. Epitaxially-grown heterostructures form the base for the circuit design.

Lateral patterning is performed by optical lithography followed by dry and wet etching steps. Fabrication processes required for building integrated optical logic unit cell are similar to conventional III-V processing sequences. Dielectric deposition is performed by Plasma Enhanced Chemical Vapor Deposition (PECVD) or sputtering. Gold-containing metal contacts are typically deposited by electron beam evaporation. Etching techniques include reactive ion etching and wet etches [49]. Exploring fabrication tolerances is a crucial part of device modeling.

1.2.3 Device performance

Elements of the all-optical logic unit cell are chosen as representative components in our study of semiconductor device modeling for PIC design. Appropriate modeling techniques need to be chosen for each optical component. Numerical methods have to addresses crucial device phenomena, parameters, and requirements.

Passive devices have to be transparent to 1.55 μm light. Other desirable characteristics of passive components include low loss and low polarization sensitivity. The cross-section of the passive waveguide should be sufficiently large for easy coupling to an optical fiber. Waveguide bends should be as compact as possible. Multimode interference couplers are required to operate as balanced, efficient splitters and combiners.

Minimizing reflectivity is the most important design guideline for interfaces between passive and active components of the photonic integrated circuits. Low reflectivity is especially important for integrated SOAs: a reflection coefficient below 10^{-4} is needed in order to operate an SOA as a single-pass device without creating a laser cavity. In addition, robust, efficient couplers need to be designed to guide optical energy between passive and active components.

Two types of semiconductor optical amplifiers are employed in the optical logic unit cell. The first type is a linear amplifier. In this application, a linear SOA needs to provide only a moderate level of amplification with a highly linear behavior at the lowest injection current density possible. The second SOA type is a non-linear phase shift element. The non-linear SOA has to supply a π phase shift for a modest SOA length and injection current density. Both types of SOAs have to perform their functions for signals several picoseconds in lengths with energies on the order of hundreds of femtoseconds.

1.3 Overview

The following three chapters share a similar logical structure. Each chapter concentrates on one class of devices with specific applications in photonic integrated circuits. We choose appropriate numerical techniques that address crucial device characteristics. We explain the mathematical basis for modeling, including simplifying assumptions and limitations of each numerical method. Next we apply the described simulation techniques to design examples chosen among optical logic unit cell components. We discuss simulation results and their implications for device optimization, identify tradeoffs between device parameters, and in some cases examine design robustness with respect to likely imperfections in device fabrication.

In Chapter 2, we discuss passive devices: bulk and dilute ridge waveguides, curved ridge waveguides, and multimode interference (MMI) devices. We use semi-vectorial Beam Propagation Method implemented by RSoft Corporation to find confined optical modes of the waveguide structures and to study light propagation in the multimode waveguides. We demonstrate design process for the passive devices starting with a choice of passive material layers for straight ridge waveguides. This vertical structure is shared by all passive devices and therefore represents a starting point for an MMI design. We briefly present the theory of MMI devices that guides and informs our computer-aided design process for MMIs. Special attention is paid to likely imperfections in ridge waveguide and MMI fabrication and to the effect of these imperfections on simulated device performance. In addition, we survey numerical techniques for estimating losses in curved ridge waveguides and show calculations of bending losses using finite-difference method with cylindrical perfectly matched layer (PML) boundary conditions. The discussion of curved ridge waveguides also includes an optimization process for coupling junctions between waveguides of different curvature.

In Chapter 3, we address the problem of modeling interfaces between passive and active optical components. We begin with a review of main monolithic integration techniques: butt coupling, Quantum Well Disordering (QWD), and Asymmetric Twin Waveguides (ATG). Since ATG approach it employed in the design of an all-optical unit cell, we discuss the history and evolution of ATG method in some detail. We also address the physical nature of coupling through tapered waveguides. We demonstrate the optimization process for ATG tapers using BPM software and access robustness of taper couplers with respect to fabrication variations. Next, we introduce the finite difference time domain technique (FDTD) with perfectly matched layer (PML) boundary conditions for calculation of reflections from abrupt interfaces. We use FDTD with PML to determine reflections from butt-coupling interfaces as well as from the ATG taper tip. We also show that reflection coefficient can be accurately estimated based on local effective indices before and after the junction. This alternative method is considerably less time-consuming and demands far fewer computational resources.

In Chapter 4, we review physical processes behind semiconductor optical amplifier (SOA) operation. We discuss the origins of slow and fast dynamic response in an SOA and their consequences for SOA use in linear and non-linear applications. In order to highlight desirable characteristics of a linear optical amplifier, we compare SOA with an Erbium-Doped Fiber Amplifier (EDFA). Next, we mention several techniques for obtaining improved linear SOA performance, including the use of materials with a long carrier lifetime, non-uniform current injection and gain clamping. In the following sections, we switch to the discussion of SOA use in all-optical signal processing schemes. We detail two general approaches to overcoming pattern dependence in all-optical circuits employing SOAs: the use of Quantum Dot SOAs and utilization of special signal encoding methods. In the later part of Chapter 4, we present a model of light propagation in SOA based on rate equations for carrier and photon density in the device. The simulation method employs the wavelength-dependent parametric gain model and allows us to estimate gain and phase experienced by an optical pulse passing through an SOA. We use the described simulation technique to implement optimization of a linear and a non-linear SOA. We demonstrate a process for selecting SOA length and injection current density for a linear SOA which produces a desired gain and a non-linear SOA which produces a specified phase shift. Both cases reveal a tradeoff between SOA length and bias current density. As we will show, this tradeoff is important for optimization of SOA performance.

Chapter 5 contains a summary of results presented in this work. The chapter concludes with a brief discussion of future directions in semiconductor device modeling and in optical logic until cell design.

1. D. Cotter, et al., *Nonlinear Optics for High-Speed Digital Information Processing.* Science, 1999. **286**: p. 1523.

2. R.J. Manning, et al. *Recent advances in all-optical signal processing using semiconductor optical amplifiers*. 1999.

3. K. Tajima. *Ultrafast all-optical signal processing with symmetric Mach-Zehnder type all-optical switches*. 2001.

4. S. Nakamura, Y. Ueno, and K. Tajima. *Ultrahigh-speed optical signal processing with symmetric-Mach-Zehnder-type all-optical switches*. 2002.

5. B. Dagens, et al. *SOA-based devices for all-optical signal processing*. 2003.

6. K. Uchiyama and T. Morioka. *All-optical signal processing for 160 Gbit/s/channel OTDM/WDM systems*. 2001.

7. B. Sartorius, et al. *Self-pulsation at more than 20 GHz in InGaAsP/InP DFB lasers* in *Semiconductor Laser Conference* 1992.

8. S. Fischer and M.G. Dulk, E.; Vogt, W.; Gini, E.; Melchior, H.; Hunziker, W.; Nesset, D.; Ellis, A.D. , *Optical 3R regenerator for 40 Gbit/s networks* Electronics Letters 1999. **35**(11): p. 2047 -2049.

9. F. Ghirardi and J.C. Brandon, M.; Bruno, A.; Menigaux, L.; Carenco, A. , *Polarization splitter based on modal birefringence in InP/InGaAsP optical waveguides* IEEE Photonics Technology Letters, 1993. **5**(9): p. 1047 –1049.

10. F.J. Mustieles, E. Ballesteros, and F. Hernandez-Gil, *Multimodal analysis method for the design of passive TE/TM converters in integrated waveguides* IEEE Photonics Technology Letters, 1993. **5**(7): p. 809 -811.

11. J.J.G.M. van der Tol, et al., *Mode evolution type polarization splitter on InGaAsP/InP.* IEEE Photonics Technology Letters, 1993. **5**(12): p. 1412 -1414.

12. L.B. Soldano and A.I.S. de Vreede, M.K.; Verbeek, B.H.; Metaal, E.G.; Green, F.H. , *Mach-Zehnder interferometer polarization splitter in InGaAsP/InP* IEEE Photonics Technology Letters, 1994. **6**(3): p. 402 –405.

13. S. S. A. Obayya, B.M.A.R., K. T. V. Grattan and H. A. El-Mikati *Beam Propagation Modeling of Polarization Rotation in Deeply Etched Semiconductor Bent Waveguides* IEEE Photonics Technology Letters, 2001. **13**(7): p. 681-683.

14. H. Heidrich, et al., *Passive mode converter with a periodically tilted InP/GaInAsP rib waveguide* IEEE Photonics Technology Letters, 1992. **4**(1): p. 34-36.

15. C. M. Weinert and H. Heidrich, *Vectorial simulation of passive TE/TM mode converter devices on InP* IEEE Photonics Technology Letters, 1993. **5**(3): p. 324 - 326.

16. M. Schlak, et al., *Tunable TE/TM-mode converter on (001)-InP-Substrate.* IEEE Photonics Technology Letters, 1991. **3**(1): p. 15-16.

17. P. Albrecht, et al. *Polarization converter and splitter for a coherent receiver optical network on InP* in *IEE Colloquium on Polarisation Effects in Optical Switching and Routing Systems*. 1990.

18. M. Rajarajan, et al., *Characterization of low-loss waveguide bends with offset-optimization for compact photonic integrated circuits.* IEE Proceedings on Optoelectronics 2000. **147**(6): p. 382-388.

19. P. Bienstman, et al., *Calculation of Bending losses in dielectric waveguides using eigenmode expansion an perfectly matched layers.* IEEE Photonics Technology Letters, 2002. **14**(2): p. 164-166.

20. J. Singh, et al., *Single-mode low-loss buried optical waveguide bends in GaInAsP/InP fabricated by dry etching.* Electronics Letters, 1989. **25**(14): p. 899 -900.

21. S. Kitamura, et al., *Angled facet S-bend Semiconductor optical Amplifiers for high-gain and large extinction ratio.* IEEE Photonic Technology Letters 1999. **11**(7): p. 788-790.

22. A. Lestra and J.-Y. Emery, *Monolithic Integration of Spot-Size Converters with 1.3 um lasers and 1.55um polarization insensitive semiconductor optical amplifiers.* IEEE J Selected Topics in Quantum Electronics, 1997. **3**(7): p. 1429-1440.

23. K. Djordjev, S.J.C., W.J. Choi, S.J. Choi, I. Kim and P. Dapkus, *Two-segment spectrally inhomogeneous traveling wave semiconductor optical amplifiers applied to spectral equalization.* IEEE Photonic Technology Letters, 2002. **14**(5): p. 603-605.

24. M. J. Khan, et al. *Integrated Bragg grating structures*. in *Advanced Semiconductor Lasers and Applications/Ultraviolet and Blue Lasers and Their*

Applications/Ultralong Haul DWDM Transmission and Networking/WDM Components, 2001. Digest of the LEOS Summer Topical Meetings 2001.

25. M.K. Chin, et al., *GaAs microcavity channel-dropping filter based on a race-track resonator* IEEE Photonics Technology Letters, 1999. **11**(12): p. 1620 – 1622.

26. C. Manolatou, et al., *Coupling of modes analysis of resonant channel add-drop filters* Quantum Electronics, IEEE Journal of, 1999. **35**(9): p. 1322 –1331.

27. S. Fan, et al., *Channel Drop Tunneling through Localized States.* Physics Review Letters, 1998. **80**: p. 960–963.

28. P.P.Absil, et al., *Vertically coupled microring resonators using polymer wafer bonding.* IEEE Photonics Technology Letters 2001. **13**(1): p. 49 -51.

29. B.E. Little, et al., *Microring resonator arrays for VLSI photonics.* IEEE Photonics Technology Letters 2000. **12**(3): p. 323 -325.

30. N. Chitica, et al., *Monolithic InP-biased tunable filter with 10-nm bandwidth for optical data interconnects in the 1550-nm band* IEEE Photonics Technology Letters, 1999. **11**(5): p. 584 –586.

31. H.K. Tsang, et al., *Etched cavity InGaAsP-InP waveguide Fabry-Perot filter tunable by current injection.* Journal of Lightwave Technology, 1999. **17**(10): p. 1890 –1895.

32. H. Yokoi, et al., *Feasibility of integrated optical isolator with semiconductor guiding layer fabricated by wafer direct bonding* IEE Proceedings on Optoelectronics, 1999. **146**(2): p. 105 -110.

33. H. Yokoi and T. Mizumoto, *Integration of terraced laser diode and optical isolator by wafer direct bonding* Conference on Lasers and Electro-Optics Europe, 2000: p. 1.

34. M. Takenaka and Y. Nakano. *Proposal of a novel semiconductor optical waveguide isolator* in *Conference on Indium Phosphide and Related Materials*. 1999.

35. W. Ng, et al., *High-precision detector-switched monolithic GaAs time-delay network for the optical control of phased arrays* IEEE Photonics Technology Letters, 1994. **6**(2): p. 231 –234.

36. S. Yegnanarayanan, et al., *Compact silicon-based integrated optic time delays* IEEE Photonics Technology Letters, 1997. **9**(5): p. 634 –635.

37. E.J. Murphy, et al., *Guided-wave optical time delay network* IEEE Photonics Technology Letters 1996. **8**(4): p. 545 –547.

38. N.F. Hartman and L.E. Corey. *A new time delay concept using integrated optics techniques* in *Antennas and Propagation Society International Symposium*. 1991.

39. N.F. Hartman, et al. *Integrated optic time delay network for phased array antennas* in *IEEE National Radar Conference*. 1991.

40. B.H.P. Dorren, et al., *A chopped quantum-well polarization-independent interferometric switch at 1.53 um* IEEE Journal of Quantum Electronics, 2000. **36**(3): p. 317 -324.

41. J.E. Zucker, et al., *Electro-optic modulation in a chopped quantum-well electron transfer structure* Electronics Letters, 1994. **30**(6): p. 518 -520.

42. B.H.P. Dorren, et al., *Low-crosstalk penalty MZI space switch with a 0.64-mm phase shifter using quantum-well electrorefraction* IEEE Photonics Technology Letters 2001. **13**(1): p. 37 -39.

43. B.H.P. Dorren, et al., *Low-crosstalk penalty MZI space switch with a 0.64-mm phase shifter using quantum-well electrorefraction* IEEE Photonics Technology Letters, 2001. **13**(1): p. 37 -39.

44. J. Leuthold, et al., *Multimode interference couplers for the conversion and combining of zero- and first-order modes.* Journal of Lightwave Technology, 1998. **16**(7): p. 1228 –1239.

45. P.A. Besse, et al., *New 2x2 and 1x3 multimode interference couplers with free selection of power splitting ratios.* Journal of Lightwave Technology, 1996. **14**(10): p. 2286 -2293.

46. Soo-Jin Park, et al., *A novel method for fabrication of a PLC platform for hybrid integration of an optical module by passive alignment.* IEEE Photonics Technology Letters, 2002. **14**(4): p. 486-488.

47. D. Taillaert, et al., *An Out-of-Plane Grating Coupler for Efficient Butt-Coupling Between Compact Planar Waveguides and Single-Mode Fibers* Journal of Quantum Electronics, 2002. **38**(7): p. 949-955.

48. K. Kato and Y. Tohmori, *PLC hybrid integration technology and its application to photonic components* IEEE Journal on Selected Topics in Quantum Electronics, 2000. **6**(1): p. 4-13.

49. A. Markina, G. S. Petrich, and L. A. Kolodziejski, *Towards Integrated Photonic Circuits*. 2002, Research Laboratory of Electronics, Massachusetts Institute of Technology.

50. E.H.C. Parker, *The Technology and Physics of Molecular Beam Epitaxy*. 1985: Plenum Press.

51. A. Katz, *Indium Phosphide and Related Material: Processing, Technology, and Devices*. 1992: Artech House, Inc.

2 Passive Devices

2.1 Passive Ridge Waveguides

Design of ridge waveguides requires fast and accurate calculations of waveguide modes. Rigorous approach calls for solving a full set of Maxwell equations for 3D geometry. Closed-form solutions are not available; therefore numeric methods must be used. There exist a number of methods. Semi-analytical methods include Marcatili's method [52, 53], Effective Index method [54-57], Fourier transform techniques [58], the Spectral Index [59-61], and the Free Space Radiation Mode methods [62-64]. While these methods are efficient and fast, their use is limited to particular geometries. Numerical methods such as Finite Difference [65-67], Finite Element [68, 69], and Finite Difference Beam Propagation Method [70-72] are accurate, robust, and applicable to a wide range of problems [73, 74]. We chose Beam Propagation Method (BPM) for modeling of ridge waveguides because BPM is conceptually straightforward, efficient, and uses modest computational resources to yield sufficiently accurate results. It serves our simulation goals well because in most cases the computational effort is directly proportional to the number of grid points used in the numerical simulation. The beam propagation method (BPM) is the most widely used technique for modeling integrated photonics devices [75].

The BPM is a technique for approximating the exact wave equation for monochromatic waves and solving the resulting equations numerically by finite difference method. The basic approach requires assumptions of a scalar field and paraxiality. However, to insure that the switch performance is the same for TE and TM polarized light we need to use enhanced BPM. To address the issue, among available options we turn to semi-vectorial version of BPM.

The BPM technique can be applied to complex geometries without having to develop specialized versions of the method. Another advantage of BPM is that it automatically includes the effects of both guided and radiating fields as well as mode coupling and conversion. The BPM approach is extensible, that is, it allows for the inclusion of effects such as polarization and nonlinearities by extensions of the basic method.

Polarization effects can be included in the BPM by using the vector wave equation rather than the scalar Helmholtz equation. Semi-vectorial approximation is achieved by decoupling the transverse components of the electric field. As a result of this approximation, the problem is considerably simplified while retaining the most significant polarization effects. In this work, the semi-vectorial BPM is used.

2.1.1 Beam Propagation Method

Beam Propagation Method (BPM) is a recursive procedure for calculating electro-magnetic field distribution in a plane from the field distribution in a preceding parallel plane [75, 76]. Basic approach is formulated under the restrictions of paraxiality and a scalar field. Paraxiality restricts propagation to a narrow range of angles. The scalar field assumption means that polarization effects are neglected. The scalar electric field can be written as $E(x, y, z, t) = \phi(x, y, z)e^{-j\omega t}$. The geometry of the device is completely defined by the refractive index distribution $n(x, y, z)$.

The wave equation can be stated as Helmholtz equation for monochromatic waves:

$$\frac{\partial^2 \phi}{\partial x^2} + \frac{\partial^2 \phi}{\partial y^2} + \frac{\partial^2 \phi}{\partial z^2} + k(x, y, z)^2 \phi = 0 \qquad \text{(Eq. 2-1)}$$

where the spatially-dependent wavenumber is given by $k(x, y, z) = k_0 n(x, y, z),$ with $k_0 = 2\pi / \lambda$ being the wavenumber in free space.

For most guided-wave problems, the phase variation due to propagation along the guiding axis represents the fastest variation in the field ϕ. Since paraxial approximation allows us to assume that the axis is predominantly along the *z* direction, it is possible to factor this rapid variation out by introducing a slowly varying field *u* and restating ϕ as

$$\phi(x, y, z) = u(x, y, z)e^{i\bar{k}z}, \qquad \text{(Eq. 2-2)}$$

where $\bar{k}$ is a constant that represents the average phase variation of the field ϕ. This constant is referred to as the reference wavenumber and can be expressed in terms of reference refractive index, $\bar{n}$: $\bar{k} = k_0 \bar{n}$. Substituting Eq. 2-2 into Eq. 2-1 yields the equation equivalent to the exact Helmholtz for the slowly varying field:

$$\frac{\partial^2 u}{\partial z^2} + 2i\bar{k}\frac{\partial u}{\partial z} + \frac{\partial^2 u}{\partial x^2} + \frac{\partial^2 u}{\partial y^2} + (k^2 - \bar{k}^2)u = 0. \qquad \text{(Eq. 2-3)}$$

Invoking paraxial approximation one more time, it is assumed that the variation of *u* with *z* is sufficiently slow that the first term in Eq. 2-3 is negligible compared to the second, that is, $\left|\frac{\partial^2 u}{\partial z^2}\right| << \left|2\bar{k}\frac{\partial u}{\partial z}\right|$. Eq. 2-3 is now reduced to

$$\frac{\partial u}{\partial z} = \frac{i}{2\bar{k}}\left(\frac{\partial^2 u}{\partial x^2} + \frac{\partial^2 u}{\partial y^2} + (k^2 - \bar{k}^2)u\right). \qquad \text{(Eq. 2-4)}$$

The above equation forms the basis of three-dimensional BPM and completely determines the evolution of the field for $z>0$ given an input field $u(x, y, z = 0)$. The last simplification reduces the problem from a second order boundary value problem to a first order initial value problem. While the former requires iteration or eigenvalue analysis, the latter can be solved by simple "integration" of Eq. 2-4 along the direction of propagation *z*.

Early versions of BPM employed split-step Fourier method for "integrating" parabolic partial differential equation Eq. 2-4 forward in *z*. Later an implicit finite-difference approach (FD-BPM) based on Crank-Nicholson scheme has become standard [75]. Compared to Fourier transform-based methods, FD-BPM achieves comparable accuracy using a larger step size. Another advantage is a lower computational time per step [73]. In FD-BPM, the field in the transverse (*xy*) plane is represented at discrete points. Numerical equations are used to determine the field at the next discrete plane along the propagation direction (*z*) from the discretized field at the previous z plane. First, we will illustrate this approach for a scalar field in 2D (*xz*).

Let's assume that grid points and planes are equally spaced by x and z respectively. The field at transverse grid point *i* and longitudinal plane *n* is denoted by

u_i^n. In the Crank-Nicholson method Eq. 2-4 is written for the midplane between the plane of the known field *n* and the next plane, *n+1*:

$$\frac{u_i^{n+1} - u_i^n}{\Delta z} = \frac{i}{2\bar{k}} \left(\frac{\delta^2}{\Delta x^2} + \left(k\left(x_i, z_{n+1/2}\right) \right)^2 - \bar{k}^2 \right) \frac{u_i^{n+1} + u_i^n}{2}, \qquad \text{(Eq. 2-5)}$$

where δ^2 is the second order difference operator, $\delta^2 u_i = (u_{i+1} + u_{i-1} - 2u_i)$, and $z_{n+1/2} \equiv z_n + \Delta z / 2$. When the above equation is rearranged into the form of a tridiagonal matrix equation for the unknown field u_i^{n+1} in terms of known quantities, it results in

$$a_i u_{i-1}^{n+1} + b_i u_i^{n+1} + c_i u_{i+1}^{n+1} = d_i. \qquad \text{(Eq. 2-6)}$$

Expressions for the coefficients a_i, b_i, c_i, and d_i are derived in [77]. Since Eq. 2-6 is tridiagonal, it can be solved in order *O(N)* operations, where *N* is the number of grid points in *x*.

Appropriate choice of boundary conditions is crucial for accurate BPM calculations because a poor choice can cause an artificial reflection of light from the boundary of the computational domain. Early research made use of absorbing boundary conditions (ABC) where an artificial absorbing material is placed near the edge of the domain. The ABC approach has several serious disadvantages. First of all, the absorber parameters are problem-dependent. Optimizing them for a particular problem requires significant effort and care. Moreover, in many cases, artificial reflections persist because the interface between the computational space and the artificial absorber is also partially reflective. Transparent boundary condition (TBC) was introduced to address the above problems. In the TBC approach the outgoing field is allowed to pass the domain boundary as an outgoing plane wave. The TBC approach is more versatile, robust, and requires less computer memory than the ABC. It works well for problems with narrow propagation angles. Since paraxial condition holds for most of the structures considered in this work, the TBC approach is employed wherever BPM is used [73, 75].

The direct extension of the Crank-Nicholson approach to 3D results in a system of equations that is not tridiagonal and therefore requires $O(N_x^2 \cdot N_y^2)$ operations to solve directly. A numerical approach called the alternating direction implicit (ADI) method allows the 3D problem to be solved with optimal $O(N_x \cdot N_y)$ efficiency. The ADI approach is employed by the BPM program used for this work [75].

2.1.1.1 Including polarization effects in the BPM

Polarization effects can be included by using the vector wave equation instead of the scalar Helmholtz equation. The equations for the vector electric field E can be formulated in terms of the transverse components of the field, E_x and E_y. This approach results in a set of coupled equations for the slowly varying fields u_x and u_y:

$$\frac{\partial u_x}{\partial z} = A_{xx} u_x + A_{xy} u_y \qquad \text{(Eq. 2-7)}$$

$$\frac{\partial u_y}{\partial z} = A_{yx} u_x + A_{yy} u_y \qquad \text{(Eq. 2-8)}$$

Complex differential operators A_{ij} are given by

$$A_{xx} u_x = \frac{i}{2\bar{k}} \left\{ \frac{\partial}{\partial x}\left[\frac{1}{n^2} \frac{\partial}{\partial x}\left(n^2 u_x\right)\right] + \frac{\partial^2}{\partial y^2} u_x + (k^2 - \bar{k}^2) u_x \right\} \qquad \text{(Eq. 2-9)}$$

$$A_{yy} u_y = \frac{i}{2\bar{k}} \left\{ \frac{\partial^2}{\partial x^2} u_y + \frac{\partial}{\partial y}\left[\frac{1}{n^2} \frac{\partial}{\partial y}\left(n^2 u_y\right)\right] + (k^2 - \bar{k}^2) u_y \right\} \qquad \text{(Eq. 2-10)}$$

$$A_{yx} u_x = \frac{i}{2\bar{k}} \left\{ \frac{\partial}{\partial y}\left[\frac{1}{n^2} \frac{\partial}{\partial x}\left(n^2 u_x\right)\right] - \frac{\partial^2}{\partial x \partial y} u_x \right\} \qquad \text{(Eq. 2-11)}$$

$$A_{xy}u_y = \frac{i}{2\bar{k}}\left\{\frac{\partial}{\partial x}\left[\frac{1}{n^2}\frac{\partial}{\partial y}\left(n^2 u_y\right)\right] - \frac{\partial^2}{\partial xy}u_y\right\} \qquad \text{(Eq. 2-12)}$$

The above equations are employed by full-vectorial BPM. The diagonal terms A_{xx} and A_{yy} describe different propagation constants and field shapes for TE and TM modes. These operators also account for polarization dependence due to different boundary conditions at interfaces. The off-diagonal terms A_{xy} and A_{yx} deal with polarization coupling and hybrid modes due to geometric effects. The problem can be significantly simplified by decoupling transverse field components, that is, by assuming that $A_{xx}= A_{xx}=0$. This is a so-called semi-vectorial approximation. The semi-vectorial calculation takes into account the most significant polarization effects. It is appropriate for most structures that are not specifically designed to induce coupling between TE and TM modes [75].

2.1.1.2 Mode solving with BPM

Calculation of optical modes in waveguides is the first step in most design and analysis procedures in semiconductor circuit modeling. Modes need to be determined in order to ensure single-modedness of waveguides, to calculate mode confinement, coupling length and losses. The majority of simulations presented in this work use eigenmodes of the relevant waveguide structures as input. In many cases, calculation of modes is also necessary in order to monitor evolution of optical energy within waveguide structures and transfer of energy between parts of the structures.

Code written for BPM propagation is easily adapted for mode-solving. A correlation method or an iterative method can be used. In both methods a given incident field is launched into a structure that is uniform along z. Some form of BPM propagation is employed. Since the geometry is *z*-invariant, the propagation can be described in terms of the modes of the structure. For simplicity, we will describe the use of the method for 2D scalar field with an understanding that it can be easily extended to 3D and vectorial cases. An incident $\varphi_m(x)$ field can be written in terms of the eigenmodes of the structure as follows:

$$\phi_{in}(x) = \sum_m c_m \phi_m(x) \qquad \text{(Eq. 2-13)}$$

Propagation along the structure in then expressed by

$$\phi(x,z) = \sum_m c_m \phi_m(x) e^{i\beta_m z} \qquad \text{(Eq. 2-14)}$$

When imaginary distance BPM is used, the longitudinal coordinate *z* is replaced by $z' = iz$. The propagation along the imaginary axis is given by

$$\phi(x,z') = \sum_m c_m \phi_m(x) e^{\beta_m z'} \qquad \text{(Eq. 2-15)}$$

The exponential growth of each term is equal to the respective real propagation constant. When an arbitrary field is propagated along the imaginary axis, the fundamental mode will soon dominate all other modes because the fundamental mode has the highest propagation constant. The field pattern will be equivalent to φ_0. The following expression yields the propagation constant:

$$\beta^2 = \frac{\int \phi^* \left(\frac{\partial^2 \phi}{\partial x^2} + k^2 \phi \right) dx}{\int \phi^* \phi dx} \qquad \text{(Eq. 2-16)}$$

An orthogonalization procedure can be used to subtract contribution from the fundamental mode in order to find higher order modes.

When the correlation method is used, an arbitrary field is propagated along the structure via the regular BPM technique. The following correlation function between the input field and the propagating field is calculated during the propagation:

$$P(z) = \int \phi_{in}^{*}(x)\phi(x,z)dx \qquad \text{(Eq.2-17)}$$

Substituting the expansion of the field in terms of the normal modes, the correlation function can be written as

$$P(z) = \sum_{m} |c_m|^2 e^{i\beta_m z} \qquad \text{(Eq. 2-18)}$$

A Fourier transform of the correlation function has a spectrum with peaks corresponding to the propagation constants of normal modes. The corresponding modal fields are obtained through the second propagation by beating the propagating field against the known propagation constants:

$$\phi_{in}(x) = \frac{1}{L}\int_{0}^{L} \phi(x,z)e^{-i\beta_m z} \qquad \text{(Eq. 2-19)}$$

Although the correlation method is slower than the imaginary distance BPM, it is applicable to a wider range of problems, such as the ones including leaky or radiating modes [75].

2.1.1.3 RSoft BeamPROP

RSoft BeamPROP Version 5.0 was used for layout and analysis of passive devices. RSoft BeamPROP is a widely-used photonics design and modeling tool. Other research groups have employed this tool to simulate performance of similar passive optical devices, as demonstrated in their patents and publications. In those instances, results of modeling were confirmed by experimental data.

The software combines advanced finite-difference beam propagation engine with a convenient modern graphical user interface. The package consists of two closely integrated elements. The main program includes the CAD layout system for device design as well as controls simulation features: numerical parameters, input fields, and display and analysis options. The simulation program performs the actual computation and produces a graphical display of the results. The CAD system is designed to allow for parameterization of waveguide geometry and calculation window settings as well as rapid parameter variation and analysis of waveguide properties as a function of parameters. Among other merits of RSoft BeamPROP are problem-specific, intelligent choices of default parameters and real-time analysis and display of the simulation results.

2.1.2 Main examples—Optimization of dilute ridge waveguides

Design and optimization of passive ridge waveguides included two successive approximations. First, we conducted simulations to find a range of parameters such as refractive index of bulk material and waveguide width to achieve single-mode propagation while providing large enough cross-section for fiber coupling. (Height of 1.05 μm was chosen in order to keep both the required etch depth and the ridge aspect ratio moderate. Unfortunately, we found that using bulk material was impractical because low-arsenic compositions are challenging to produce using gas source molecular beam Epitaxy (GS-MBE). Therefore, we decided to use dilute waveguide approach as described below and conducted another set of simulations to determine the choice of layers and geometry. Finally, additional calculations were performed to assess robustness of ridge waveguide design with respect to variations in quaternary material composition and etch depth.

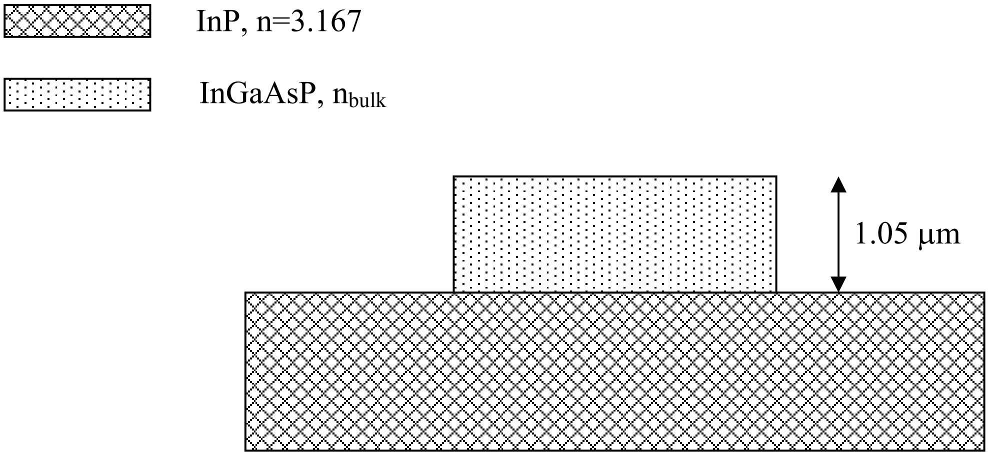

Figure 2-1. Bulk Ridge Waveguide.

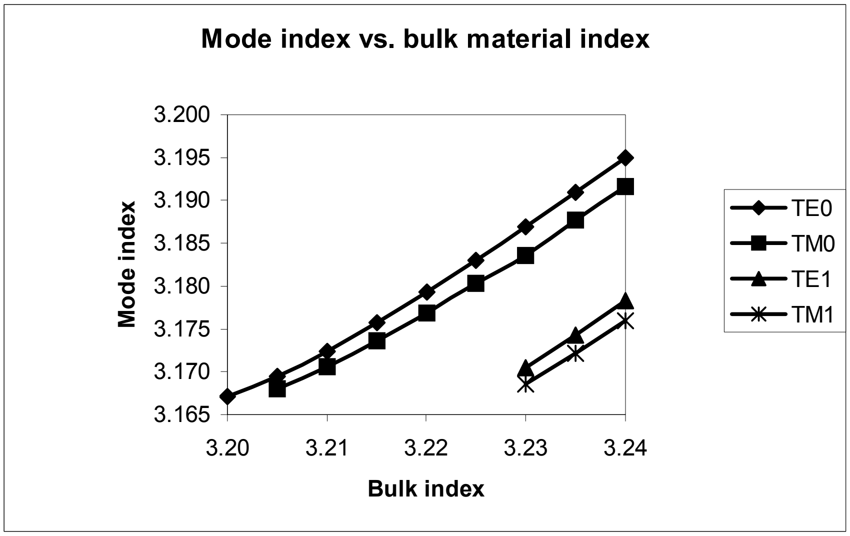

Figure 2-2. Dependence of mode effective index on bulk index in bulk ridge waveguides of cross section 4 mm x 1.05 µm.

2.1.2.1 Simulations of Bulk WGs

First we explore the modes of uniform (bulk) ridge waveguides. Figure 2-1 shows a bulk ridge waveguide. Dependence of effective indices of confined waveguide modes on the bulk material index was determined for a fixed cross-section of 4 µm width by 1.05 µm height. As illustrated by Figure 2-2, a ridge waveguide of given cross-section supports a single TE and a single TM mode for a range of bulk materials with refractive index varying approximately between 3.205 and 3.23. Choosing bulk index in the middle of this range, n_{bulk}=3.22, we explored dependence of waveguide modes on ridge width. Figure 2-3 shows that single-mode behavior is displayed by waveguides of width from over 2 μm to 4.5 μm. As seen in Figure 2-2 and Figure 2-3, ridge waveguides are not polarization insensitive, with TE modes having somewhat higher effective indices than those of TM modes.

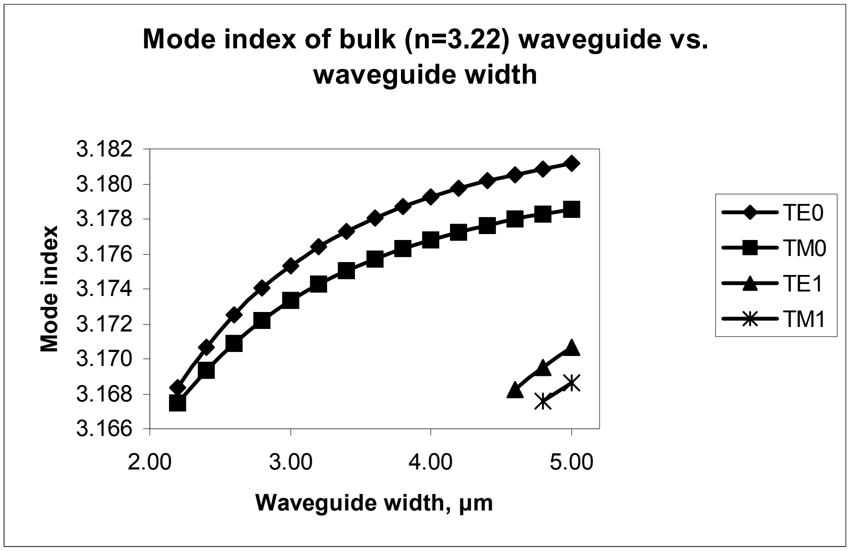

Figure 2-3. Dependence of mode effective index on ridge width in bulk ridge waveguides, bulk index 3.22 and height of 1.05 μm.

2.1.2.2 Selection of layered materials

Dilute waveguides are fabricated from InGaAsP layers interspersed by InP layers. This approach allows us to use InGaAsP material of a known, easily achievable and well-calibrated composition to build a single-mode waveguide with a large cross-section for easy coupling to fiber [78-80]. To achieve the same goal using a bulk InGaAsP requires a thick layer of quaternary material close in composition to InP. Bulk quaternary materials with very low arsenic concentration are very challenging to grow epitaxially due to a much higher tendency of arsenic atoms to stick to the substrate surface during growth than that of phosphor atoms. It is next to impossible to grow a layer of such material of the required thickness (on the order of a micron). Dilute waveguide approach addresses two issues. First, it allows us to design a ridge waveguide with a desired effective index by varying layer thicknesses rather than changing material composition. This technique offers very precise control over the effective index of the ridge waveguide. Second, the quality of the semiconductor crystal is improved by inserting InP layers between InGaAsP layers that typically have some strain due to small unintended lattice mismatch with InP.

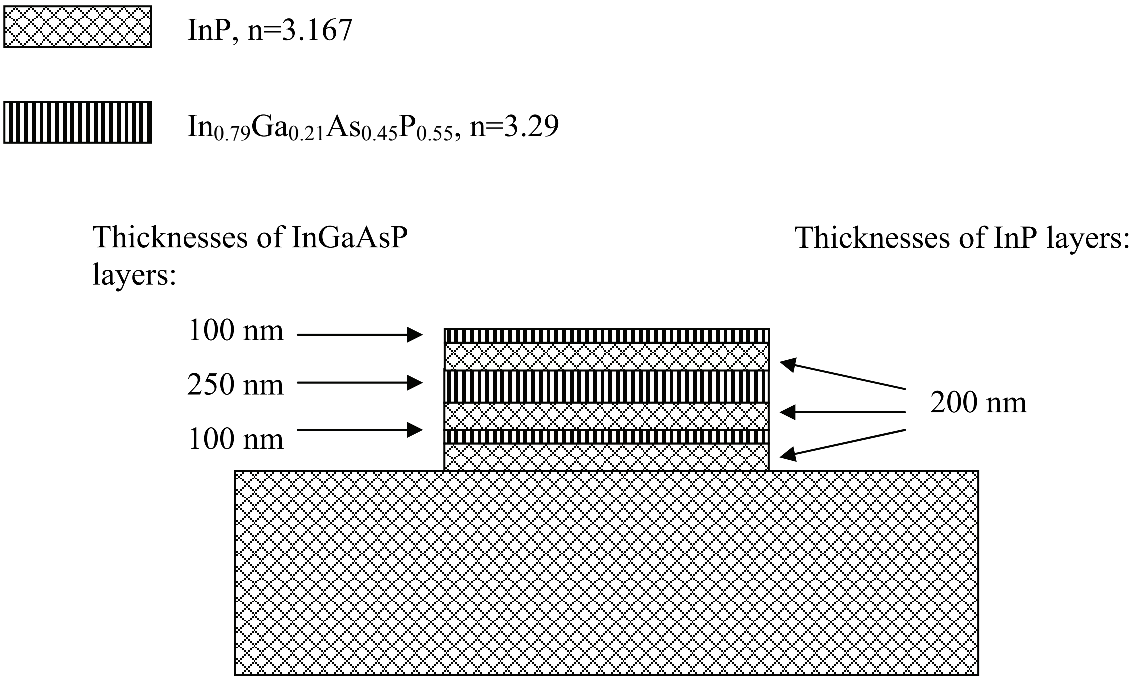

Figure 2-4. Dilute ridge waveguide design.

The layered structure designed for this project is presented in Figure 2-4. The quaternary layers of composition $In_{0.79}Ga_{0.21}As_{0.45}P_{0.55}$ and refractive index n=3.29 have thicknesses of 100 nm, 250 nm, and 100 nm. They are separated by 200 nm thick layers of InP. The layers are chosen in such a way as to produce the desired overall refractive index. Weighted square average refractive index of the six InGaAsP/InP layers, n=3.22, matches the bulk material index chosen in the previous section.

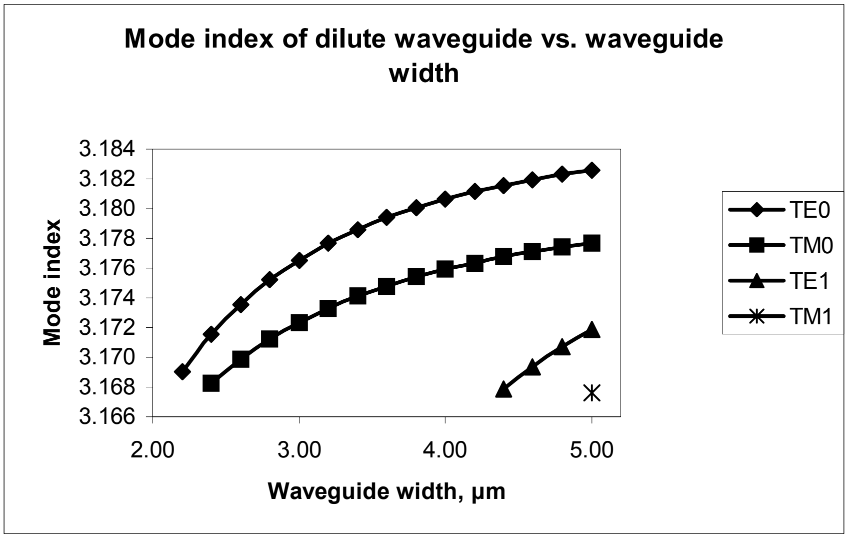

Figure 2-5. Dependence of mode effective index on ridge width in dilute ridge waveguides.

Dependence of effective indices of confined waveguide modes on waveguide width for the described layered structure are illustrated in Figure 2-5. The results are essentially similar to those for bulk waveguides of comparable dimensions. One drawback of dilute waveguides is that the discrepancy between the effective indices of TE and TM modes is increased in comparison to bulk waveguides.

2.1.2.3 Robustness of dilute ridge waveguides with respect to fabrication variations

Robustness of the dilute ridge waveguide was accessed with respect to variations arising from wafer processing. In particular, effects of InGaAsP composition and ridge etch depth were studied. The extent of likely material composition variations wav deduced from material specifications provided by IQE, the commercial supplier of epitaxial wafers. The bandgap wavelength for $In_{0.79}Ga_{0.21}As_{0.45}P_{0.55}$ material is stated as λ=1180±20 nm. This corresponds to Arsenic content between 0.413 and 0.473 and an approximate effective index variation of about ±0.011. While waveguides fabricated with most materials within this range still support only one TE and one TM mode, the materials on the far high end of the Arsenic concentration spectrum will just start to support one higher-order TE mode. This can lead to potentially undesirable behavior in ridge waveguides. If it is in fact determined that a given wafer has higher concentration of Arsenic in its quaternaries and therefore the material has a larger overall index of refraction, the problem can be remedied by fabricating narrower passive waveguides.

We also examined the effect of varying the etch depth on the effective index of confined waveguide modes. Nominal etch depth for the designed device is 1.05 µm or 1050 nm. We calculated effective indices of ridge waveguides etched to depth of 950 nm and 1150 nm, making a generous estimate of ±100 nm deviation in etch depth. The difference in effective indices between the properly etched waveguide and an underetched or overetched waveguide was found to be only on the order of 10^{-4}.

In conclusion, it was determined that effective waveguide index is highly insensitive to etch depth variation, but somewhat sensitive to variations in quaternary material composition. If material composition variation results in a higher index of the quaternary material, single-mode waveguide can still be fabricated by reducing the ridge width.

2.1.3 Passive ridge waveguides—Conclusions

Single-mode waveguides with a large cross-section were designed using dilute waveguide approach. Among the advantages of this method compared to single-layer bulk quaternary material are better material quality, greater ease of material growth, and more precise control over the overall effective index of the material. Disadvantages of dilute waveguides include a more complicated layer structure causing potential difficulties in etching and increased polarization sensitivity. Similar devices of an earlier design were fabricated with material grown in Integrated Photonic Devices and Materials Group lab by molecular beam epitaxy and were shown to support TE and TM modes.

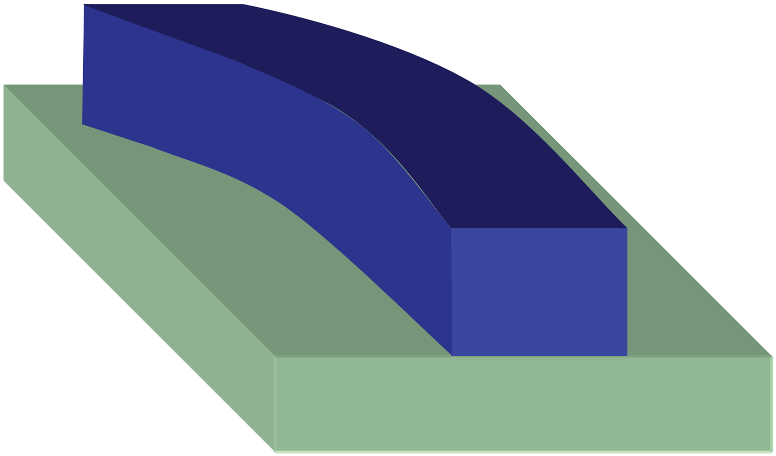

Figure 2-6. Curved ridge waveguide.

2.2 Passive waveguide bends

Bending ridge waveguides (Figure 2-6) represent an important component in photonic circuits. Since they are inherently lossy and are used nearly as often as straight waveguides, accurate modeling is imperative. Two issues in particular need to be addressed: losses due to the waveguide curvature and losses due to mode mismatch at the transition point between waveguides of different curvature. The first problem is considerably more involved and merits a detailed discussion of available methods.

To study bent waveguides numerically, either the beam propagation methods or modal solutions approach can be applied [81, 82]. Several approaches reported in the literature rely on various forms of the scalar wave equation. One method employs an index profile that varies with propagation distance. Another derives an effective index profile from a compact form of the wave equation in cylindrical coordinates. The wave equation in cylindrical coordinates has also been used with the Finite Element Method and Finite Difference BPM [81] and reference therein. Most of these approaches yield acceptable results for large bending radii.

In general, methods based on approximate equivalent straight waveguide (ESW) formulation [83] are less accurate than rigorous cylindrical coordinate system formulation [82]. It is important to note that the break of symmetry due to bending gives rise to the full vector characteristics of the modal fields. These characteristics become more pronounced for tight bends, requiring the use of full-vector formulation. In addition, the popular transparent boundary conditions are typically insufficient for accurate modal solutions for leaky structures such as curved waveguides. The perfectly matched layer (PML) boundary conditions which were originally developed for the finite-difference time-domain method [84] were adapted independently by Popovic [85] and Feng, et al. [82] to mode solvers for leaky dielectric structures.

The next section describes unsuccessful attempts to calculate losses in curved dilute waveguides using RSoft BPM tool. Theory of leaky mode solutions by finite-difference method with PML in cylindrical coordinates is presented. Finally, results of bending loss computations are obtained using the finite difference solver.

2.2.1 Attempts to assess bending losses with BPM

RSoft BPM tool offers two approaches to simulating curved waveguides: direct BPM calculation and the simulated bend technique. While direct calculation can be performed, it does not yield meaningful results for a number of reasons. First of all, direct computation requires a very large simulation domain in transverse direction. More importantly, direct simulation is limited by the paraxial limitation of BPM that typically cannot be overcome even with the Pade-based wide-angle capability of the RSoft tool. Such calculations are also of limited use for optimizing the junction coupling.

The simulated-bend feature uses coordinate transformation to map a bent waveguide onto a straight waveguide. Thus, computational domain in the transverse direction is greatly reduced and simulation is simplified. This method has proven effective in calculating a scalar approximation to the mode in the curved region. To calculate losses inherent in bent waveguide, the calculated mode is propagated along the waveguide with the respective simulated bend. The power in the waveguide is monitored with respect to the initial launched mode. In theory, power in the curved waveguide decreases exponentially at a rate that represents the bending loss. In our simulations, decay of monitored waveguide power did not follow the exponential curve, but declined slowly before entering a region of exponential-like decrease. No consistent relationship was found between the rate of decline and the bending radius. Results were found to be highly sensitive to the choice of numeric setting and therefore unreliable.

Unfortunately, neither method available in Rsoft BPM tool produced meaningful results for our 3D structure. Multiple attempts at simulation were made with a wide range of numeric settings. No set of numeric setting was found to produce consistent results. This failure is likely explained by the limited ability of transparent boundary conditions to handle leaky structure.

2.2.2 Bending loss calculation by finite-difference method with cylindrical PML

Leaky nature of the modes in bent waveguides demands a mode solver with highly effective boundary conditions. Cylindrical perfectly matched layers can be used to calculate complex-frequency leaky modes of ridge waveguide bends by finite difference methods [85, 86]. It has been demonstrated that PML computations are significantly more effective than TBC in this case [82]. Bending loss can be deduced from the imaginary part of the complex propagation constant of the mode [87].

The full-vector Maxwell equations for the transverse electric field are represented as an eigenvalue problem with squared complex frequency eigenvalue in 2D. For bent ridge waveguides, the 2D representation is a $\rho - z$ cross-section in a cylindrical coordinate system in which bending radius lies along the *r* coordinate. Since the original PML formulation based on the splitting of field components is unsuitable for deriving a wave equation [82], PML is viewed here instead as a complex coordinate-stretching transformation [88]. The following change of variable is required:

$$\tilde{\zeta} = \int_0^{\zeta} s_{\zeta}(\zeta')d\zeta', \tag{Eq. 2-20}$$

where $s_\zeta(\zeta)$ represents the complex stretching variables as in [89] and ζ stands for ρ, φ, and z in the cylindrical coordinate system. Neglecting the term designed to handle evanescent waves for frequencies below the waveguide's cutoff, the complex stretching variables are given by

$$s_{\zeta}(\zeta) = \begin{cases} 1 & in \quad the \quad non-PML \quad region \\ -\dfrac{j\sigma_{\zeta}(\zeta)}{\omega\varepsilon_0} & in \quad the \quad PML \quad region \end{cases} \tag{Eq. 2-21}$$

with

$$\sigma_{\zeta}(\zeta) = \sigma_{\zeta \max} \frac{|\zeta - \zeta_0|^m}{d^m} \qquad \text{(Eq. 2-22)}$$

where ζ_0 is the PML interface, d is the PML thickness and m is typically 2.

Full-vector wave equations in the complex cylindrical coordinate system incorporating the PML boundary condition can by written using this coordinate stretching technique:

$$\tilde{\nabla}^2 \vec{E} + \tilde{\nabla}(\vec{E} \cdot \tilde{\nabla} \ln(n^2)) + n^2 k_0^2 \vec{E} = 0 \qquad \text{(Eq. 2-23)}$$

with the operators $\tilde{\nabla}$ and $\tilde{\nabla}^2$ for the new complex coordinate system given by

$$\tilde{\nabla} = \hat{\tilde{\rho}} \frac{\partial}{\partial \tilde{\rho}} + \hat{\tilde{\phi}} \frac{1}{\tilde{\rho}} \frac{\partial}{\partial \tilde{\phi}} + \hat{\tilde{z}} \frac{\partial}{\partial z} \qquad \text{(Eq. 2-24)}$$

and

$$\tilde{\nabla}^2 = \frac{1}{\tilde{\rho}} \frac{\partial}{\partial \tilde{\rho}} \left(\tilde{\rho} \frac{\partial}{\partial \tilde{\rho}} \right) + \frac{1}{\tilde{\rho}^2} \frac{\partial^2}{\partial \tilde{\phi}^2} + \frac{\partial^2}{\partial z^2} . \qquad \text{(Eq. 2-25)}$$

In Popovic's work [85], the cylindrical finite-difference formulation is on the Yee grid as in finite-difference time-domain methods, but in the frequency domain. The spatial derivatives are approximated by finite-differencing in order to translate Maxwell's equations into the form of a matrix equation [90]. The cylindrical-geometry eigenvalue equation solved for leaky modes is written using notation developed in [91] as follows:

$$\begin{bmatrix} -\hat{\partial}_z\tilde{\partial}_z - \frac{1}{\rho^2_{m+\frac{1}{2}}}\tilde{\partial}_p \frac{\rho_m}{\varepsilon^{\phi\phi}_M}\hat{\partial}_p \rho_{m+\frac{1}{2}}\varepsilon^{\rho\rho}_M & \hat{\partial}_z \frac{1}{\rho_{m+\frac{1}{2}}}\tilde{\partial}_p \rho_m - \frac{1}{\rho^2_{m+\frac{1}{2}}}\tilde{\partial}_p \frac{\rho^2_m}{\varepsilon^{\phi\phi}_M}\hat{\partial}_z \varepsilon^{zz}_M \\ \frac{1}{\rho_m}\hat{\partial}_p \rho_{m+\frac{1}{2}}\tilde{\partial}_z - \frac{1}{\rho_m}\tilde{\partial}_z \frac{1}{\varepsilon^{\phi\phi}_M}\hat{\partial}_p \rho_{m+\frac{1}{2}}\varepsilon^{\rho\rho}_M & -\frac{1}{\rho_m}\hat{\partial}_p \rho_{m+\frac{1}{2}}\tilde{\partial}_p - \frac{1}{\rho_m}\tilde{\partial}_z \frac{\rho_m}{\varepsilon^{\phi\phi}_M}\hat{\partial}_z \varepsilon^{zz}_M \end{bmatrix} \cdot \begin{bmatrix} E^{\rho}_{m+\frac{1}{2},n} \\ E^{z}_{m,n+\frac{1}{2}} \end{bmatrix} =$$

$$= \left(\omega^2 \mu \begin{bmatrix} \varepsilon^{\rho\rho}_M & 0 \\ 0 & \varepsilon^{zz}_M \end{bmatrix} - \gamma^2 \begin{bmatrix} \frac{1}{\rho^2_{m+\frac{1}{2}}} & 0 \\ 0 & \frac{1}{\rho_m} \end{bmatrix} \right) \cdot \begin{bmatrix} E^{\rho}_{m+\frac{1}{2},n} \\ E^{z}_{m,n+\frac{1}{2}} \end{bmatrix}.$$

(Eq. 2-26)

The 2D-domain grid points are designated by M=(m,n), (m+1/2,n) or (m,n+1/2). Forward and backward differences are identified by tilde (~) and caret (^). Here γ is the angular propagation constant of a mode in the cylindrical structure, and ω is the frequency as in the time dependence $\exp(j\omega t)$. Eq. 2-26 is rearranged to isolate γ^2 on the right hand side in order to solve complex-propagation-constant eigenvalue problem for leaky modes of curved waveguides [85] and references therein.

2.2.3 Bending losses in curved dilute waveguides—Results

Matlab program used for this project in order to calculate bending losses was developed by Milos Popovic based on complex-frequency leaky mode computations using perfectly matched boundary layers (PML) as described in the preceding section. In this series of calculations, dilute ridge waveguide designs presented in Section A of this chapter were considered. The radius of curvature of the bent waveguides ranged from 100 μm to 500 μm. The results are presented in Figure 2-7. Losses due to waveguide curvature are moderate (around 1.5 dB) for bending radius of 300 μm and low (about 0.36 dB) for bending radius of 500 μm.

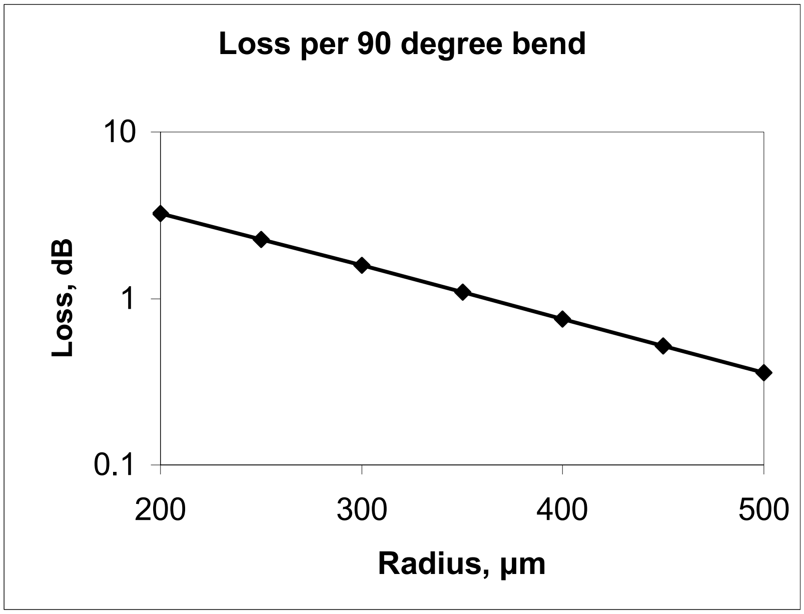

Figure 2-7. Losses in curved ridge waveguide.

2.2.4 Optimization of coupling junctions

BPM-based scalar mode solutions are sufficient for optimizing junctions between straight and bent waveguides. RSoft BeamPROP was used in this work to optimize lateral offsets between waveguides of different curvature, in particular, a straight waveguide and the two portions of an S-bend. The optimal relative position of two waveguides is achieved when overlap between their fundamental modes is maximized.

As an example, a junction between a straight waveguide and a curved waveguide with bending radius of 500 µm is optimized. (The layered structure and cross-section of the waveguides is that of a typical passive waveguide designed for this project.) Fundamental modes of the straight and curved waveguides are calculated (Figure 2-8). To simulate coupling of light from the straight waveguide into the curved waveguide, the mode of the straight waveguide is launched into the bent waveguide and overlap between the two modes is calculated by monitoring power in the mode of the bent waveguide.

This procedure is repeated over a range of lateral offsets between the two waveguides. In this case, optimal offset between the waveguide is approximately -0.4 μm (Figure 2-9). The described method can be used to optimize junction coupling between any two waveguides of arbitrary curvatures.

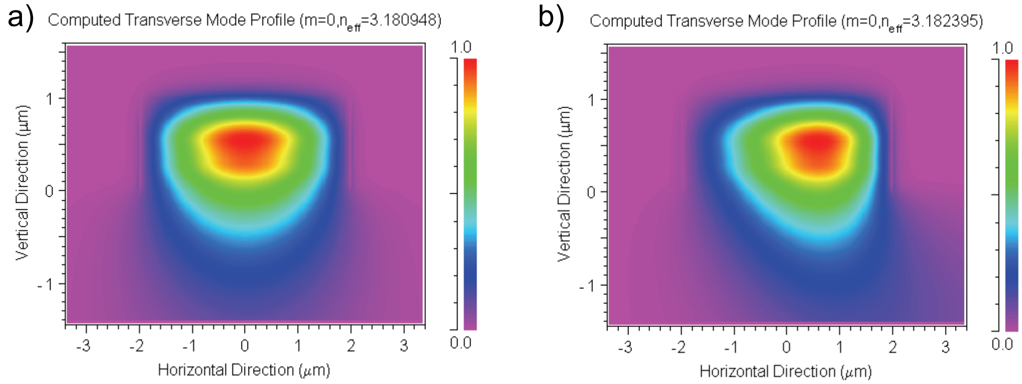

Figure 2-8. Fundamental mode of a) straight ridge waveguide; b) curved ridge waveguides (R=500 μm).

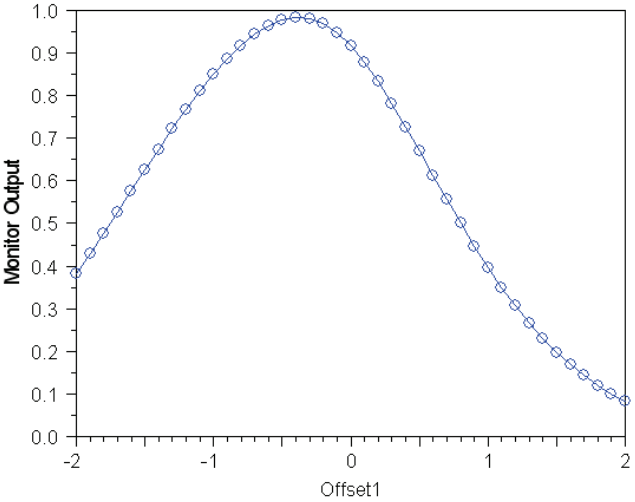

Figure 2-9. Offset optimization between a straight and a curved waveguide.

2.2.5 Ridge waveguide bends—conclusions

Calculation of bending losses in ridge waveguides is a challenging numerical task that requires a careful choice of boundary conditions. Complex-frequency leaky mode computations using perfectly matched boundary layers were employed to assess bending losses for this project. The results show that bent waveguides with radii of curvature on the order of several hundreds of microns suffer moderate losses per 90º turn.

2.3 Multimode Interference Devices

2.3.1 Principle of operation

Multi-mode interference (MMI) couplers employ specific integral relationships among the propagation constants of different waveguide modes to obtain the self-imaging of the input field at particular distances along the length of MMI couplers. Light is launched into and recovered from a multimode waveguide by means of several single-mode waveguides placed at the beginning and the end of the MMI. MMI with N input and M output waveguides is referred to as an NxM MMI. MMIs offer superior performance, better polarization tolerance and more relaxed fabrication requirements than directional and adiabatic couplers, especially with respect to the 3-dB splitting ratio [92-94].

Guided-mode propagation analysis (MPA) is used for theoretical analysis of MMI operation. The MPA method is valuable because it offers insight into the mechanism of multimode interference. Distance along an MMI where single or multiple images of the input signal are obtained is related to L_π, the beat length between the two lowest modes of the MMI [95]. Results of both the MPA derivations and the BPM simulations using RSoft are used in designing the MMIs for this project. All basic BPM calculations assume TE-polarized light. Performance of MMI devices for TM polarization is addressed when polarization sensitivity of the design is assessed.

2.3.2 Guided Mode Propagation Analysis

The principles of guided-mode propagation analysis are illustrated here for a two-dimensional representation of the multimode waveguide. Typical etch-patterning produces step-index structures with a significant ratio of width to height. Behavior of all modes of a multimode waveguide with respect to the vertical direction is very similar. Structures of this type can be analyzed by combining MPA with two-dimensional cross-section calculations [95].

2.3.2.1 Propagation constants

Suppose a step-index multimode waveguide has a width W_M and effective refractive index of the ridge is n_r. For light of free-space wavelength λ_0, the waveguide supports m lateral modes with mode numbers $\nu = 0,1,...,(m-1)$. Dispersion relationship

$$k_{x\nu}^2 + \beta_\nu^2 = k_0{}^2 n_r{}^2 \qquad \text{(Eq. 2-27)}$$

defines the relation between the lateral wavenumber $k_{x\nu}$, the propagation constant β_ν and the ridge index n_r. Here, wavenumbers are given by

$$k_0 = \frac{2\pi}{\lambda_0} \text{ and} \qquad \text{(Eq. 2-28)}$$

$$k_{y\nu} = \frac{(\nu+1)\pi}{W_{e\nu}} \qquad \text{(Eq. 2-29)}$$

where $W_{e\nu}$ is the effective width that takes into account lateral penetration depth of each mode field. For high-index-contrast waveguides, the penetration depth can be neglected so that $W_{e\nu} \approx W_{e0} \approx W_M$. Lets denote this width W_e. The propagation constants β_ν can be found by noting that $k_{x\nu}^2 << k_0^2 n_r^2$ and using binomial expansion:

$$\beta_\nu \approx k_0 n_r - \frac{(\nu+1)^2 \pi \lambda_0}{4 n_r W_e^2}. \qquad \text{(Eq. 2-30)}$$

According to Eq. 2-30 the propagation constants have an approximately quadratic dependence on the mode number ν. The beat length between the two lowest-order modes is given by

$$L_\pi \approx \frac{4 n_r W_e^2}{3\lambda_0} \qquad \text{(Eq. 2-31)}$$

and the spacing between the propagation constants in terms of the beat length is

$$(\beta_0 - \beta_\nu) \approx \frac{\nu(\nu+2)\pi}{3L_\pi}. \qquad \text{(Eq. 2-32)}$$

2.3.2.2 Guided-mode propagation analysis

For practical applications, an input field $\Psi(x,0)$ imposed at z=0 and totally contained within W_e typically does not excite unguided modes. The input field can therefore be decomposed into the superposition of guided modes:

$$\Psi(x,0) = \sum_{\nu=0}^{m-1} c_\nu \psi_\nu(x) \qquad \text{(Eq. 2-33)}$$

where the field excitation coefficients c_ν are estimated by overlap integrals based on the orthogonality relations:

$$c_\nu = \frac{\int \Psi(x,0)\psi_\nu(x)dx}{\sqrt{\int \psi_\nu^2(x)dx}}. \qquad \text{(Eq. 2-34)}$$

The field profile at a distance z is given by

$$\Psi(x,z) = \sum_{\nu=0}^{m-1} c_\nu \psi_\nu(x) \exp[j(\omega t - \beta_\nu z)]. \qquad \text{(Eq. 2-35)}$$

The above expression can be simplified by making the time dependence $\exp(j\omega t)$ implicit while also factoring out and dropping the phase of the fundamental mode:

$$\Psi(x,z)=\sum_{\nu=0}^{m-1}c_\nu\psi_\nu(x)\exp[j(\beta_0-\beta_\nu)z)]. \qquad \text{(Eq. 2-36)}$$

Substituting Eq. 2-32 into Eq. 2-36 we obtain an expression for the field at a distance z=L:

$$\Psi(x,L)=\sum_{\nu=0}^{m-1}c_\nu\psi_\nu(x)\exp[j\frac{\nu(\nu+2)\pi}{3L_\pi}L]. \qquad \text{(Eq. 2-37)}$$

It is useful to note the following properties:

$$\nu(\nu+2)=\begin{cases} even & for \quad \nu \quad even \\ odd & for \quad \nu \quad odd \end{cases} \qquad \text{(Eq. 2-38)}$$

and

$$\psi_\nu(-x)=\begin{cases} \psi_\nu(x) & for \quad \nu \quad even \\ -\psi_\nu(x) & for \quad \nu \quad odd \end{cases}. \qquad \text{(Eq. 2-39)}$$

Self-imaging of the input field is obtained by general interference when no conditions are placed on the modal excitation at the input. Restricted interference yields reproductions of the input field when certain modes alone are excited.

2.3.2.3 General interference

General interference places no restrictions on the coefficients c_ν. Only the properties of the mode phase factor determine the types of images formed. A self-image is formed at *z=L* if

$$\exp[j\frac{\nu(\nu+2)\pi}{3L_\pi}L]=1 \quad \text{or} \quad (-1)^\nu. \qquad \text{(Eq. 2-40)}$$

The first condition produces a direct image of the input field, while the second one yields an image mirrored with respect to the plane *x=0*. These conditions are fulfilled at

$$L = p(3L_\pi) \text{ with } p = 0, 1, 2, \ldots \qquad \text{(Eq. 2-41)}$$

for *p* even and *p* odd, respectively. In other words, general interference forms direct images at distances z that are even multiples of $(3L_\pi)$, and mirrored images at distances that are odd multiples of $(3L_\pi)$.

Two-fold imaging is required to realize 2x2 3-dB couplers. Let's consider the images obtained half way between the direct and mirrored image positions, that is, at distances

$$L = \frac{p}{2}(3L_\pi) \text{ where } p = 1, 3, 5, \ldots \qquad \text{(Eq. 2-42)}$$

Substituting Eq. 2-42 into Eq. 2-37 yields

$$\Psi(x, \frac{p}{2} 3L_\pi) = \sum_{\nu=0}^{m-1} c_\nu \psi_\nu(x) \exp\left[j\nu(\nu+2)p\left(\frac{\pi}{2}\right)\right]. \qquad \text{(Eq. 2-43)}$$

Using the properties Eq. 2-38 and Eq. 2-39, the above can be rewritten as

$$\Psi(x, \frac{p}{2} 3L_\pi) = \sum_{\nu \ even} c_\nu \psi_\nu(x) + \sum_{\nu \ odd} (-j)^p c_\nu \psi_\nu(x) = \frac{1+(-j)^p}{2} \Psi(x,0) + \frac{1-(-j)^p}{2} \Psi(-x,0). \qquad \text{(Eq. 2-44)}$$

According to the last equation, a pair of images of the input field, a direct and a mirror image, with amplitudes $\frac{1}{\sqrt{2}}$ are realized at distances $z = \frac{1}{2}(3L_\pi), \ \frac{3}{2}(3L_\pi), \ \ldots$

Compact MMI devices can be realized by restricted interference when only some of the guided modes are excited by the input. In order to exploit restricted interference mechanisms, input fields have to be symmetric and carefully located. Here in particular we discuss design of 1x2 MMIs based on symmetric interference and 2x2 3-dB couplers based on paired interference.

2.3.2.4 1x2 MMIs realized by symmetric interference

While N-way splitters can be realized by general interference at imaging length of

$$L = \frac{p}{N}(3L_{\pi}), \text{ with } p=0, 1, 2, \ldots \qquad \text{(Eq. 2-45)}$$

the same effect can be achieved with devices four times shorter if only the even symmetric modes are excited. Due to the fact that

$$\mathrm{mod}_4[\nu(\nu+2)] = 0 \text{ for } \nu \text{ even} \qquad \text{(Eq. 2-46)}$$

the four-fold reduction in the length periodicity can be obtained if the following condition is satisfied:

$$c_{\nu} = 0 \text{ for } \nu = 1,3,5,... \qquad \text{(Eq. 2-47)}$$

Single images of the field $\Psi(x,0)$ are achieved at

$$L = p(\frac{3L_{\pi}}{4}) \text{ for } p=0, 1, 2, \ldots \qquad \text{(Eq. 2-48)}$$

N-fold images are obtained at distances

$$L = \frac{p}{N}(\frac{3L_{\pi}}{4}) \text{ for } p=0, 1, 2, \ldots \qquad \text{(Eq. 2-49)}$$

Symmetric excitation condition can be easily achieved by launching a symmetric field into the multimude waveguide at x=0.

2.3.2.5 2x2 MMIs realized by paired interference.

Special interference mechanisms are based on peculiar multiplicities of $\nu(\nu+2)$.

Noting that

$$\mathrm{mod}_3[\nu(\nu+2)] = 0 \text{ for } \nu \neq 2,5,8,... \quad \text{(Eq. 2-50)}$$

leads to reduction in length periodicity by a factor of three for input fields that satisfy the condition

$$c_\nu = 0 \text{ for } \nu = 2,5,8,... \quad \text{(Eq. 2-51)}$$

For such inputs, direct and inverted single images are obtained at

$$L = p(L_\pi) \text{ for } p=0, 1, 2, \ldots \quad \text{(Eq. 2-52)}$$

Two-fold images are achieved at distances $\frac{p}{2}(L_\pi)$ where p is odd.

A practical way to satisfy requirements for selective excitation is to launch an even symmetric input at $x = \pm W_e / 6$. The modes with mode numbers $\nu = 2,5,8,...$ have a node with odd symmetry at these positions, causing the overlap integral with a symmetric field to be zero.

The length shift which produces a 0.5 dB loss is given approximately by the so-called Rayleigh range:

$$\delta L \approx \frac{\pi n_r w_0^2}{4\lambda_0} \quad \text{(Eq. 2-53)}$$

where w_0 is the full 1/*e* amplitude width of the input field $\Psi(x,0)$. It follows from the above relationship that tolerances can be relaxed by using wider access waveguides. For our devices $w_0 \approx 4$ µm and $\delta L \approx 26$ µm.

Reflections in an MMI device can originate at the end of the multimode section, especially between the output waveguides and when large index difference is present. Reflection mechanisms are particularly effective when they involve self-imaging properties for which MMIs are designed. One such mechanism is “internal resonance” when general and symmetric self-imaging occurs simultaneously, for examples, for a 3-dB coupler of length $L = \frac{3}{2}(L_\pi)$. This type of reflection can be prevented by designing couplers based on the paired interference mechanism.

Another type of reflection arises when a power splitter is used as a power combiner. For example, a 1x2 MMI can be used in reverse as an efficient power combiner if the two inputs are in phase. If on the contrary they are 180^o out of phase, power is minimum in the output guide but maximum at the reflecting end of the multimode section. This reflection mechanism can cause a problem during the off-state for a Mach-Zehnder modulator using a 2x1 MMI combiner. The issue can be avoided by using a 2x2 3-dB coupler instead of a combiner.

Imbalance of a coupler is defined as the maximum to minimum output power ratio for all outputs in dB.

2.3.3 Main examples: MMIs

1x2 and 2x2 MMIs were designed for the optical circuit in this project. The thickness and composition of semiconductor layers for the MMIs are determined by the design of passive ridge waveguides, as detailed in the previous sections. The dilute ridge waveguides with 4 μm x 1.05 μm cross-section described above serve as input and output ports to the 1x2 and 2x2 MMIs.

Two design considerations are important for setting MMI width. First of all, the distance between the two input and/or output waveguides has to be sufficiently large to ensure easy and reliable fabrication of the trench between the ridge waveguides by means of optical lithography and standard etching techniques. Since it is desirable to keep MMI dimensions as compact as possible, we chose to set the trench width to 2 μm. The second consideration for determining MMI width is that the multimode portion of an MMI has to support more than three optical modes in order to assure proper interference. Theoretical results derived by MPA are used to estimate appropriate length of the devices. RSoft BPM simulations are employed to confirm and refine the design.

2.3.3.1 1x2 MMI

The two outputs of 1x2 MMI are placed at $\pm W_{1x2}/4$ with respect to the MMI center, where W_{1x2} is the width of the multimode section of the device. Because the width of each output waveguide is 4 μm and the width of the trench is 2 μm, the distance between the centers of the output waveguides is 6 μm and the total width of the multimode section W_{1x2}=12 μm. To confirm that this width will produce a functional MMI device, it is necessary to determine how many optical modes a 12 μm-wide waveguide of given composition supports. RSoft BPM was used to calculate modes of the multimode waveguide. It was found that the waveguide supports five optical modes, which is sufficient for proper function of an MMI. The highest excited mode is shown in Figure 2-10.

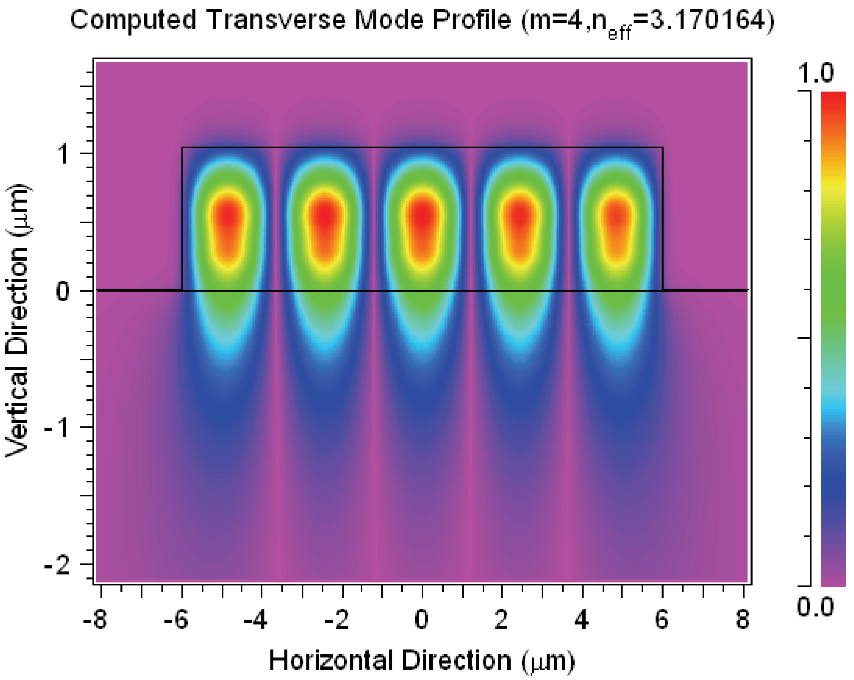

Figure 2-10. Highest-order mode of the 12 μm wide multimode section.

In order to obtain general guidance on required device length, we first calculate the beat length of the two lowest-order modes estimated by $L_{\pi 1x2} \approx \frac{4n_r W_{1x2}^2}{3\lambda_0}$, where λ_0=1.55 μm is the free-space wavelength, n_r=3.22 is the ridge index (calculated as a weighted square average of layer indices), W_{1x2}=12 μm is the width of the multimode waveguide. This yields $L_{\pi 1x2} \approx 399$ μm. For a 1x2 MMI, first 2-fold image distance (3-dB length) is related to $L_{\pi 1x2}$ the following way: $L_{3dB} \approx \frac{3L_{\pi 1x2}}{8}$. In our case $L_{3dB} \approx 150$ μm.

Propagation of light through the 1x2 MMI is then simulated with RSoft BeamPROP. The fundamental mode of a 4 μm-wide input waveguide is launched into that waveguide and subsequently propagates through the multimode section. At every step along the multimode section, the amount of energy in the fundamental mode of the two output waveguides is monitored as if the multimode waveguide were terminated at that length. The optimal length of the 1x2 MMI is determined to be 157.4 µm. At this length 0.49 of the input power resides in each of the output waveguides. The small discrepancy (~0.1 dB) with an ideal 0.5 figure can be explained by the finite number of modes participating in multimode interference. Figure 2-11 is included for comparison between an ideal case and the actual calculated output of the 1x2 MMI under consideration. In the ideal case, each output waveguide receives 0.5 of the input light in the form of the fundamental mode of a passive waveguide. In the actual case, the optical field incident on each output waveguide is somewhat distorted, resulting in small scattering losses.

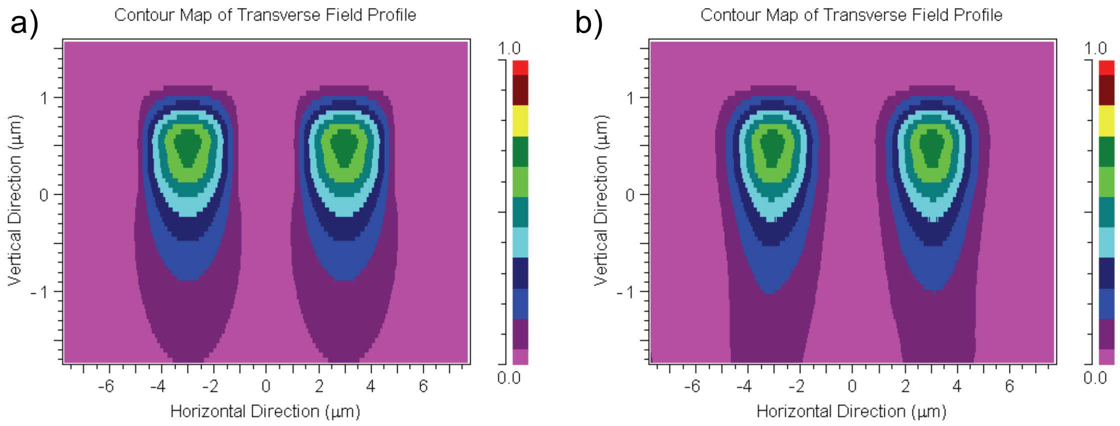

Figure 2-11. Output of 1x2 MMI splitter: a) ideal, b) computed for the described design.

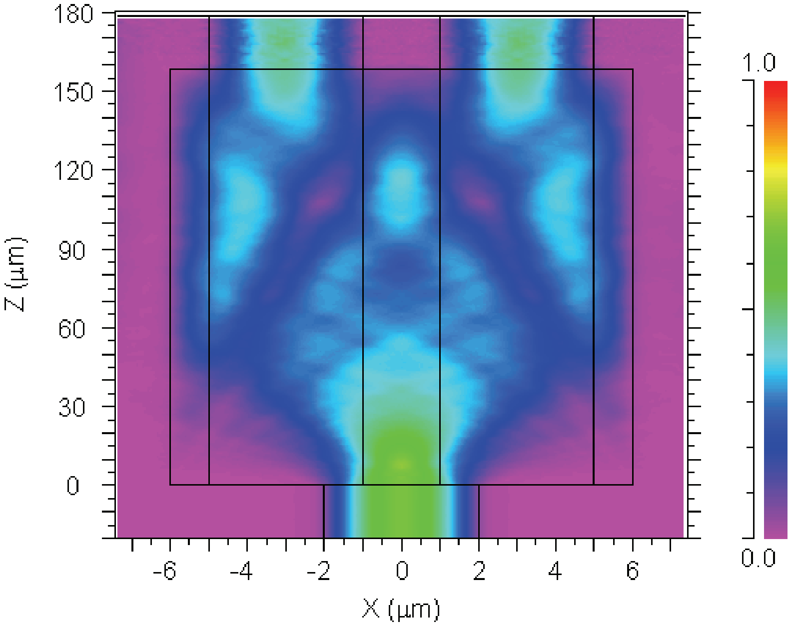

Figure 2-12. Operation of 1x2 MMI splitter.

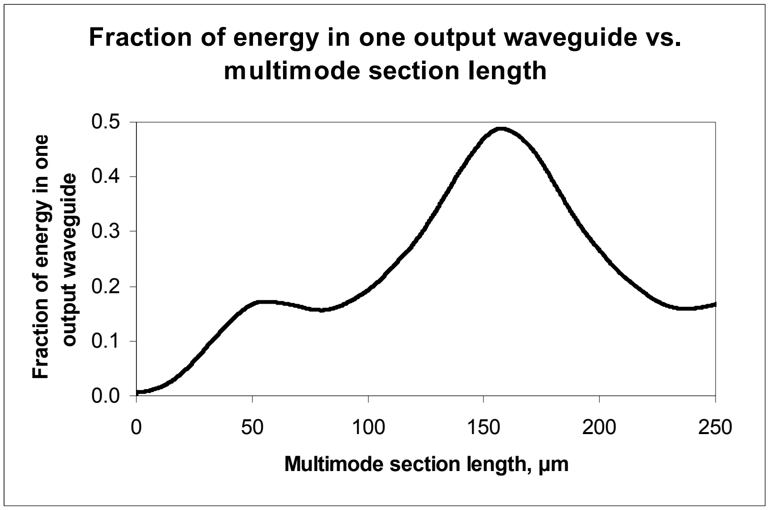

Figure 2-13 Optical power in one of 1x2 MMI outputs as a function of multimode section length

Figure 2-12 illustrates operation of 1x2 MMI. Figure 2-13 tracks the power in the output waveguides as a function of multimode section length. In this figure, the multimode section is made intentionally longer than the optimal length in order to demonstrate how the optimal length is determined and to assess MMI's robustness with respect to its length. The length of the multimode section in the range of 144 μm- 173 μm produces energy transfer into the output waveguide within 0.9 of the maximum value. Imbalance in the 1x2 splitter is very small: on the order of 10^{-2}-10^{-3} dB for this range.

Polarization sensitivity was assessed by launching the fundamental TM mode into the 1x2 MMI optimized for TE polarization. Care was taken to ensure that TM polarization option was activated on the BPM tool. The power in the fundamental TM mode of each output waveguide was calculated. It was found that TM-polarized light is coupled into the output waveguides less efficiently than TE mode by approximately 0.2 dB with an imbalance on the order of 10^{-2} dB.

2.3.3.2 2x2 MMI

The two input and two outputs of 2x2 MMI are placed at $\pm W_{2x2}/6$ with respect to the MMI center, where W_{2x2} is the width of the multimode section of the device. We will refer to the input and output at $-W_{2x2}/6$ as input 1 and output 1, and to the input and output at $W_{2x2}/6$ as input 2 and output 2, respectively. As in the 1x2 MMI design described above, the distance between the centers of the two output waveguides (and here also between the two input waveguides) is 6 μm, which represents one third of the total 2x2 MMI width. The width of the multimode section W_{2x2}=18 μm. It is certain that 18 μm-wide waveguide supports a sufficient number of optical modes since it was shown above that a 12 μm-wide waveguide with the same composition satisfies the same requirement.

The beat length of the two lowest-order modes is approximated by $L_{\pi 2x2} \approx \frac{4n_r W_{2x2}^2}{3\lambda_0}$, where W_{2x2}=18 μm is the width of the multimode waveguide. In this case, the beat length is $L_{\pi 2x2} \approx 897$ μm. For a 2x2 MMI, 3-dB length can be found as $L_{3dB} \approx \frac{L_{\pi 1x2}}{2}$. Here, $L_{3dB} \approx 449$ μm.

As the next step, operation of the 2x2 MMI is simulated with RSoft BPM tool. The fundamental mode of a 4 μm-wide input waveguide is launched into input waveguide 1 and propagates through the multimode section. The amount of energy in the fundamental mode of output 1 and output 2 is monitored along the length of the multimode section. The optimal length of the 2x2 MMI is found to be 480 μm. At this length 0.488 of the input power is transferred to output 1 and 0.472 to output 2.

Figure 2-14 illustrates propagation of light in the multimode section of 2x2 MMI. Figure 2-15 shows the power in the output waveguides as a function of multimode section length. As with the 1x2 MMI, the multimode section is extended well beyond its optimal length. This computation allows us to assess robustness of the 2x2 MMI with respect to length of the multimode section. Imbalance of the coupler is minimized for a length of 467 μm at ~$3\text{x}10^{-4}$ dB. The length of the multimode section in the range of 462 μm—494 μm produces energy transfer into the output waveguide within 0.9 of the maximum value. Imbalance for devices in this range is below 0.2 dB.

Polarization sensitivity was assessed by launching the fundamental TM mode into input 1. The power in the fundamental TM mode of each output waveguide was calculated. Compared to TE-polarized light, TM-polarized light is coupled into the output waveguides with an extra loss of about 0.1—0.2 dB. Corresponding imbalance between the two outputs is approximately 0.05 dB.

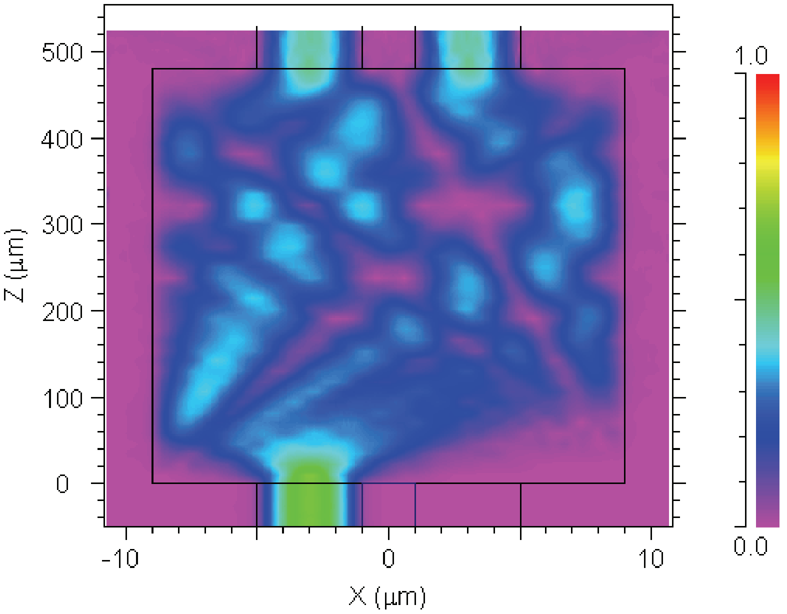

Figure 2-14. Operation of 2x2 MMI as a 3 dB splitter.

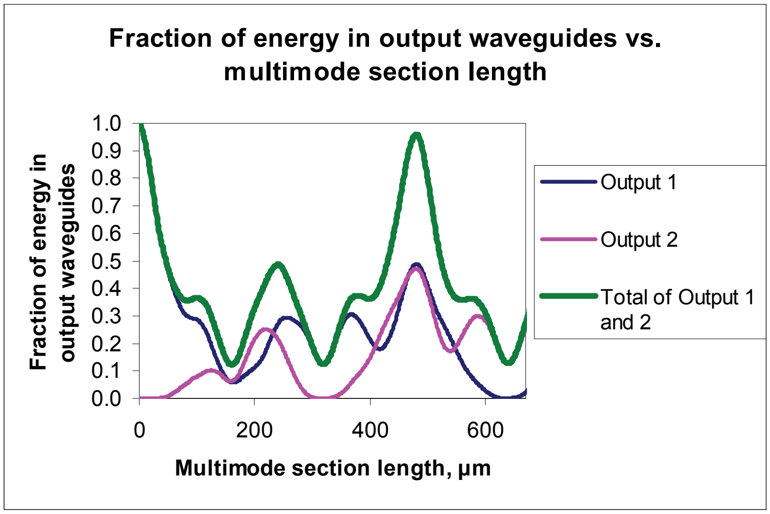

Figure 2-15. Optical power in 2x2 MMI outputs as a function of multimode section length.

2.3.3.3 Combiners

As discussed in Section 2.3.2.5, using a 1x2 MMI in reverse as a power combiner produces desired results only if the two inputs are in phase (Figure 2-16 a). If the two inputs are out of phase, a significant fraction of optical power will be incident on the end of the multimode section and will be reflected. The most extreme case occurs when the two inputs are 180° out of phase as the power incident is on the reflecting end of the multimode section (Figure 2-16 b). The problem is avoided by using a 2x2 3-dB coupler. Operation of 2x2 MMI with different relative phases between the two inputs is illustrated in Figure 2-17.

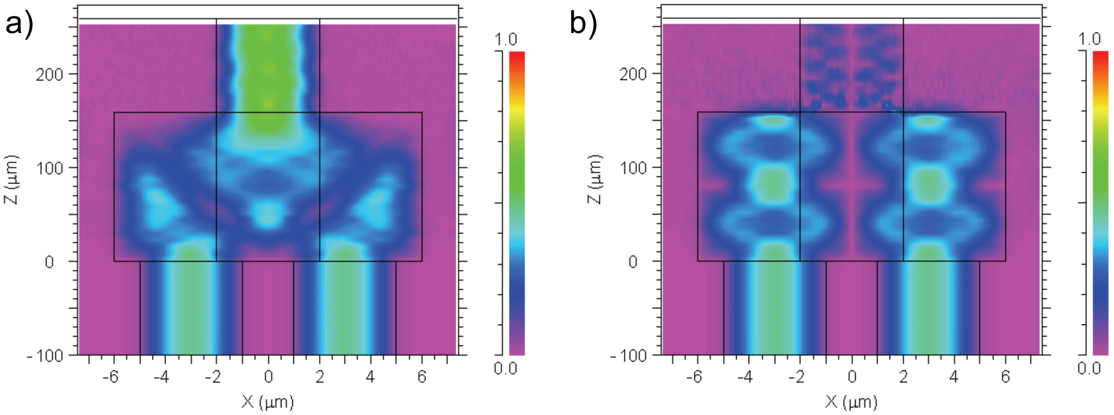

Figure 2-16. 2x1 MMI combiner a) inputs in phase; b) inputs 180° out of phase.

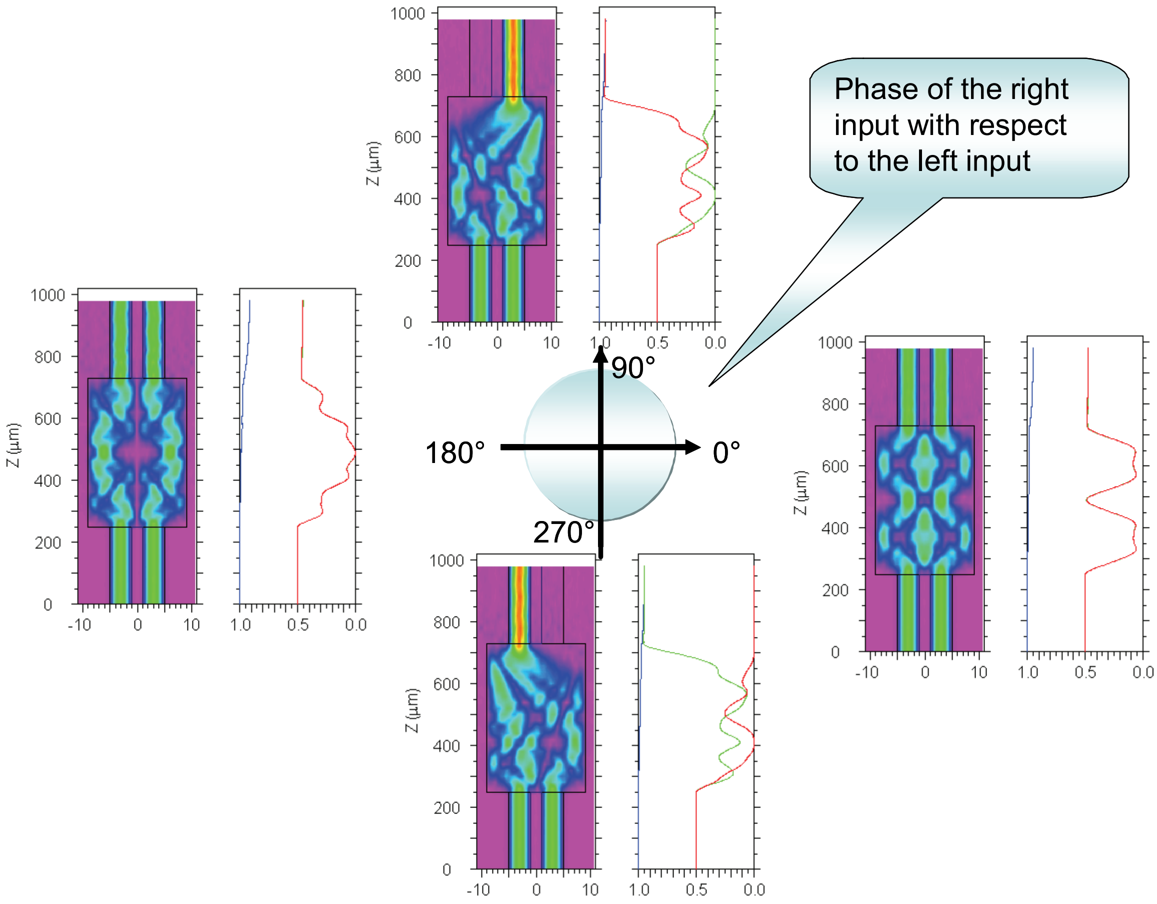
Phase of the right input with respect to the left input

Figure 2-17. Operation of 2x2 MMI with different relative phases between the two inputs.

2.3.3.4 Tolerance to underetching of trenches

Important issue of MMI robustness for deep-etched, high-index contrast design such as presented in this work is tolerance to underetching of trenches between the two outputs of a 1x2 MMI and two input and two outputs of a 2x2 MMI. Guided by the structure of the dilute waveguide, we chose two cases for the sake of such assessment. The etch depth for a perfectly fabricated trench between the access waveguides is 1.05 µm. In the case of moderate underetching, the bottom quaternary layer of the dilute waveguide acts as an etch-stop layer; the depth of the trench is 0.75 µm. (Figure 2-18 a.)

In the case of severe underetching, the middle quaternary layer acts as an etch-stop; the etch depth is only 0.3 µm. (Figure 2-18 b.)

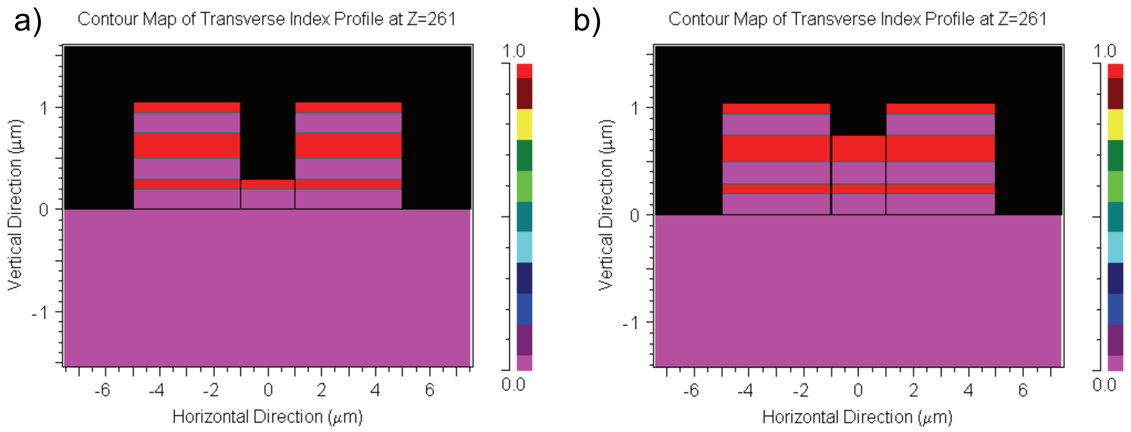

Figure 2-18. Index profiles of output waveguides with underetched trenches: a) moderately underetched; b) severely underetched.

Moderately underetched 1x2 MMI splitter is approximately as efficient as a perfectly etched splitter, while a severely underetched device is almost 0.3 dB less efficient than the properly etched one. Imbalance in underetched 1x2 splitters remains low, on par with the properly etched devices.

In a 2x2 MMI operated as a 3 dB coupler, moderate underetching produces no extra loss, while severe underetching produces an extra loss of less than 0.2 dB. Imbalance is both versions of underetched device is ~0.3 dB.

When the trench between the output waveguides is underetched, light in the output waveguides displays a peculiar oscillatory behavior (Figure 2-19). To explain this phenomenon, it is necessary to examine the supermodes of the structure consisting of the two parallel waveguides and the trench between them. When the trench is etched properly, the structure possesses two easily predictable TE modes: a symmetric and an anti-symmetric one. For both modes, most of the optical energy is concentrated in the two ridge waveguides. (Same is true for TM modes.) Figure 2-20 illustrates TE and TM modes of the properly etched structure. Underetching of the trench results in additional high-index material between the output waveguides. In turn, the higher overall effective index of the structure leads to the existence of higher-order modes. Figure 2-21 shows the modes of the severely underetched version of the structure. The most likely explanation for the oscillation in the output waveguides is an interaction between the fundamental TE mode and the higher-order symmetric TE mode with effective indices of 3.1818 and 3.1697, respectively. This proposition is confirmed by calculation of coupling length between the two modes: $\Delta n_{eff}=0.0121$ and estimated coupling length $L_c=64$ µm, consistent with the oscillation period.

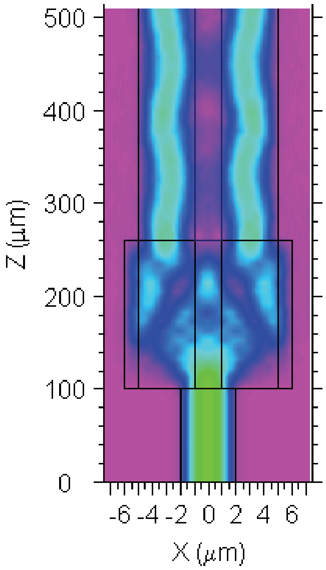

Figure 2-19. Optical power oscillations in the output waveguides with a severely underetched trench.

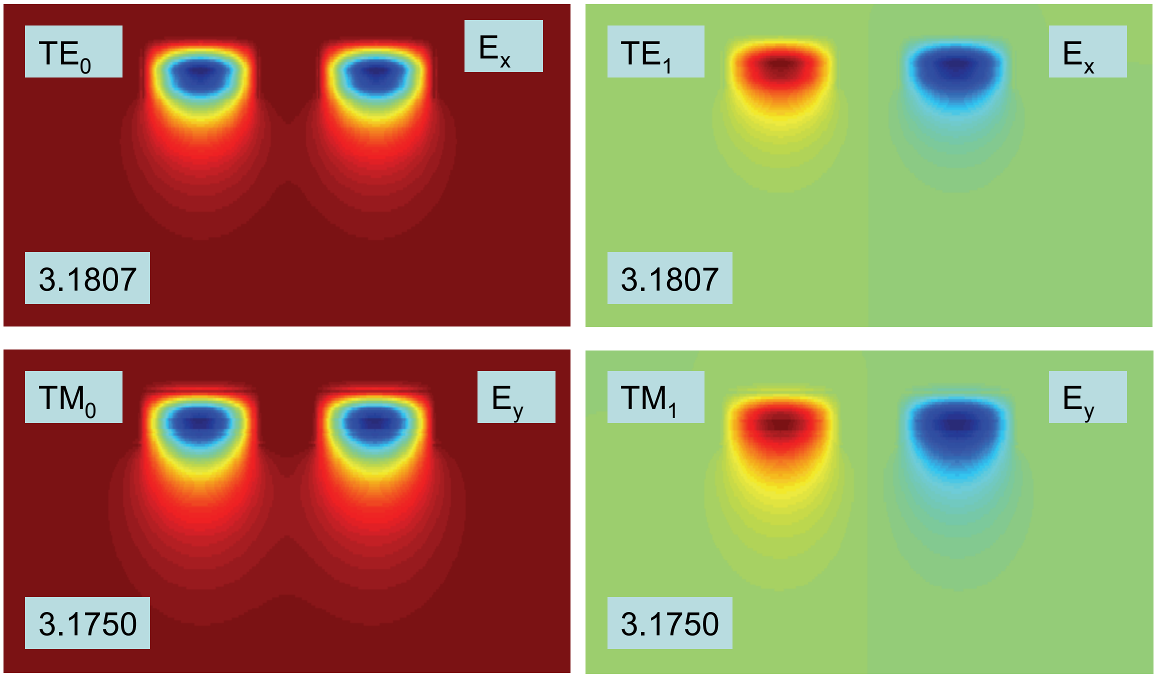

Figure 2-20. Modes of the properly etched structure.

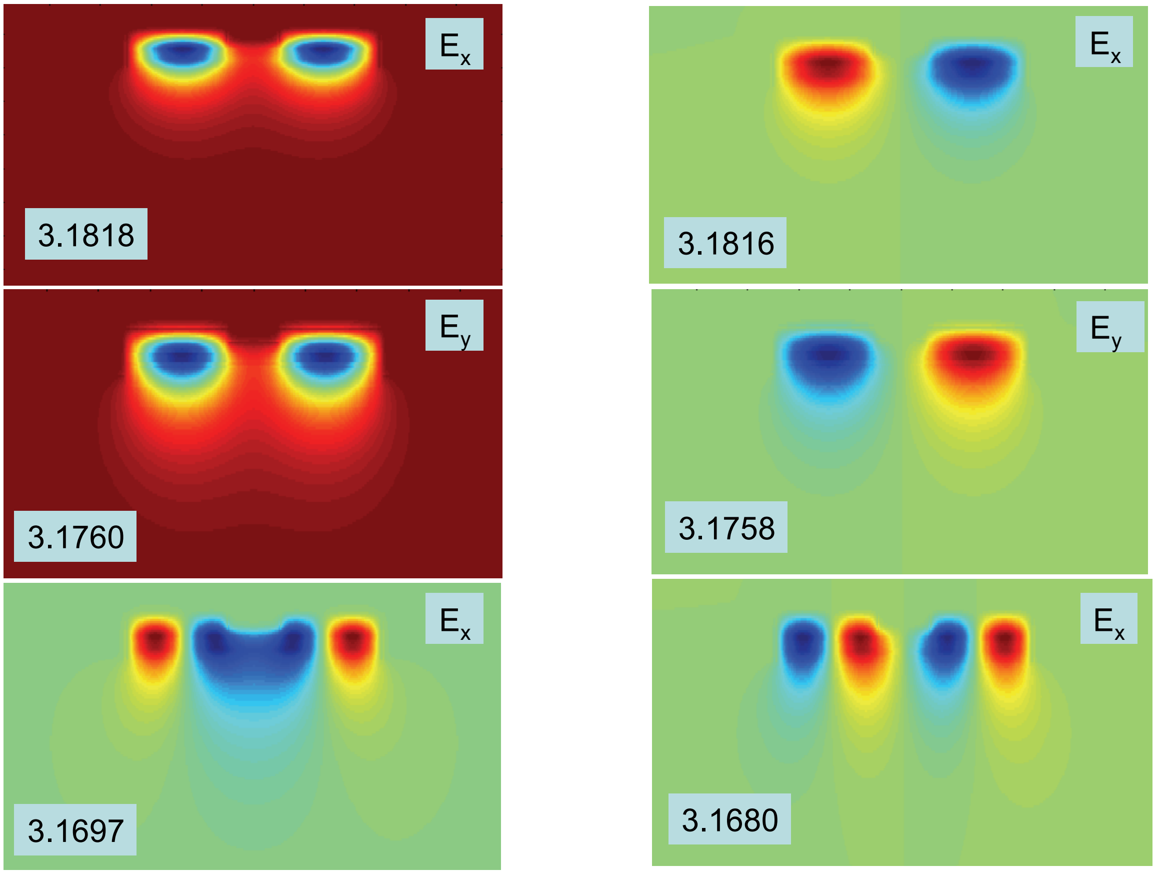

Figure 2-21. Modes of severely underetched structure.

2.3.4 Multimode interference devices—Conclusions

MMI splitters are effective and robust devices. Like other high-contrast ridge waveguide structures, MMIs suffer from some polarization sensitivity. However, MMIs designed for TE modes perform well for TM-polarized light. Both 1x2 and 2x2 devices are not very sensitive to variations in length of the multimode section on the order of microns or even tens of microns. Underetching of trenches does not drastically undermine device performance, but gives rise to unwanted oscillatory behavior in the output waveguides due to existence of higher-order modes and their interaction with the fundamental mode of the structure.

52. S. N. Dudorov, D. V. Lioubtchenko, and A. V. Raisanen, *Modification of Marcatili's method for the calculation of anisotropic rectangular dielectric waveguides.* Microwave Theory and Techniques, IEEE Transactions on, 2002. **50**(6): p. 1640-1642.

53. E. A. J. Marcatili, *Dielectric rectangular waveguide and directional coupler for integrated optics.* Bell Syst. Tech. J.,, 1969. **48**: p. 2071-2102.

54. C. Kin Seng, *Analysis of the effective-index method for the vector modes of rectangular-core dielectric waveguides.* Microwave Theory and Techniques, IEEE Transactions on, 1996. **44**(5): p. 692-700.

55. J. J. G. M. Van Der Tol and N. H. G. Baken, *Correction to effective index method for rectangular dielectric waveguides.* Electronics Letters, 1988. **24**(4): p. 207-208.

56. A.A. Abour El-Fadl. *An optimal method to study the propagation characteristics of rectangular optical waveguides*. in *Radio Science Conference*. 1998.

57. J. Buus, *The effective index method and its application to semiconductor lasers.* Quantum Electronics, IEEE Journal of, 1982. **18**(7): p. 1083-1089.

58. G. M. Berry, et al., *Exact and variational Fourier transform methods for analysis of multilayered planar waveguides.* IEE Proc. – Optoelectronics, 1995. **142**: p. 66-75.

59. P. McIlroy, M. S. Stern, and P. C. Kendall, *Spectral index method for polarised modes in semiconductor rib waveguides.* Journal of Lightwave Technology, 1990. **8**: p. 113-117.

60. P. C. Kendall, P. McIlroy, and M. S. Stern, *Spectral index method for rib waveguide analysis.* Electronics Letters, 1989. **25**: p. 107-108.

61. G. M. Berry, et al., *Analysis of mulilayer semiconductor rib waveguides with high refractive index substrates.* Electronics Letters, 1993. **29**: p. 1941-1942.

62. P. Sewell, et al., *Full vector analysis of two-dimensional angled and coated optical waveguide facets.* Quantum Electronics, IEEE Journal of, 1997. **33**(12): p. 2311-2318.

63. M. Reed, et al., *Efficient propagation algorithm for 3D optical waveguides.* Optoelectronics, IEE Proceedings-, 1998. **145**(1): p. 53-58.

64. M. Reed, et al., *Antireflection-coated angled facet design.* Optoelectronics, IEE Proceedings-, 1996. **143**(4): p. 214-220.

65. K. Bierwirth, N. Schulz, and F. Arndt, *Finite difference analysis of rectangular dielectric waveguide structures.* IEEE Trans. Microwave Theory Tech., 1986. **34**: p. 1104-1114.

66. E. Schweig and W. B. Bridges, *Computer analysis of dielectric waveguides: a finite difference method.* IEEE Trans. Microwave Theory Tech., 1984. **32**: p. 531-541.

67. S. S. Patrick and K. J. Webb, *A variational vector finite difference analysis for dielectric waveguides.* IEEE Trans. Microwave Theory Tech., 1992. **40**: p. 692-698.

68. M. Koshiba and K. Inoue, *Simple and efficient finite-element analysis of microwave and optical waveguides.* IEEE Trans. Microwave Theory Tech., 1992. **40**: p. 371-377.

69. B. M. A. Rahman and J. B. Davies, *Finite element analysis of optical and microwave waveguide problems.* IEEE Trans. Microwave Theory Tech., 1984. **32**: p. 20-28.

70. Y. Chung and N. Dagli, *An assessment of finite difference beam propagation method.* IEEE J. of Quantum Electronics, 1990. **26**: p. 1335-1339.

71. W. P. Huang, et al., *A finite difference vector beam propagation method: analysis and assessment.* Journal of Lightwave Technology, 1992. **10**: p. 295-305.

72. W. P. Huang, C. L. Xu, and S. K. Chaundhuri, *A finite difference vector beam propagation method for three dimensional waveguide structures.* IEEE Photonic Technology Letters, 1992: p. 148-151.

73. A. Vukovic, *Fourier Transformation Analysis of Optoelectronic Components and Circuits*. 2000, University of Nottingham.

74. K. S. Chiang, *Review of numerical and approximate methods fort he analysis of general optical dielectric waveguides.* Optical and Quantum Electronics Letters, 1994. **26**: p. 113-134.

75. RSoft, *BeamPROP* 1993-2002, Columbia University: Ossing, NY.

76. Yu-Li, H., Y. Ming-Chuan, and C. Hung-Chun, *Three-dimensional noniterative full-vectorial beam propagation method based on the alternating direction implicit method.* Lightwave Technology, Journal of, 1999. **17**(11): p. 2389-2397.

77. R. Scarmozzino and R.M. Osgood, *Comparison of finite-difference and Fourier-transform solutions of the parabolic wave equation with emphasis on integrated-optics applicatiuons.* J. Opt. Soc. Amer. A, 1991. **8**: p. 724.

78. J.-M. Verdiell, M. Ziari, and D.F. Welch, *Low-loss coupling of 980 nm GaAs laser to cleaved singlemode fibre.* Electronics Letters, 1996. **32**(19): p. 1817-1818.

79. M.H. Shih, et al., *Alignment-relaxed 1.55 um multiquantum well lasers fabricated using standard buried heterostructure laser processes.* Electronics Letters, 1995. **31**(13): p. 1058-1060.

80. V. Vusirikala, et al., *GaAs-AlGaAs QW diluted waveguide laser with low-loss, alignment-tolerant coupling to a single-mode fiber.* Photonics Technology Letters, IEEE, 1996. **8**(9): p. 1130-1132.

81. M. Rivera, *A finite difference BPM analysis of bent dielectric waveguides.* Journal of Lightwave Technology, 1995. **13**: p. 233-238.

82. N.-N. Feng, et al., *Computation of full-vector modes for bending waveguide using cylindrical perfectly matched layers.* Journal of Lightwave Technology, 2002. **20**(11): p. 1976-1980.

83. W.W. Lui, et al., *Full-vectorial wave propagation in semiconductor optical bending waveguides and equivalent straight waveguide approximations.* Journal of Lightwave Technology, 1998. **16**(5): p. 910-914.

84. J.-P. Berenger, *A perfectly matched layer for the absorption of electromagnetic waves.* Journal of Computational Physics, 1994. **114**: p. 185–200.

85. M. Popović, *Complex-frequency leaky mode computations using PML boundary layers for dielectric resonant structures*. 2003, Optical Society of America.

86. W.P. Huang, et al., *The perfectly matched layer boundary condition for modal analysis of optical waveguides: leaky mode calculations.* Photonics Technology Letters, IEEE, 1996. **8**(5): p. 652 – 654.

87. C.-P. Yu and H.-C. Chang, *Yee-mesh-based finite difference eigenmode solver with PML absorbing boundary conditions for optical waveguides and photonic crystal fibers.* Optics Express, 2004. **12**(25): p. 6165-6177.

88. C. Manolatou and H.A. Haus, *Passive components for dense optical integration*. 2002, Boston: Kluwer Academic Publishers.

89. F.L. Teixeira and W.C. Chew, *PML-FDTD in cylindrical and spherical grids.* Microwave and Guided Wave Letters, IEEE [see also IEEE Microwave and Wireless Components Letters], 1997. **7**(9): p. 285-287.

90. K. Radhakrishnan and W.C. Chew, *An efficient Krylov-subspace-based algorithm to solve the dielectric-waveguide problem.* IEEE Trans. on Microwave Theory and Tech., 2001. **49**: p. 1345-1348.

91. W.C. Chew, *Electromagnetic theory on a lattice.* J. Applied Phys., 1994. **75**: p. 4843–4850.

92. D.G. Rabus, *Optical Multi-Mode Interference Devices Based on Self-Imaging : Principles and Applications*. 2002, Heinrich-Hertz-Institut für Nachrichtentechnik Berlin.

93. J. Leuthold, et al., *Multimode interference couplers for the conversion and combining of zero- and first-order modes* Journal of Lightwave Technology, 1998. **16**(7): p. 1228 -1239.

94. P.A. Besse, et al., *New 2x2 and 1x3 multimode interference couplers with free selection of power splitting ratios.* Lightwave Technology, Journal of, 1996. **14**(10): p. 2286-2293.

95. L. B. Soldano and E. C. M. Pennings, *Optical Multi-Mode Interference Devices Based on Self-Imaging : Principles and Applications.* Journal of Lightwave Technology, 1995. **13**(4): p. 615-627.

3 Interfaces Between Passive and Active Devices

Interface between passive and active components is a critical aspect of integrated optical circuits that requires careful modeling. Quality of interfaces has a major impact on the performance of the entire optical circuit. Numeric simulations allow us to choose optimal device parameters from a range of choices that include various materials and geometries—a task prohibitively labor- and time-consuming if attempted experimentally. We also use modeling to access fabrication tolerances and effects of semiconductor processing imperfections on passive-active device interfaces.

The type of interface created between passive and active devices depends on the integration method. Monolithic integration strategies are butt coupling, quantum well disordering, and asymmetric twin waveguides (ATG). The first two methods produce abrupt interfaces. ATG method uses adiabatic tapers to guide light between passive waveguides and active components.

Preferred type of interface depends in part on the devices that need to be integrated. In the case of the optical logic unit sell, SOAs are integrated with passive waveguides. To operate an SOA as a broadband single-pass device, it must have low facet reflectivity to avoid the creation of resonator modes. Therefore, it is desirable to choose an analysis method that effectively takes into account reflections at interfaces.

BPM is extremely useful and efficient in exploring the power transfer between the modes of the ATG structure and those of passive waveguides. As with modeling passive waveguides, semi-vectorial approximation is sufficient because coupling of the transverse field components can be neglected. However, BPM is inadequate for assessing reflections because it is inherently limited by the paraxial approximation. Because of its fundamental limitations, BPM can not be used to accurately model devices for which reflection is significant.

Finite Difference Time Domain (FDTD) method represents a suitable choice for calculating reflections at interfaces. FDTD is a versatile and intuitive time domain technique. It is based on translating Maxwell's equations in differential form into the difference equations. A computational domain is established and divided into a grid. Discretized Maxwell's equations describe dependence of the electric field on the previous value of the electric field and the difference in the previous values of the magnetic field on either side of the electric field point in space. Similarly, the new value of the magnetic field depends on the previous value of the magnetic field and the difference between the earlier-time values of the electric field on either side of the magnetic field point in space. Then E and H fields are calculated everywhere in the computational domain in a leap-frog manner: the electric field is calculated at a given instant in time, then the magnetic field is found at the next instant in time, and so on. A significant difficulty in using FDTD is that the technique required large computational resources. This requirement arises from the fact that the entire computational domain is considered for every point in time, and the grid has to be sufficiently small compared to the smallest feature of the simulated device. 3D FDTD is especially computationally intensive. In this work, short sections of the photonic integrated circuit around potentially reflective interfaces are modeled with the help of FDTD.

This chapter starts with a review of monolithic integration techniques. BPM CAD tool is then used to optimize the geometry of an ATG structure. FDTD is used to assess reflection from abrupt interfaces.

3.1 Review of monolithic integration techniques

3.1.1 Butt coupling

Butt coupling technology is relatively well developed and achieves impressively low coupling losses despite numerous technological challenges. The chief advantage of butt coupling is an entirely separate optimization of layer thicknesses, composition and electrical properties for each device [96]. The main drawback is the need for sophisticated processing and epitaxial regrowth.

Creation of a butt-coupled device starts with epitaxial growth for one of the device structures, for the purposes of the example, the passive structure. The epitaxial wafer is then coated with a layer of dielectric material and patterned to delineate passive and active sections. In the active device areas, corresponding to the openings in the hard mask, InP and InGaAsP layers are etched with Reactive Ion Etching (RIE) or by a mixed process including an initial chemical etch step. The damaged layers are then removed with a wet etch. The second epitaxial structure is grown in the channel created by the etching process. Often more than one regrowth step needs to be performed, sometimes employing both Gas Source Molecular Beam Epitaxy (GSMBE) or Metal Organic MBE (MOMBE) and Metal Organic Chemical Vapor Deposition (MOCVD) to complete the growth for an integrated photonic circuit [96, 97]. GSMBE and MOMBE both have certain advantages as epitaxial regrowth techniques. Discussion of their comparative merits is beyond the scope of this work.

Although butt coupling has been widely used for monolithic integration, it has serious disadvantages as it requires epitaxial regrowth of the active material layers after the passive waveguides have been patterned [98-100]. Achieving high coupling efficiency with regrowth techniques is a challenge because of imperfections of the resulting interfaces. The quality of the interface is also likely to affect performance of some devices such as, for example, SOAs. In short, butt-coupled devices fabricated using material regrowth typically suffer from yield and high costs [101].

3.1.2 Quantum well disordering

Recently, there has been a lot of research into monolithic integration of optical components by Quantum Well Disordering (QWD). QWD is a family of techniques in which a heterostructure includes quantum well active material and the bandgap of the material is locally altered. The surface of the structure is patterned in order to define locations of active and passive devices. The processing that follows achieves two effects: the bandgap wavelength is lowered at the passive device locations while the quantum wells remain intact at the active device sites [102, 103].

Quantum well disordering is based on interdiffusion of lattice atoms in a quantum well or multiple quantum wells with the atoms in the barrier layers [104]. This process relies on the presence of point defects—vacancies or interstitials--in the lattice. Diffusion of the point defects through the lattice allows individual atoms to hop from one lattice site to another. The cumulative result of many atoms' movements is intermixing of QW material with that of the adjacent barrier [105]. Intermixing permanently alters the well width and potential barrier height. In the limit of complete intermixing, the disordering process forms a semiconductor alloy with the average composition of the wells and barriers. Usually, less incomplete intermixing yields structures of intermediate bandgap in which 2-D properties of the QWs are partially retained [106]. The bandgap of the disordered material is larger than that of the original QW structure. Larger bandgap regions are used as optical interconnects between the narrow bandgap devices used as gain or photodetection elements [105].

QWD techniques described in the literature include impurity induced disordering (implanted or diffused from the surface) [107-109], photoabsorption-induced disordering (PAID) [106, 110], dielectric cap quantum well disordering (DCQWD) [111, 112], and impurity-free vacancy diffusion [103, 113], the latter two methods being essentially the same.

Originally, impurity induced disordering was the most common method of QWD. It involves implantation or diffusion of an electrically active dopant species, either p-type (ex. Zn, Mn and Mg) or n-type (ex. Si, Se, S, Ge and Sn), typically followed by rapid thermal annealing (RTA). Ion bombardment generates lattice defects which diffuse into the structure upon RTA, promoting the disordering of the host atoms [102].

Unfortunately, ion bombardment introduces free carriers via the ionization of the dopants, leading to unintended losses through free-carrier absorption. Implantation of neutral impurities such as B and F has been demonstrated to improve electrical isolation and reduce absorption loss in the disordered regions [114]. Ion-implantation disordering is attractive in part because the process has been extensively developed for use in the silicon IC industry and offers the capability for well-defined patterning and damage control. A new technique called plasma immersion ion implantation (PIII) or plasma source ion implantation offers some advantages in comparison to conventional beam-line ion implantation. In particular, PIII is suitable for processing of large and non-planar samples [102]. Ion implantation can also be effectively impurity free if a matrix element is used as the implanted species [105]. For example, low-energy arsenic ion-implantation induced disordering was demonstrated to produce a bandgap blue shift up to 60 meV [107, 108].

Laser-induced disordering, also called photoabsorption-induced disordering, has two variations which employ two distinct mechanisms. When continuous wave radiation is used, preferential absorption of laser photons in QW layers generates heat [110]. Laser heating causes an increase in the concentration and diffusion coefficient of vacancies which results in disordering. This method suffers from poor spatial resolution due to lateral heat conduction. The use of a pulsed laser is preferable, as such a process creates point defects directly in the semiconductor [105]. Laser intermixing is especially useful in the InGaAs/InGaAsP QW system. This material has poor thermal stability and can be seriously compromised by thermal annealing [106].

Dielectric cap or vacancy-enhanced disordering techniques use dielectric caps on the surface of the semiconductor to create vacancies. Dielectric materials, capping layer thickness [115, 116], and annealing times are carefully designed to control the amount of intermixing [105]. A number of dielectric capping materials has been studied, among them SiO_2, SiN_x, SrF_2, and WN_x. Yi at al. [111] experimented with several dielectric-semiconductor capping layer combinations for InGaAs/InGaAsP single QW system in an effort to find the optimum combinations for device applications. The SiN_x-InP combination showed the largest energy shift while the SiO_2-InGaAsP combination showed the smallest [111]. In general, it is known that SiO_2 inhibits intermixing in the phosphorous-containing quaternary systems [114], while SrF_2 does the same for AlGaAs/GaAs system [103, 113]. An appropriate choice of capping layers can be made in order to obtain desired bandgap tuning for the integration of photonic devices, for example, SiO_2/ SiN_x can be used on InP substrates and SrF_2/ SiO_2 on GaAs substrates.

QWD approach has some significant advantages. Most importantly, QWD insures that different waveguide sections are perfectly aligned with each other. Small refractive index step at an active/passive interface can also be desirable, resulting in very low reflection coefficients—typically on the order of 10^{-5} [105]. The main drawback of QWD techniques is that it typically produces passive waveguides with unacceptably high losses [113, 114], while the performance of the active material is sometimes compromised by the fabrication processes used for quantum well disordering. A common problem is an increased threshold current in semiconductor lasers [103]. Due to limitations on the materials that can be integrated by QWD, this method is currently applicable mostly to laser-waveguide and laser-modulator integration [101].

3.1.3 Asymmetric Twin Waveguides

Early attempts to use twin waveguides (TG) for photonic integration were made in mid-1970s in AlGaAs material system. Suematsu et al. published a theoretical and experimental investigation of the first TG laser consisting of vertically-integrated active and passive waveguides [116]. The goal was to provide a semiconductor laser with an integrated optical output circuit. Conventional semiconductor bar lasers use cleaved facets as reflecting mirrors, and a monolithic connection to a passive waveguide was needed. A double heterostructure was used to build an integrated twin-guide laser with two vertically-stacked waveguides: an active waveguide for laser oscillation and a passive waveguide for the light output [116]. The laser and the phase-matched passive waveguide were grown during the same epitaxy and were sufficiently close that the light between them was coupled by an evanescent field in a manner similar to that of a directional coupler. Integration of passive and active components was achieved by selective removal of the active upper waveguide [101]. Yamada and Suematsu analyzed the threshold of integrated TG lasers with coupled-mode theory [115]. However, early structures were very sensitive to thickness and index of epitaxial layers. Since perfect control of epitaxial layer composition is extremely challenging, in early twin-guide lasers the coupling into the passive waveguide and the threshold current were essentially uncontrollable [117, 118].

The cause of the difficulty resides in the interaction between the even and odd modes in the basic TG structure. As a result of this interaction, the fraction of the total optical power incident on the etched facet of the laser represents a periodic function of cavity length [117, 119, 120]. Thus, the amount of power reflected from the facet becomes very difficult to control. The difficulty is compounded by the fact that the modal gain and the coupling length both are strongly dependent on each layer’s thickness and composition [117]. One way to overcome this problem is to introduce an absorption layer midway between the active and passive waveguides. Such “loss layer” suppresses lasing on the even mode and attenuates its interacting with the odd mode, making the TG laser’s facet reflectivity and coupling efficiency independent of length [117]. The concept of the absorption layer is very useful in laser design, but does not apply to a traveling-wave optical amplifier. In a single-pass device, the additional absorption is insufficient to remove the even mode [120].

Single-pass TG devices require a different approach to mode selection. Studenkov et al. [121] introduced an asymmetric twin guide (ATG) structure for an integrated optical amplifier. In a symmetric TG, both the even and odd modes have equal confinement factors in each waveguiding layer. Nearly complete power transfer takes place between the two waveguides. The maximum output coupling for either mode is 50%. In an ATG, the even and odd modes are split unequally between the waveguides due to the geometry of the design. For example, the thickness of the passive waveguide can be increased, so that the odd mode is largely confined to the active guide and the even mode is primarily confined to the passive guide [120]. The mode confined in the active WG experiences higher gain and higher reflectivity at the etched facets of an ATG laser, and therefore easily dominates [119]. In single-pass devices such as SOAs, the mode that resides in the passive portion of the TG can be ignored for sufficiently large lengths of the TG structure [120]. Unlike the TG with an absorbing layer, an ATG uses gain instead of loss as a mode-selection mechanism, thus allowing successful integration of SOAs with passive devices [101].

An undesirable consequence of asymmetric design is the poor coupling between the fundamental mode of the ATG structure residing primarily in the active waveguide and the mode of the passive waveguide [101]. Thus the original ATG design suffers from ~5-6 dB coupling loss at each active-passive junction [120]. Forrest at al. [122] demonstrated that introducing a lateral taper on the active waveguide drastically reduces the coupling loss and improves the quality of twin-waveguide junctions to be comparable to that of butt-coupled devices. Tapers also have been demonstrated to have extremely low reflection, making them an excellent choice for the SOA design [119, 122].

In the most current ATG implementations, the active waveguide typically resides on top of a passive waveguide [122]. The vertically-stacked waveguides separated by a cladding layer are strongly coupled. Lower, transparent waveguide layer has larger bandgap energy. It is used for on-chip optical interconnections between the active devices and passive light manipulation via etched ridge waveguides and related devices [120, 121]. Effective index of the passive waveguide has to be sufficiently lower than that of the active region so that the fundamental mode of the ATG section is well-confined in the active waveguide, but not too close to that of the substrate so that the fundamental mode of the purely passive section is also well-confined.

The tapered active waveguide is composed of material with a higher index of refraction than the lower transparent waveguide. As the active waveguide width is increased gradually by increasing the ridge width, the light confined in the underlying passive waveguide is transferred adiabatically to the active waveguide. Optimum taper shape is nonlinear so that the taper angle becomes smaller as the mode size increases. Such shape minimizes the radiation loss by not allowing the higher order modes to be excited [123]. Until recently, the taper couplers were designed using three-dimensional BPM modeling and simulations [119, 123, 124]. The same method is extensively employed in this work. The latest publication by Forrest et al. [101] present a novel taper coupler design algorithm using perturbation and coupled local mode theory.

Active components such as SOAs, distributed Bragg reflectors, and photodiodes can be integrated with passive components such as waveguides, Y-junctions, and MMI couplers. A variety of integrated optical devices can be fabricated from the same base heterostructure [121, 125-127].

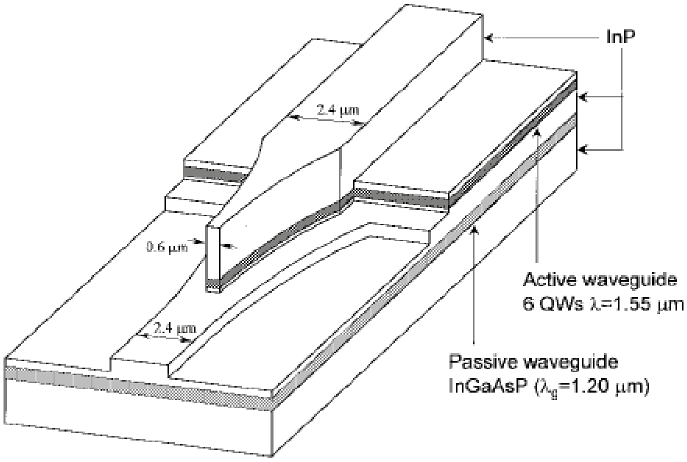

Figure 3-1. Asymmetric twin-waveguides structure [119].

The chief advantage of ATG approach is that provides low-loss, efficient coupling without the need for epitaxial regrowth as all the integrated components are defined by post-growth patterning and fabrication steps [121, 122]. The greatest challenge is the need for sub-micron lithography and precise alignment of active waveguide taper to the passive waveguide.

3.2 Main BPM examples—Optimization of Asymmetric Twin Waveguides

Beam propagation method is used to aid design of asymmetric twin waveguides and adiabatic tapers that facilitate mode optical energy transfer between the portions of the device. BPM is an appropriate tool because ATG structures with tapers are long and exhibit slow variation along the direction of propagation. BPM can be used because back reflections and beam divergence in such devices are low [128]. (Reflections from abrupt interfaces such as a blunt taper tip are accessed later by FDTD.)

The final design of the ATG structure presented in this work is a result of multiple rounds of optimization with respect to several dimensions of the structure's geometry. The resulting configuration is defined in Figure 3-2 (top view) and Figure 3-3 (cross-sectional view). The same structure is used to illustrate with simulations the principles of taper operation as well as the modeling procedures. The optimization process is illustrated in the following section 3.2.2. Parameters are varied one by one with respect to the base structure in order to justify the chosen values.

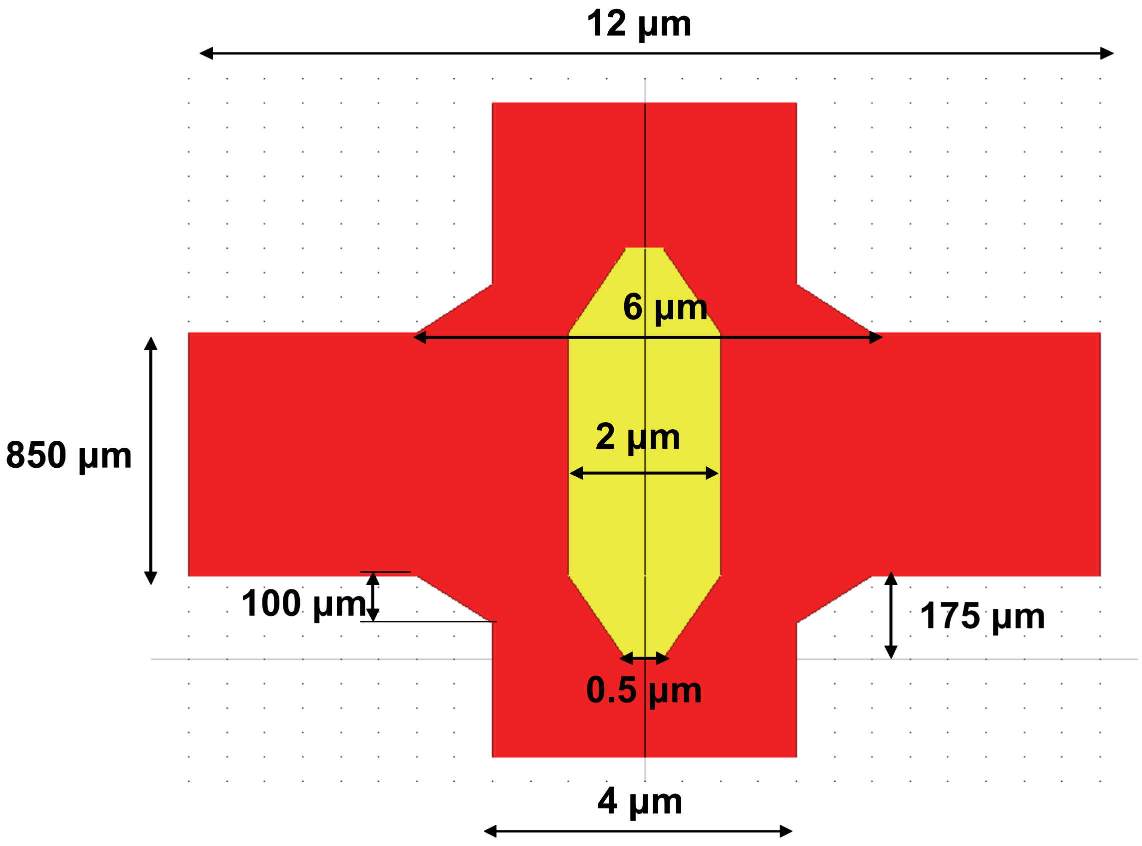

Figure 3-2. Lateral layout of tapered ATG structure.

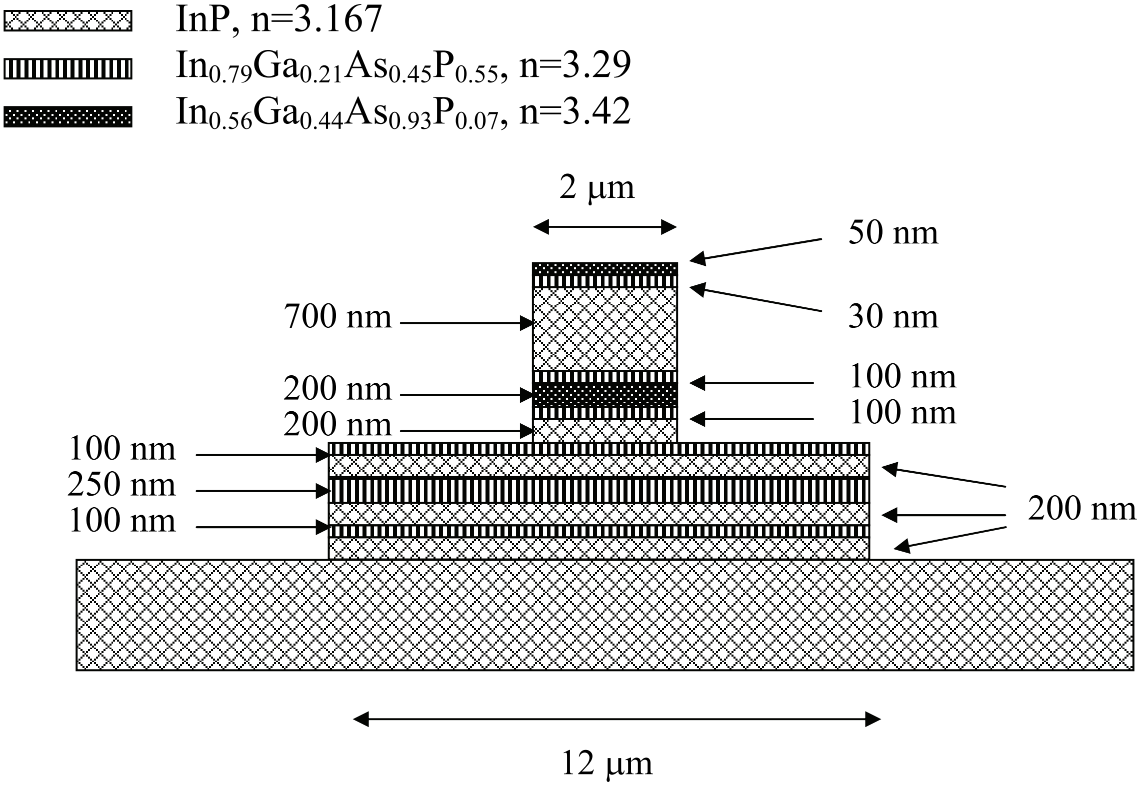

Figure 3-3. Cross-section of ATG structure.

3.2.1 Resonant and Adiabatic Couplers

There has been considerable confusion in describing the physical mechanism of optical transfer in taper waveguides as either resonant or adiabatic. This section addresses the following key facts: 1) symmetric TG structures rely on resonant coupling; 2) ATGs employ adiabatic taper couplers; 3) there is a “resonant point” along the adiabatic taper where scattering into higher-order modes is at its maximum [101].

In resonant couplers the power is split equally between the fundamental and first-order modes. Complete transfer of optical power between the waveguides is realized through beating between the two modes without scattering. The TG lasers described by Suematsu [129, 130] employ such coupling mechanism. As previously discussed in the description of symmetric taper couplers, while in theory resonant couplers are highly efficient, their fabrications tolerances are very poor [101].

Optical power transfer in ATG devices is realized by employing adiabatic taper couplers. For efficient adiabatic transfer, it is desirable that the structure supports only one mode throughout the coupling region. In some cases this condition cannot be satisfied. In particular, an ATG structure typically supports more than one mode because it includes a high-index upper waveguide placed on top of a single-mode passive waveguide. In such cases, an adiabatic structure needs to be designed in such a way that optical energy remains in the fundamental mode of the local structure and the higher-order modes are not excited. Optical power coupled to higher-order modes is negligibly small [131]. The tip of the taper coupler is sufficiently small to have little effect on the fundamental mode of the passive waveguide and can be viewed as a perturbation of the refractive index profile. While most of the optical power remains in the fundamental mode at all points along the taper coupler, a small amount of beating between the fundamental mode and higher order modes in the straight section beyond the taper is unavoidable due to finite length of a taper coupler [101].

The concept of resonant coupling is sometimes evoked to explain power transfer in adiabatic taper in the following manner [131]. Resonant coupling can be realized in structures that support two optical supermodes. Two waveguides comprising the structure have different dimensions and index of refraction of material. A taper can be formed so as to create a phase-matched condition at a certain width of the taper, often referred to as a resonant point. It is then claimed that the optical power transfer is realized by interaction of normal modes with very close propagation constants. The power transfer takes place over a relatively short coupling length determined by the difference in the modal propagation constants, typically several tens of microns [131].

Calculations show that the modes of ATG structure are most closely matched when the taper is just wide enough to support the second supermode. Figure 3-4 presents the effective indices of the two supermodes of the ATG structure as a function of taper width. It illustrates that the n_{eff} of two modes is the closest when the second supermode just becomes supported. For our layer structure and chosen passive waveguide dimensions, minimum Δn_{eff} occurs at taper width of 1.07 µm (Δn_{eff}=0.02295). Coupling length can be estimated by $L_c=\lambda/(2* \Delta n_{eff})$=33.7 µm. The two supermodes are shown in Figure 3-5.

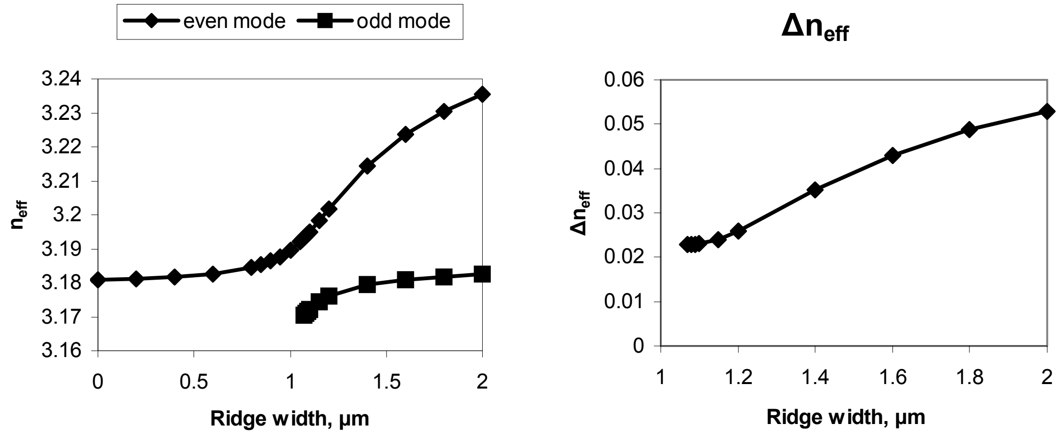

Figure 3-4. Effective indices of confined modes of ATG structure as a function of taper width.

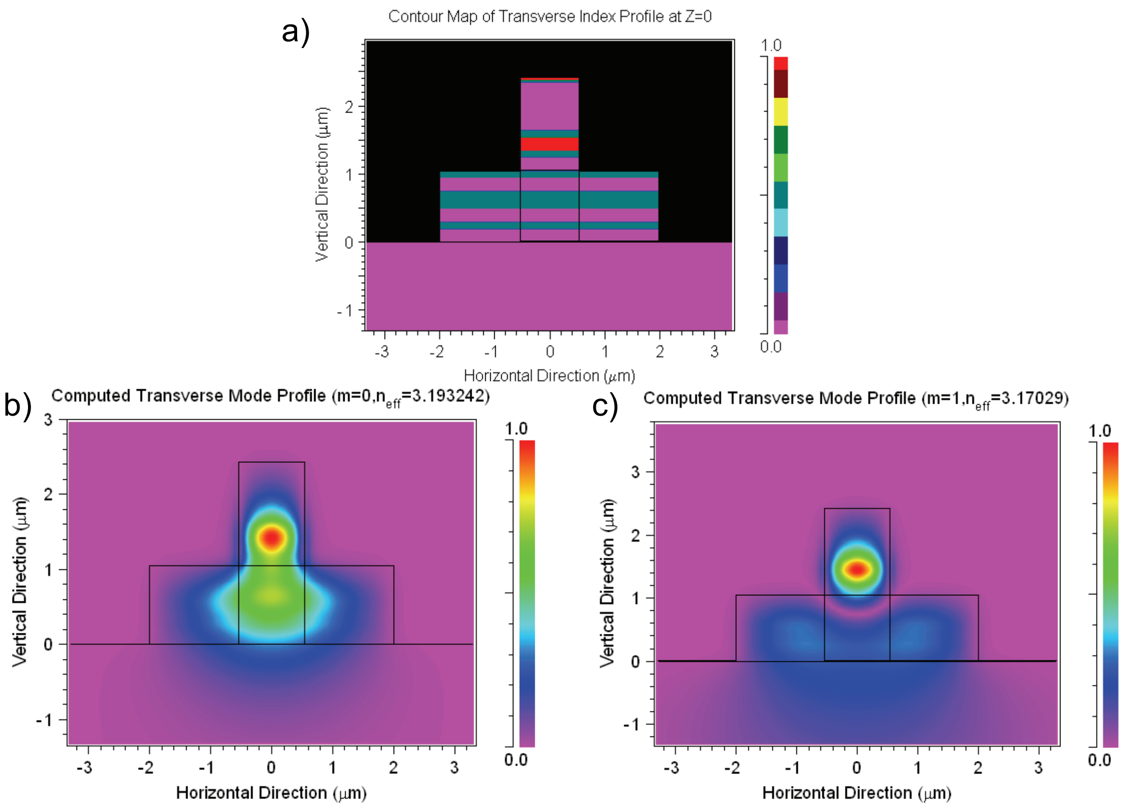

Figure 3-5. ATG structure begins to support the second mode at ridge width of 1.07 µm. a) Index profile, b) Fundamental mode, c) First-order mode.

Evoking normal modes to explain power transfer in adiabatic tapers is somewhat misleading. While there is a point along the taper where beating between the fundamental and first-order modes is maximized, coupling remains adiabatic as long as the taper width is varied slowly near this point. According to Xia et al. [101] scattering into higher-order mode is maximal around this point. He shows that the losses are minimized if the taper varies slowly around this point. The power in the fundamental mode experiences a slight decrease due to scattering around the resonance point, but some of the higher-mode power is scattered back into the fundamental mode further along the taper [101].

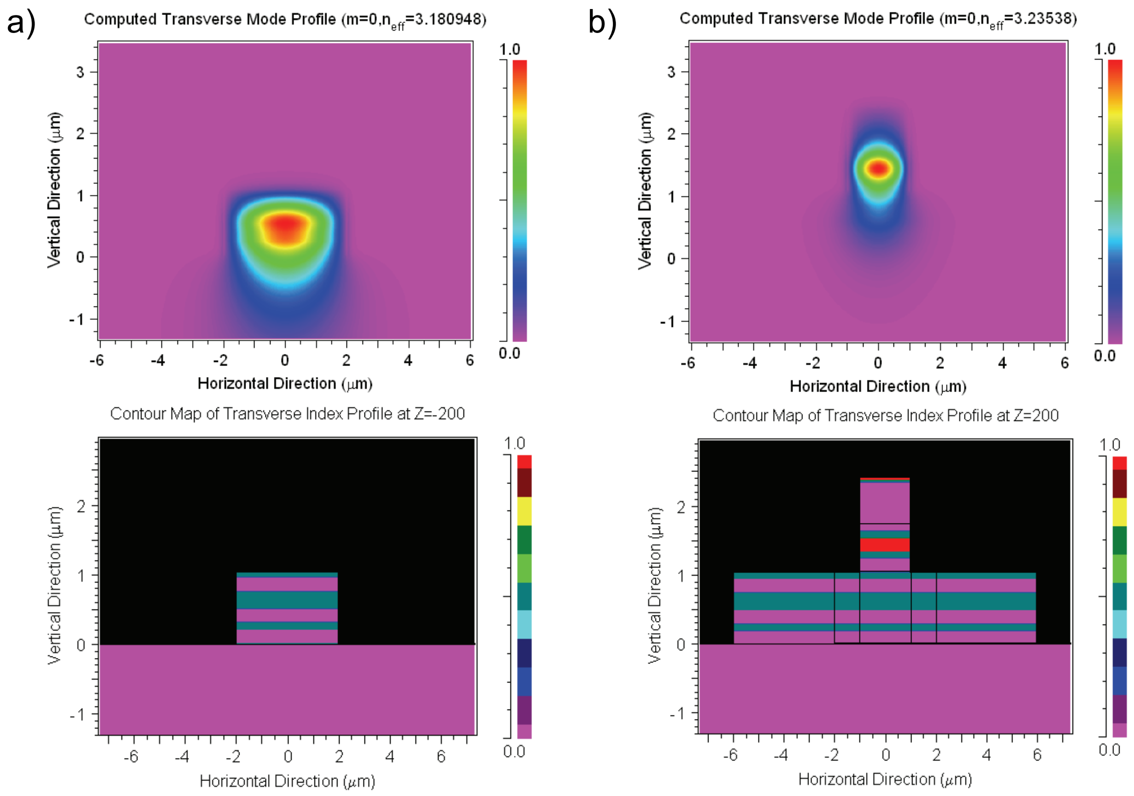

Figure 3-6. Fundamental modes of a) passive waveguide and b) ATG (with respective index profiles).

3.2.2 BPM simulations of adiabatic taper couplers

The following process is used to analyze coupling between passive waveguide and ATG via adiabatic tapers. First, BPM is used to solve for the fundamental modes of passive waveguides and full-width ATG (Figure 3-6). The fundamental mode of the passive waveguide is then launched into the passive waveguide and allowed to propagate through the tapered region into the full-width ATG section. The portion of energy in the fundamental mode of the ATG is monitored to access the success of the optical energy transfer (Figure 3-7).

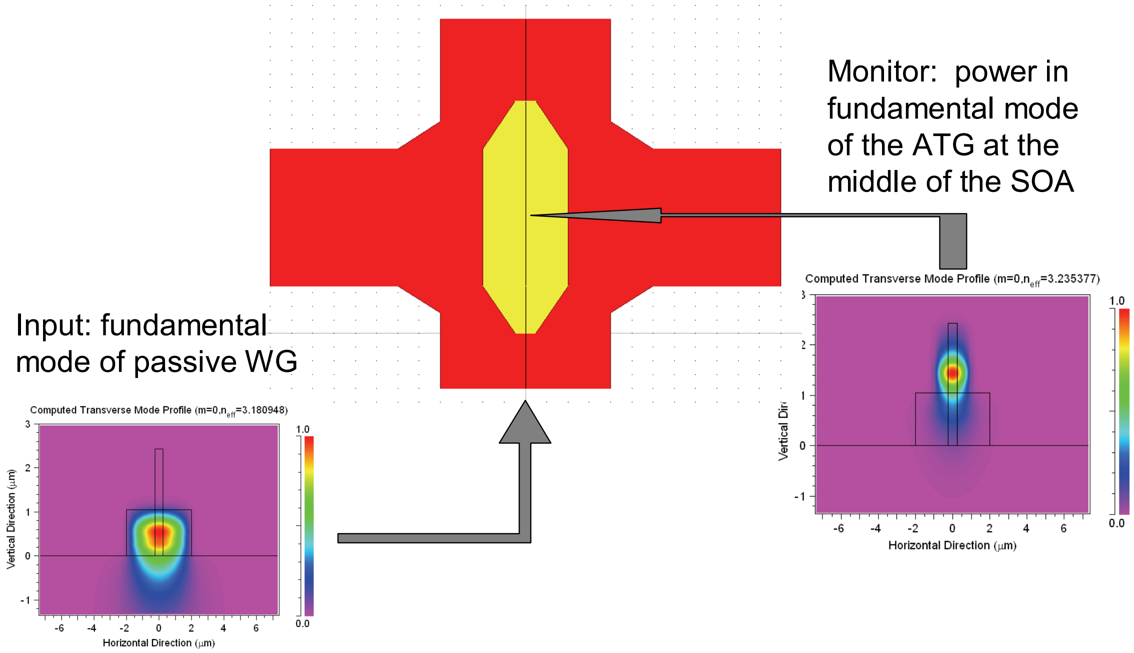

Monitor: power in fundamental mode of the ATG at the middle of the SOA

Input: fundamental mode of passive WG

Figure 3-7. Transfer of energy from passive guide to ATG.

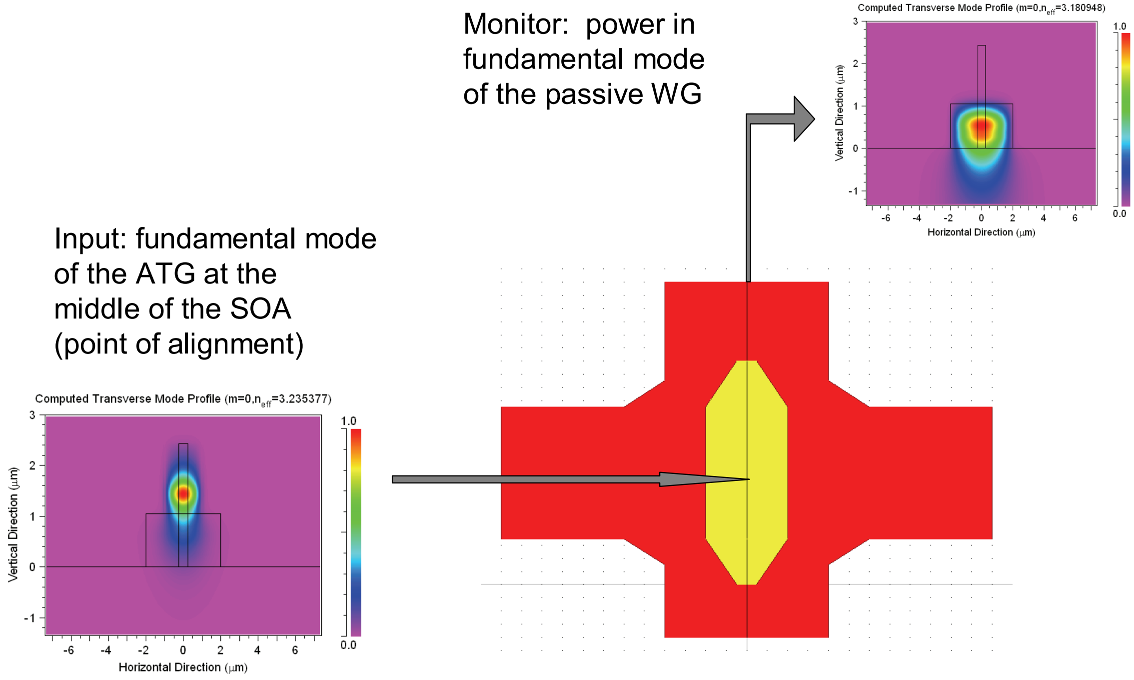

Monitor: power in fundamental mode of the passive WG

Input: fundamental mode of the ATG at the middle of the SOA (point of alignment)

Figure 3-8. Transfer of energy from ATG to passive waveguide.

Alternatively, the fundamental mode of the ATG structure is launched into the ATG and propagated through the tapered region where it is coupled to the passive waveguide. The fraction of power in the fundamental mode of the passive waveguide reflects the efficiency of the optical mode transfer (Figure 3-8).

While BPM is a highly appropriate tool for modeling taper couplers, as discussed above, RSoft BPM simulations revealed certain features and limitations that need to be addressed before we discuss parameter optimization. Figure 3-9 provides examples of results obtained by methods described in the previous paragraph and represented schematically in Figure 3-7 and Figure 3-8, respectively. Since tapers are reciprocal elements, coupling loss per transfer is expected to be the same for power transfer from passive to active guide and vice versa. However, BPM simulations show a small discrepancy: transfer from active to passive waveguide appears to involve approximately 0.1 dB more loss than transfer from passive to active guide. This discrepancy should most likely be attributed to imperfections in computation [132]. It also suggests that the calculated transfer efficiency figures are not highly accurate. They, however, can be successfully used to optimize the geometry of taper couplers [119, 123, 124].

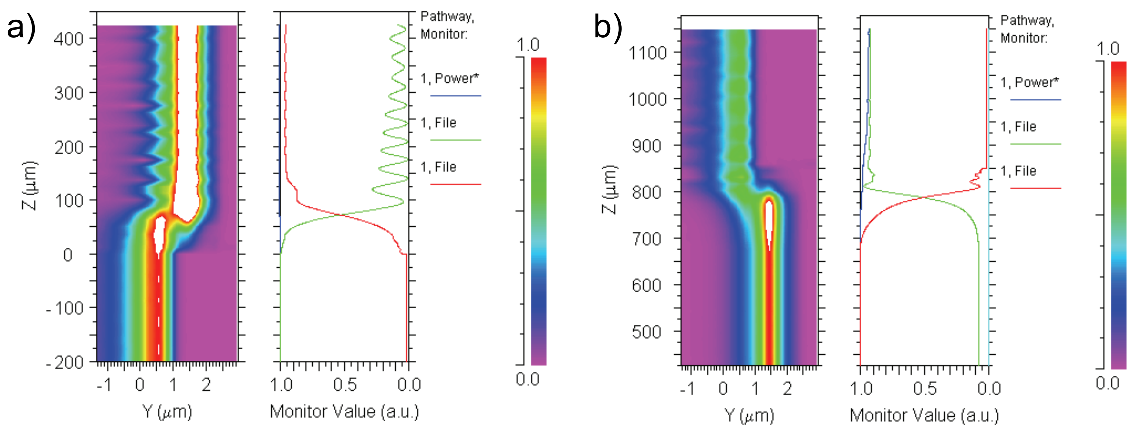

Blue—total power in the computational window
Green—power in fundamental mode of passive waveguide
Red—power in fundamental mode of full-width ATG structure

Figure 3-9. Examples of BPM simulations of optical power transfer a) from passive guide to ATG, b) from ATG to passive guide.

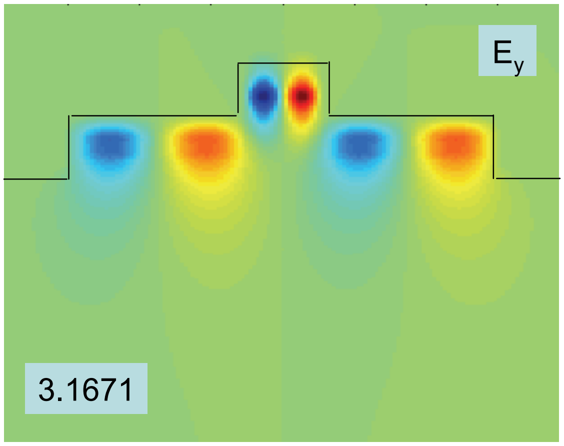

Figure 3-10. Highest-order mode of the double ridge.

Another manifestation of the same numerical problem is the apparent loss in total energy in the computational window on the transfer of optical power from active to passive waveguide. There is no corresponding loss in total power on the reciprocal transfer. It's also interesting to note small-scale oscillations in the optical power due to limited beating between the fundamental mode and higher order modes in the straight section of the ATG (Figure 3-8a) beyond the taper, as predicted discussed by Xia et al. [101]. The straight ATG section supports 13 modes: 7 TE modes and 6 TM modes. The highest-order mode has index just above that of InP substrate and is shown is Figure 3-10.

Now we illustrate optimization of taper couplers and assess their fabrication tolerances by means of BPM simulations. First, we show the importance of adiabatic tapers for optical power transfer between a passive waveguide and an SOA. We then proceed to compare effectiveness of tapers of different length. Next, we vary layer thicknesses to optimize vertical structure for the ATG. Finally, we evaluate robustness of taper couplers with respect to several likely imperfections in the fabrication process.

3.2.2.1 Simulation of ATG without tapers

In the absence of tapers, optical power is partially transferred from the passive WG to the active portion of the ATG due to the higher refractive index of the active device. The power transfer is not very efficient. In the literature, the coupling loss of 5-7 dB per transfer is cited. Our calculations confirm high coupling loss for the taper-less structure: less than 10% of optical power transfer from passive waveguide to ATG, corresponding to loss of over 10 dB.

3.2.2.2 Selection of taper length

It is clear that the adiabatic condition is easily satisfied by coupling by means of long, gentle tapers [101]. Slowly-varying taper width minimizes scattering of optical power from the fundamental mode into higher-order modes. On the other hand, compact couplers are essential for high-density PICs, and therefore tapers need to be designed as short as possible while preserving high efficiency. Figure 3-11 shows coupling efficiency of linear and exponential tapers as a function of taper length for coupler length between 75 and 250 µm. As expected, for both shapes transfer efficiency increases with taper length.

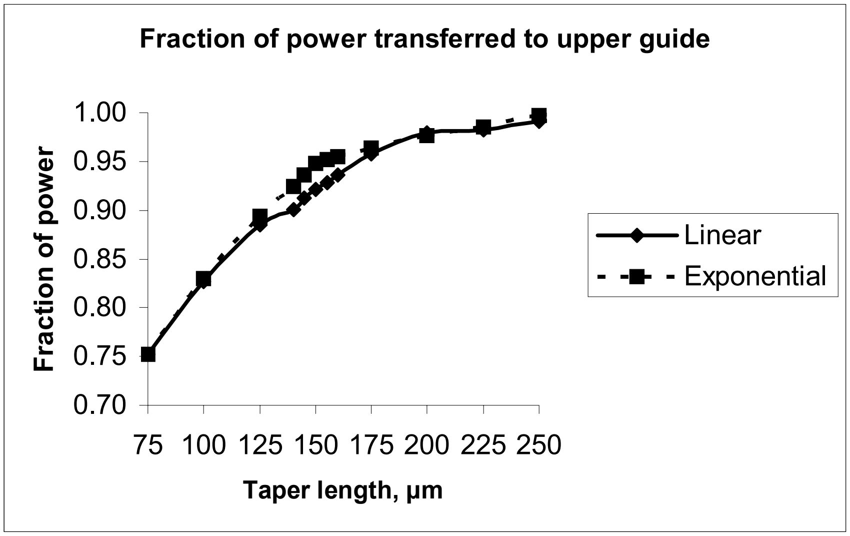

Figure 3-11. Coupling efficiency of linear and exponential tapers as a function of taper length.

Somewhat unexpectedly, linear and exponential tapers produce nearly the same results for tapers shorter than 125 µm and longer than 175 µm. This fact can be explained by arguing that in very short tapers, the adiabatic condition is violated for both taper shapes. Even for an exponential taper, the width does not change sufficiently gradually in order to prevent scattering of optical energy away from the local fundamental mode. Similarly, in long tapers the adiabatic condition is easily satisfied for both types of tapers. It is in tapers of intermediate length that exponential couplers display the greatest advantage over linear ones, showing a maximum of approximately 0.13 dB less loss for a 150 µm-long taper.

Taking into consideration the tradeoff between taper length and coupling efficiency, we chose a 175 µm-long taper. Both linear and exponential tapers of this length boast efficiency of about 96%. Beyond this length, the increase in coupling efficiency with taper length becomes small. In addition, the advantage of an exponential taper at the chosen length is insignificant, and the decision was made to use linear tapers for ease of fabrication and mask design.

3.2.2.3 Selection of layer geometry

This section addresses optimization of parts of the layered structure of the upper guide for good coupling between the passive and active waveguides. The core InGaAsP layers are designed for optical and electrical confinement (cladding layers), and nonlinear functions such as amplification (active layer). The topmost layers are included specifically for creating a better p-type contact to the upper ridge. Two remaining InP layers are designated as “spacer” and “cap” (Figure 3-12). Their respective thicknesses are varied and taper coupler efficiency is examined as a function of each thickness.

The fraction of power coupled into the fundamental mode of the full-width ATG structure from the passive waveguide as a function of cap layer thickness is shown in Figure 3-13. Within the limits of the simulation precision, essentially all power is successfully transferred to the upper guide for cap layer thickness of 100 nm. Increasing the cap layer thickness causes a slight drop in the fraction of transferred power.

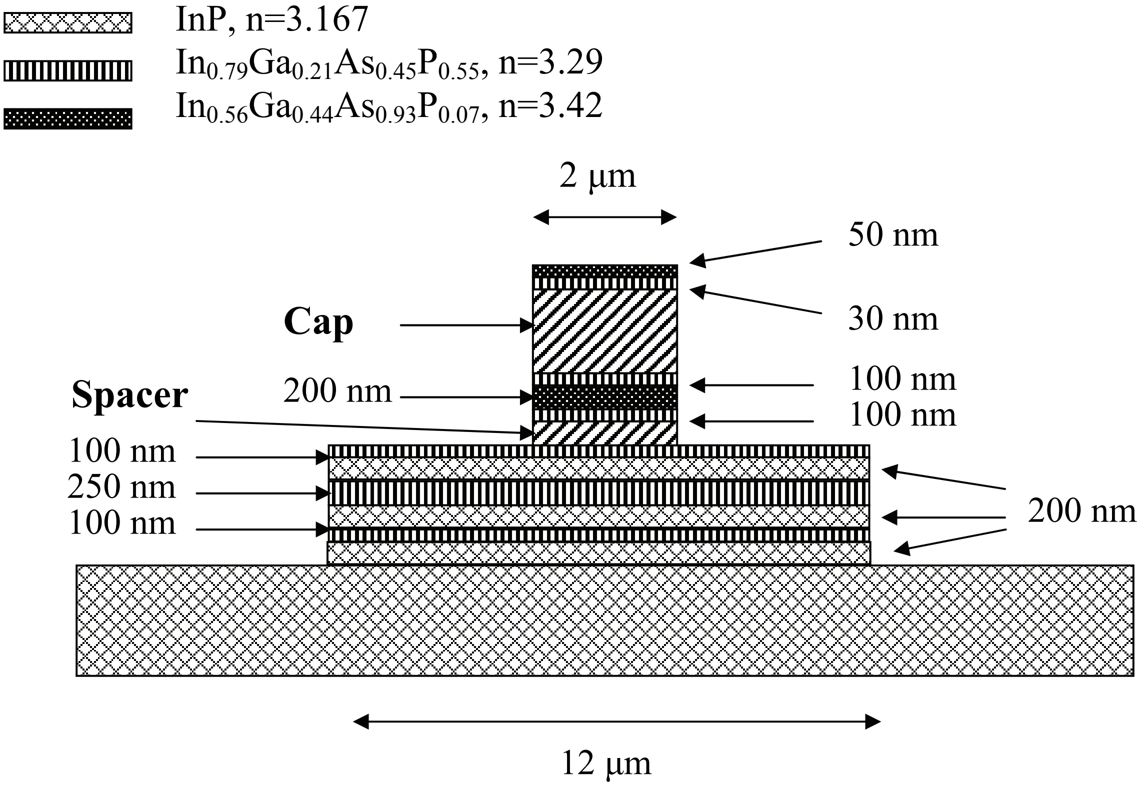

Figure 3-12. Cross-section of ATG structure with variable spacer and cap layers.

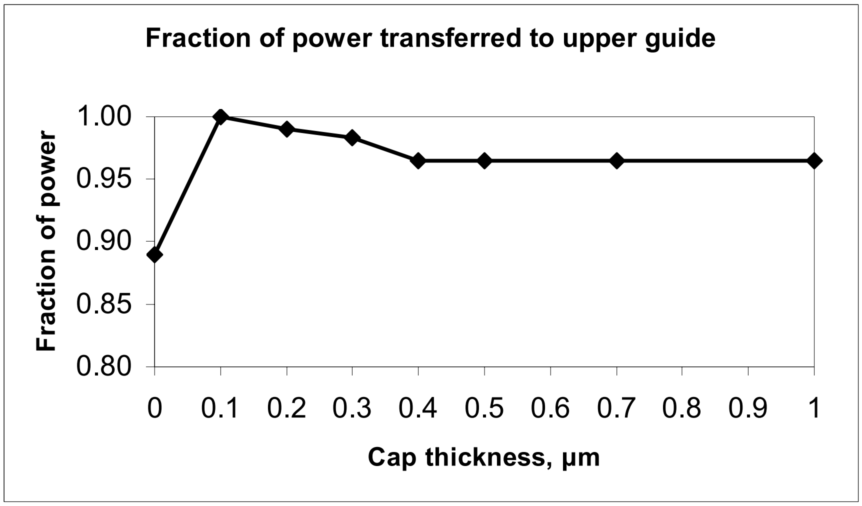

Figure 3-13. Coupling efficiency as a function of cap layer thickness.

Coupling efficiency as a function of spacer layer thickness is examined while setting cap layer thickness to 100 nm. It is evident from Figure 3-14 that varying spacer layer between 0 and 200 nm maintains the optimal coupling efficiency.

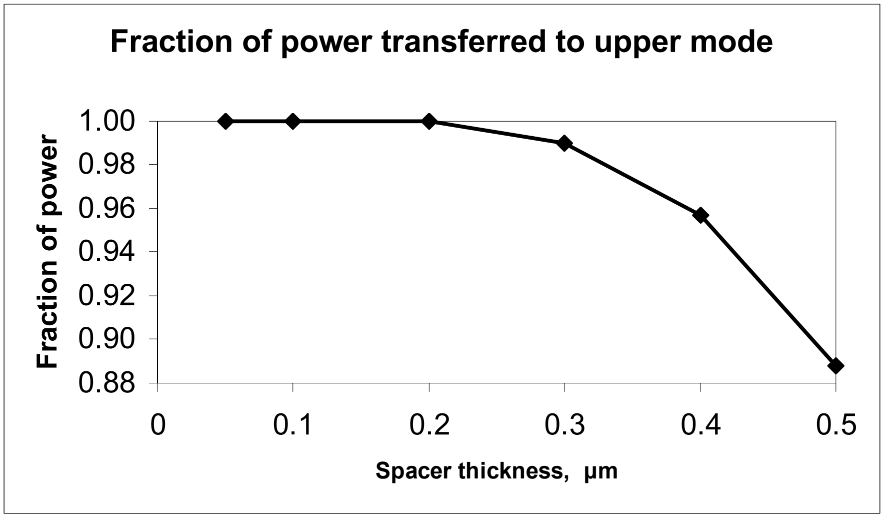

Figure 3-14. Coupling efficiency as a function of spacer layer thickness.

The study of coupling efficiency as a function of spacer and cap thicknesses is presented above as an example of the design and optimization procedures for adiabatic taper couplers using beam propagation techniques. In practice, optimization results have to be combined with fabrication considerations. This process can also be illustrated by choices we made for the final design of the layered structure. In particular, cap layer thickness of 700 nm was chosen due to two additional considerations: 1) removing highly doped top contact layers farther from the core of the optical mode to prevent losses, and 2) keeping the ridge height moderate (on the order of one micron) for ease of etching. Optimization calculations ensure that increase in cap layer thickness leads only to a moderate reduction in coupling efficiency. Figure 3-15 and especially Figure 3-16 demonstrate that optical power in the contact layers is significantly reduced by increasing cap layer thickness.

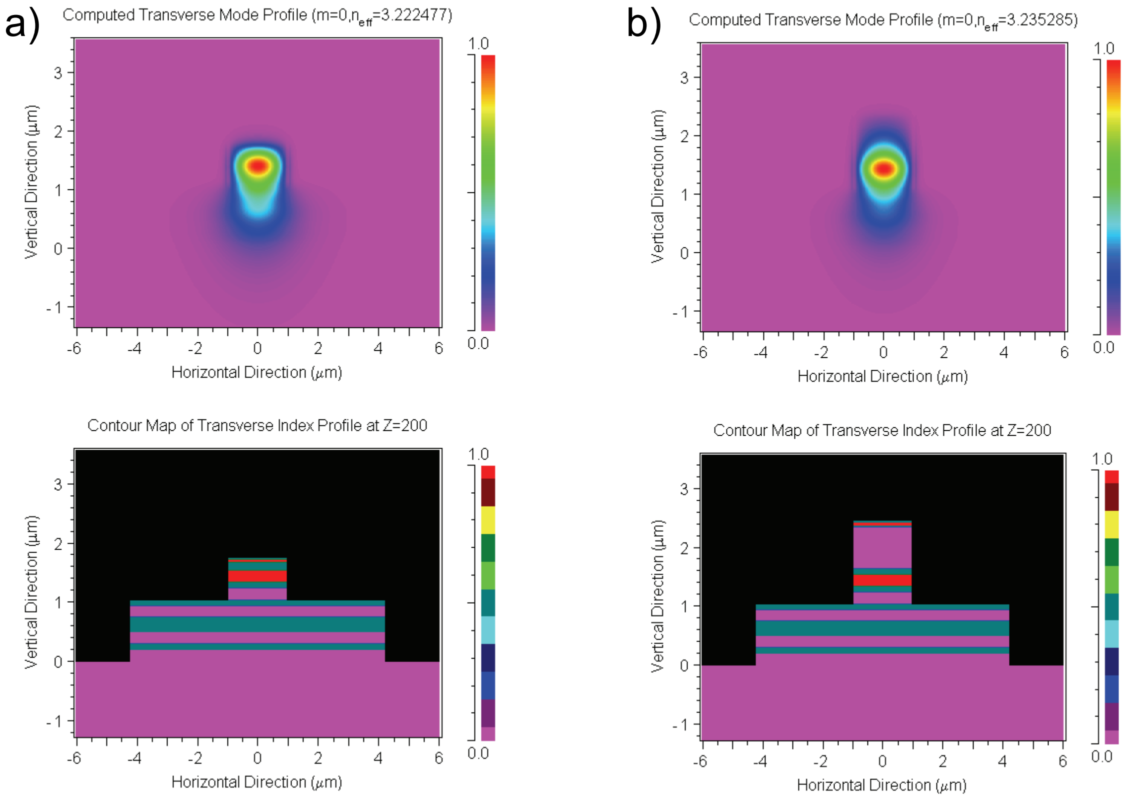

Figure 3-15. Fundamental mode of ATG for cap thickness of a) zero, b) 0.7 µm.

Likewise, spacer layer thickness of 200 nm was chosen with ridge fabrication needs in mind. The narrow upper ridge is to be fabricated by reactive ion etching with the etch terminating within the spacer layer. The upper ridge fabrication is completed with a selective wet etch where the top InGaAsP layer of the passive waveguide acts as an etch stop.

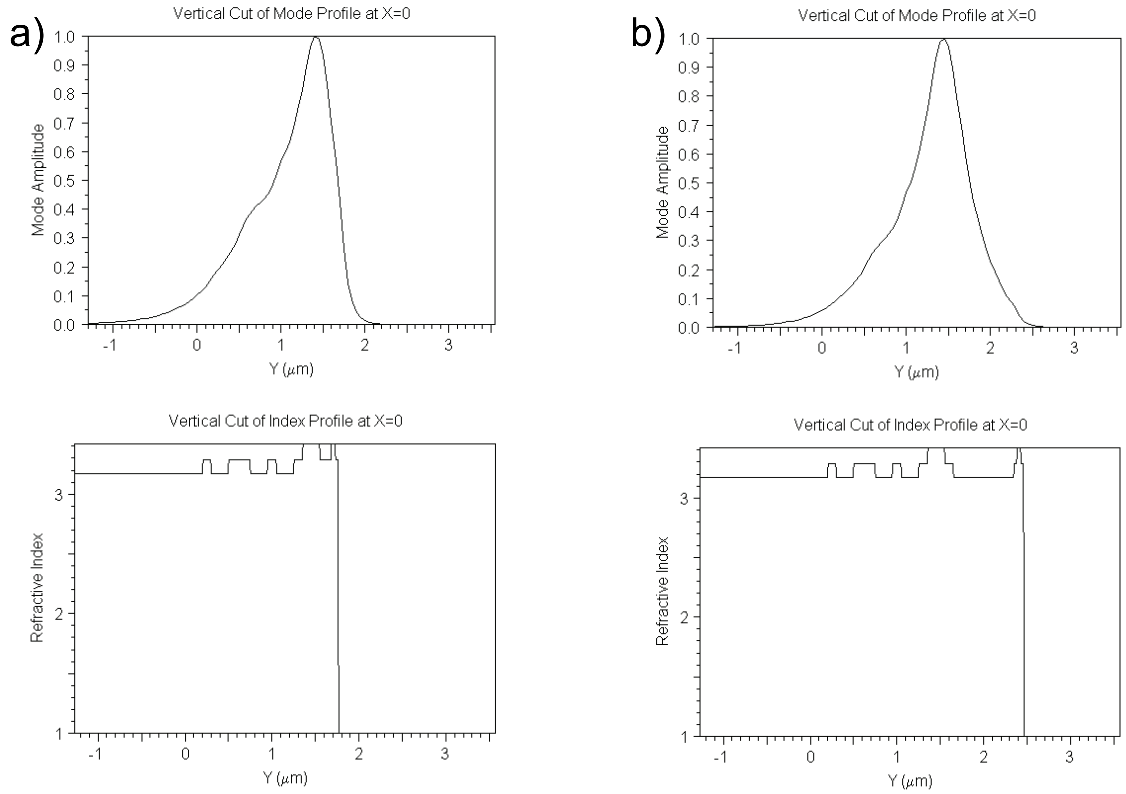

Figure 3-16. Cross-sectional view of fundamental mode of ATG for cap thickness of a) zero, b) 0.7 μm.

3.2.2.4 Robustness of ATG taper couplers with respect to fabrication variations

In this section we look at several likely imperfections of the double ridge fabrication process and their effect on coupling efficiency. First, there is a possibility of overetching the upper ridge which would result in reduction of the ridge width by the same amount both in the straight ATG section and in taper couplers. Figure 3-17 shows coupling efficiency as a function of upper ridge width reduction by up to 0.5 μm. There is an insignificant decrease in efficiency for width reduction of 0.3 μm and below.

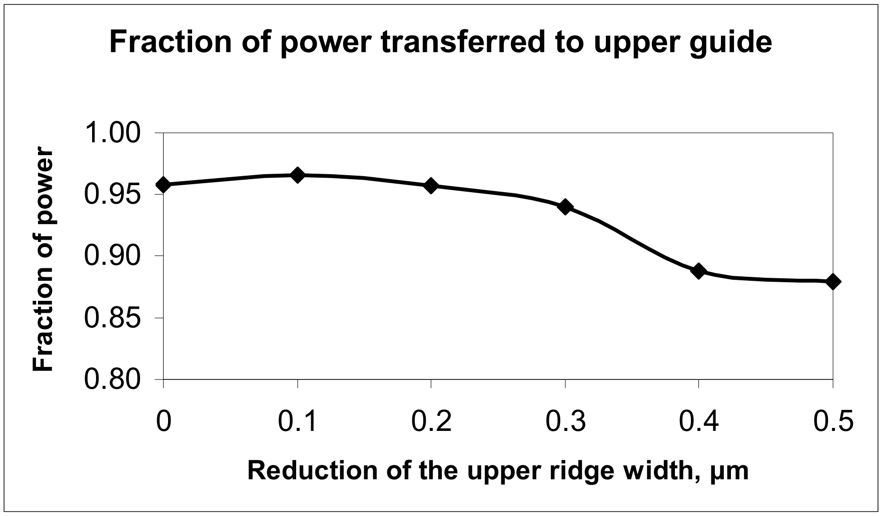

Figure 3-17. Coupling efficiency as a function of reduction in upper ridge width.

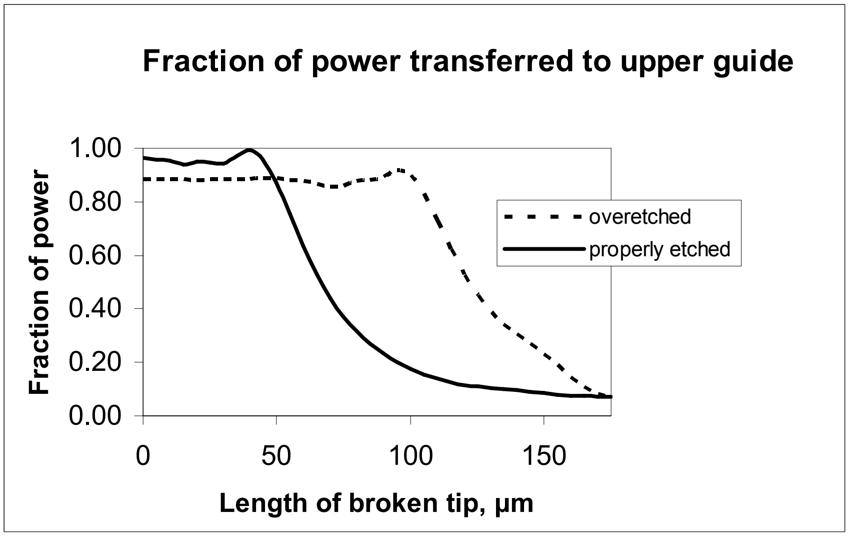

Figure 3-18. Coupling efficiency as a function of the missing length of the taper.

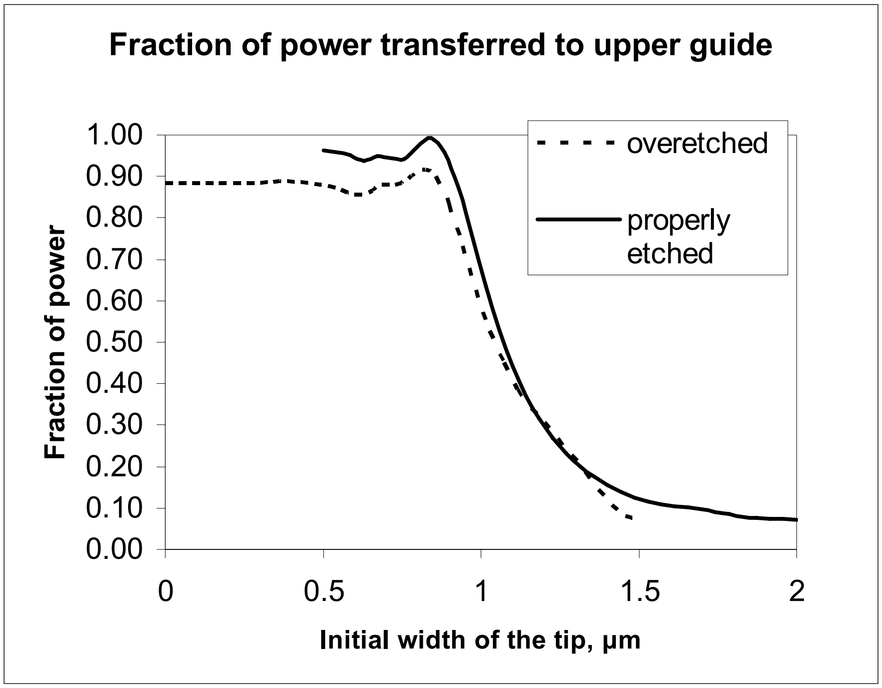

Figure 3-19. Coupling efficiency as a function of the initial width of the taper.

The very thin initial portion of the taper may break off, reducing the overall length of the taper. Such possibility becomes even more likely when the upper ridge is overetched, as described above. Figure 3-18 shows coupling efficiency as a function of the missing length of the taper. In order to interpret the results, it helps to look at the transfer efficiency as a function of initial tip width (Figure 3-19). On this plot we notice good agreement between the curves for overetched and properly etched devices. This suggests that it is the initial width of the taper which determines coupler efficiency for a fixed slope of a linear taper. According to Figure 3-19, most efficient tapers have initial width of ~0.8 µm. Note that the taper increases in width from 0.8 µm to the resonance point of 1.07 µm in approximately 35 µm, in agreement with the above predictions based on coupling length calculations. Tapers that start at a smaller width display nearly constant efficiency as a function of width, while efficiency falls off sharply for tapers starting at width over 0.9 µm. This is an encouraging result since it seems unlikely that a taper tip breaks off at a point where it is nearly a micron wide.

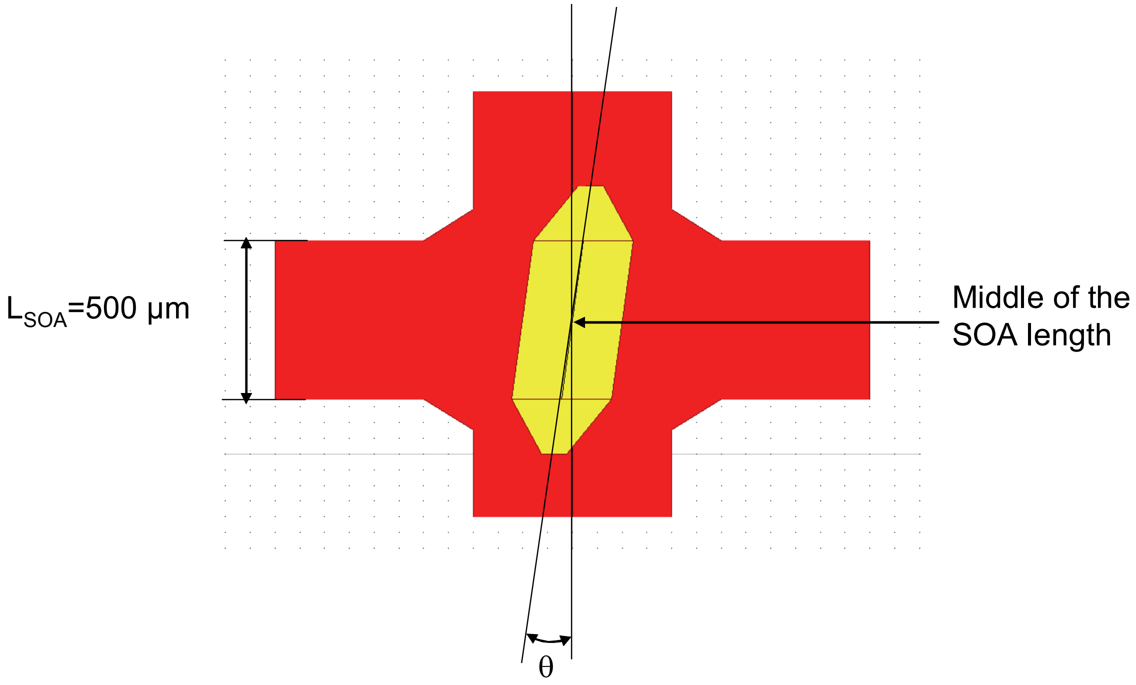

Figure 3-20. Rotational misalignment of the upper ridge (taper length = 175 µm, SOA width = 2 µm, cap width = 2 µm).

Finally, we look at a possibility of rotational misalignment between the lower and the upper ridges of an ATG. It is clear from the long and narrow geometry of the device (Figure 3-20) that a significant rotational misalignment is more likely to occur for shorter length of the straight ATG section (in our devices, the SOA length). Therefore we chose a somewhat shorter straight section—500 µm. For the sake of simplicity, we look at misalignment with respect to the center of the device. As with longer devices, rotation of the upper mask with respect to another point will be more easily detected and corrected as it will produce a stronger deviation in the position of one of the taper tips. In the case of the device in Figure 3-20, a 0.5 µm lateral deviation of a taper end corresponds to ~0.07° rotation of the upper ridge with respect to the center of the straight section.

According to Figure 3-21, deterioration of transmission performance for rotation in this range is insignificant.

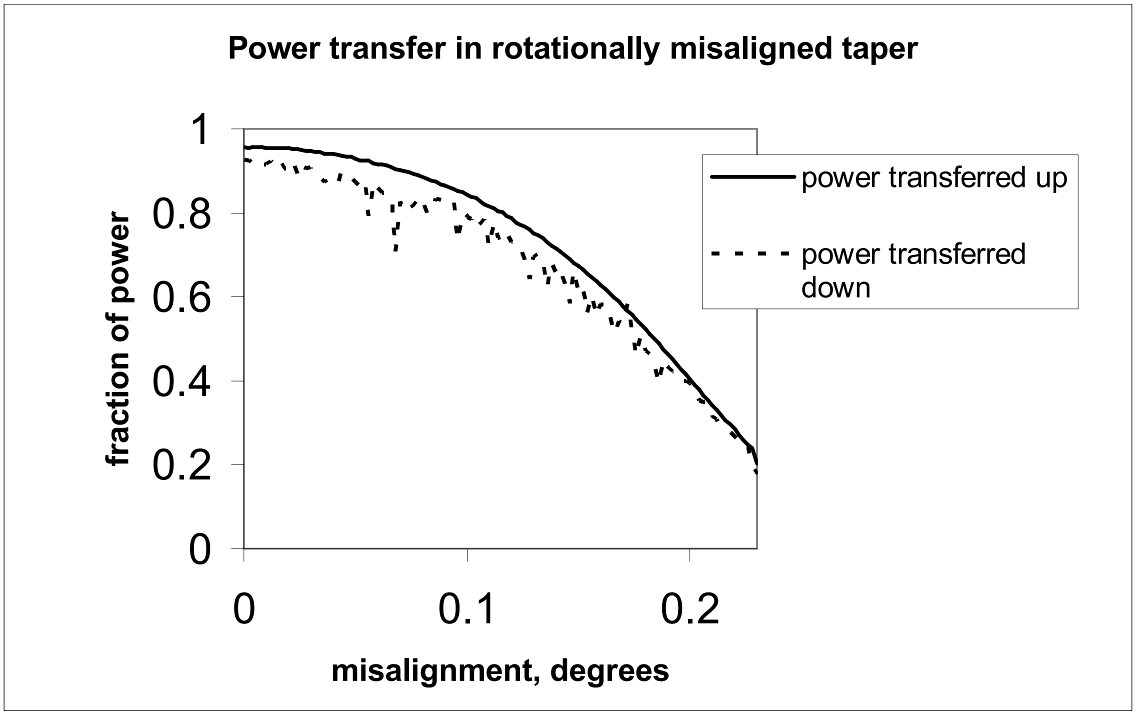

Figure 3-21. Coupling efficiency as a function of misalignement angle.

3.2.2.5 Triple ridges

There is a variation to ATG geometry that can help reduce waveguide losses by confining most of optical power away from the potentially rough walls of the ridge waveguide. In this variation, the cap and contact layers form a narrow ridge as before, but the spacer and active and cladding layers of the SOA form a ridge of intermediate width—wider that the cap ridge, but narrower than the passive waveguide ridge. Figure 3-22 shows the fundamental mode of the ATG for four variations in the structure. In cases when an intermediate ridge is present, less optical power is incident on waveguide walls. Confinement factor, that is, a fraction of power in the optical mode that overlaps with the active layer, has approximately the same value of ~0.4 for all of four structures. Confinement factor is an important parameter in SOA design which will be addressed in the following chapter. The main disadvantage of the three-ridge design is the need for more complicated fabrication process, as it requires an additional mask layer, alignment and processing steps.

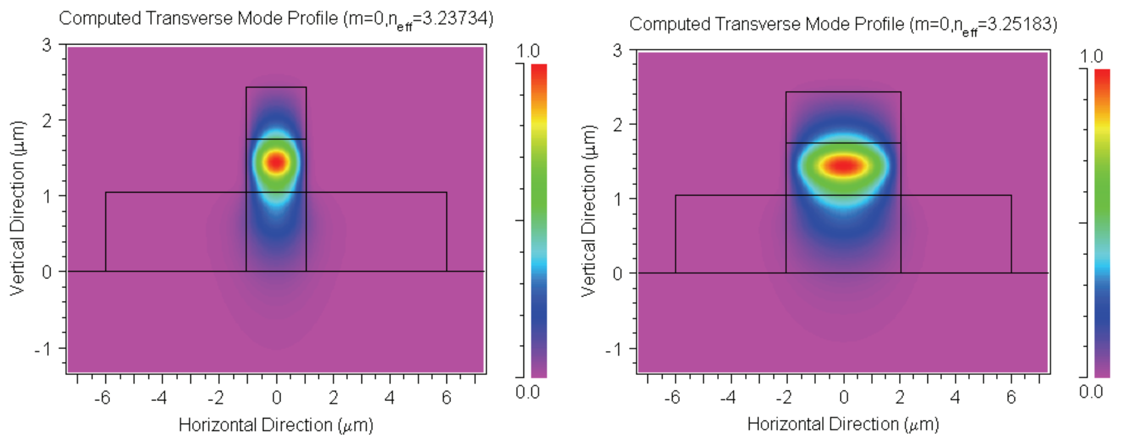

SOA width=2 µm, cap width=2 µm

SOA width=4 µm, cap width=4 µm

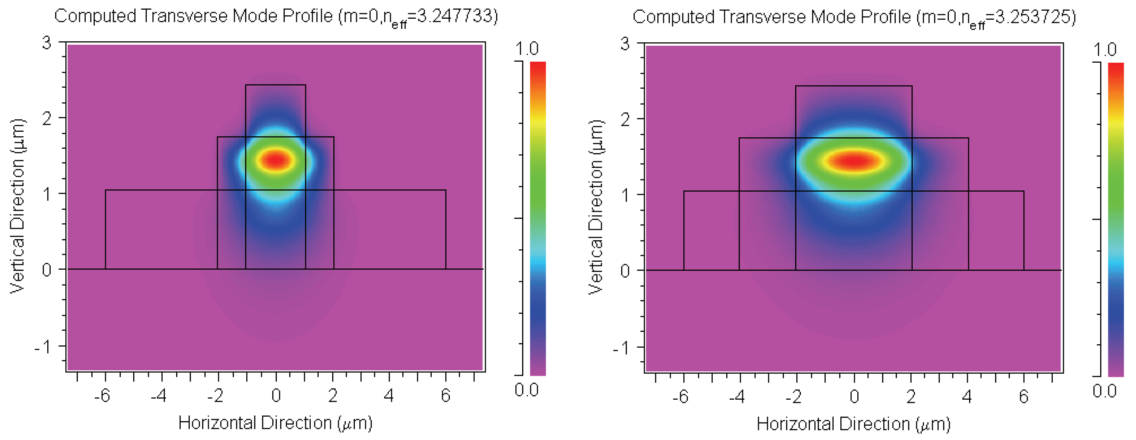

SOA width=4 µm, cap width=2 µm

SOA width=8 µm, cap width=4 µm

Figure 3-22. Fundamental mode of ATG for several variations of ridge geometry.

3.3 Finite Difference Time Domain Method

Finite-difference time-domain algorithms provide a direct solution of Maxwell's time-dependent curl equations which in this case are represented as a system of coupled partial differential equations:

$$\frac{\partial H_x}{\partial t} = \frac{1}{\mu}\left(\frac{\partial E_y}{\partial z} - \frac{\partial E_z}{\partial y} - \rho' H_x\right)$$

$$\frac{\partial H_y}{\partial t} = \frac{1}{\mu}\left(\frac{\partial E_z}{\partial x} - \frac{\partial E_x}{\partial z} - \rho' H_y\right)$$

$$\frac{\partial H_z}{\partial t} = \frac{1}{\mu}\left(\frac{\partial E_x}{\partial y} - \frac{\partial E_y}{\partial x} - \rho' H_z\right)$$

$$\frac{\partial E_x}{\partial t} = \frac{1}{\varepsilon}\left(\frac{\partial H_z}{\partial y} - \frac{\partial H_y}{\partial z} - \sigma E_x\right)$$

$$\frac{\partial E_y}{\partial t} = \frac{1}{\varepsilon}\left(\frac{\partial H_x}{\partial z} - \frac{\partial H_z}{\partial x} - \sigma E_y\right)$$

$$\frac{\partial E_x}{\partial t} = \frac{1}{\varepsilon}\left(\frac{\partial H_y}{\partial x} - \frac{\partial H_x}{\partial y} - \sigma E_z\right) \qquad \text{(Eq. 3-1)}$$

where E_x, E_y, E_z are the Cartesian components of electrical field, H_x, H_y, H_z are the Cartesian components of magnetic field, ε is the electric permittivity, σ is the electric conductivity, μ is the magnetic permeability, and ρ' is the equivalent magnetic loss.

The 3D computational domain is divided into a grid, rectangular in the simplest case. Given the electrical and magnetic properties of the medium at every spatial point and the initial field distribution (or a source excitation), the field components at each location are updated for the following time step according to Yee's algorithm [133].

A space point in a uniform, rectangular lattice is denoted by,

$$(i, j, k) = (i\Delta x, j\Delta y, k\Delta z) \qquad \text{(Eq. 3-2)}$$

where Δ*x*, Δ*y*, and Δ*z* are the lattice space increments in the *x*, *y*, and *z* coordinate directions, respectively, and *i*, *j*, and *k* are integers. We denote any function *F* of space and time evaluated at a discrete point in the grid at a discrete point in time as

$$F^n(i, j, k) = F(i\Delta x, j\Delta y, k\Delta z, n\Delta t) \, . \qquad \text{(Eq. 3-3)}$$

Yee's algorithm uses central-difference expressions for space and time derivatives that are second-order accurate in the space and time increments. For example, first partial space derivative of *F* in the *x*-direction evaluated at time $t_n = n\Delta t$ is given by

$$\frac{\partial F^n(i, j, k)}{\partial x} = \frac{F^n(i + \frac{1}{2}, j, k) - F^n(i - \frac{1}{2}, j, k)}{\Delta x} + order(\Delta x^2) \, . \qquad \text{(Eq. 3-4)}$$

By analogy, expression for the first time derivative of F evaluated at the fixed space point *(i, j, k)* is as follows:

$$\frac{\partial F^n(i, j, k)}{\partial t} = \frac{F^{n+\frac{1}{2}}(i, j, k) - F^{n-\frac{1}{2}}(i, j, k)}{\Delta t} + order(\Delta t^2) \, . \qquad \text{(Eq. 3-5)}$$

Here are examples of difference equations obtained by applying the above notation to Equations 3-1:

$$H_x^{n+\frac{1}{2}}\left(i,j+\frac{1}{2},k+\frac{1}{2}\right)=H_x^{n-\frac{1}{2}}\left(i,j+\frac{1}{2},k+\frac{1}{2}\right)+$$

$$\frac{\Delta t}{\mu\left(i,j+\frac{1}{2},k+\frac{1}{2}\right)}\left[\begin{array}{l}\frac{1}{\Delta z}\left(E_y^n\left(i,j+\frac{1}{2},k+1\right)-E_y^n\left(i,j+\frac{1}{2},k\right)\right)+\\ \frac{1}{\Delta y}\left(E_z^n\left(i,j,k+\frac{1}{2}\right)-E_z^n\left(i,j+1,k+\frac{1}{2}\right)\right)\end{array}\right]$$

$$E_x^{n+1}\left(i,j,k+\frac{1}{2}\right)=\frac{1-\frac{\sigma\left(i,j,k+\frac{1}{2}\right)\Delta t}{2\varepsilon\left(i,j,k+\frac{1}{2}\right)}}{1+\frac{\sigma\left(i,j,k+\frac{1}{2}\right)\Delta t}{2\varepsilon\left(i,j,k+\frac{1}{2}\right)}}E_z^n\left(i,j,k+\frac{1}{2}\right)+\frac{1}{1+\frac{\sigma\left(i,j,k+\frac{1}{2}\right)\Delta t}{2\varepsilon\left(i,j,k+\frac{1}{2}\right)}}\times$$

$$\frac{\Delta t}{\varepsilon\left(i,j,k+\frac{1}{2}\right)}\left[\begin{array}{l}\frac{1}{\Delta x}\left(H_y^{n+\frac{1}{2}}\left(i+\frac{1}{2},j,k+\frac{1}{2}\right)-H_y^{n+\frac{1}{2}}\left(i-\frac{1}{2},j,k+\frac{1}{2}\right)\right)+\\ \frac{1}{\Delta y}\left(H_x^{n+\frac{1}{2}}\left(i,j-\frac{1}{2},k+\frac{1}{2}\right)-H_x^{n+\frac{1}{2}}\left(i,j+\frac{1}{2},k+\frac{1}{2}\right)\right)\end{array}\right] \qquad \text{(Eq. 3-6)}$$

All quantities on the right-hand side of a difference equation are known from the previous computational step. Chronological values of the electric and magnetic field components at each point are obtained in a leapfrog manner with respect to time. That is, the electric field is found at a given point in time and the magnetic field is computed for the next point in time, repeatedly. As mentioned earlier, the electric field is obtained from the previous value of the electric field and the difference in the previous values of the magnetic field on either side of the electric field point in space. Likewise, the magnetic field is found from the earlier value of the magnetic field and the difference between the earlier-time values of the electric field on either side of the magnetic field point in space [134].

It is worth mentioning the particular strengths of the Yee algorithm that made it a standard and preferred technique in FDTD. First of all, the algorithm is robust because it solves for both electric and magnetic fields in time and space using Maxwell's equations instead of solving for the electric (or magnetic) field alone using a wave equation. Second, the Yee algorithm centers the electric and magnetic field components in the 3D domain so that every electric field components is surrounded by four circulating magnetic field components, and every magnetic field component is surrounded by four circulating electric field components. Thus, the 3D space is filled by interlinked Faraday's Law and Ampere's Law contours. That is, the Yee algorithm effectively simulates the differential and the integral form of Maxwell's equations simultaneously. For interfaces between different materials parallel to one of the grid coordinate axes, continuity of tangential electric and magnetic field is maintained without a need to specifically enforce field boundary conditions at the interface. Third, in addition to being nondissipative, the leapfrog time-stepping is fully explicit and does not require matrix inversion [135].

Stability of the algorithm requires a proper choice of the time step Δt in relation to the spatial steps Δx, Δy, and Δz. It can be shown that the stability condition is satisfied by the following relationship:

$$c\Delta t \leq \frac{1}{\sqrt{\frac{1}{(\Delta x)^2} + \frac{1}{(\Delta y)^2} + \frac{1}{(\Delta z)^2}}} \qquad \text{(Eq. 3-7)}$$

also known as the Courant-Friedrich-Levy (CFL) criterion. For a cubic lattice, $\Delta x=\Delta y=\Delta z=\Delta$ and Eq. 3-7 is simplified to

$$\Delta t \leq \frac{\Delta}{c\sqrt{3}} . \qquad \text{(Eq. 3-8)}$$

More complicated conditions may be required for stability of the FDTD algorithm if variable or unstructured meshing is used [128].

3.3.1 Perfectly Matched Layer boundary conditions

As with the BPM and other numerical methods, FDTD calculations require a careful choice of boundary conditions on the edge of a finite simulation domain. Absorbing Boundary Condition described above during discussion of BPM was originally applied to FDTD as well. The ABCs are effective in suppressing reflections for light impinging on the boundary close to normal incidence, but often fail for radiation incident on the boundary at oblique angles. Such unphysical reflections distort and destabilize simulation results and should be avoided [128]. In addition, satisfactory solutions using ABCs require that the absorbing boundaries are placed at a considerable distance from the scattering structure. This increases computational domain significantly, with the major portion of the domain representing vacuum around the object of interest [136].

In 1994 Berenger proposed a novel approach to setting boundary conditions for free-space simulations called Perfectly Matched Layer (PML) approach [137]. The PML technique dramatically reduces unwanted reflections for all angles of incidence through the use of specially-designed absorbing layers to simulate free space outside of the computational domain. Unlike in the case of the ABCs, excellent results can be obtained with the PML boundary placed very close to the scatterer, reducing the computational domain. However, care must be taken to choose the absorbing layer properties appropriately. An unsatisfactory choice can result either in a faulty answer or in unnecessarily heavy use of computational resources [136].

An artificial anisotropic absorbing material surrounding the simulation domain is assigned both electric and magnetic conductivities. Inside the PML, each electromagnetic field component is split into two parts. Six field components result in 12 subcomponents: E_{xy}, E_{xz}, E_{yz}, E_{yx}, E_{zx}, E_{zy}, H_{xy}, H_{xz}, H_{yz}, H_{yx}, H_{zx}, H_{zy}. The Maxwell equations are replaced by 12 equations as follows:

$$\varepsilon\frac{\partial E_{xy}}{\partial t}+\sigma_y E_{xy}=\frac{\partial\left(H_{zx}+H_{zy}\right)}{\partial y}$$

$$\varepsilon\frac{\partial E_{xz}}{\partial t}+\sigma_z E_{xz}=-\frac{\partial\left(H_{yz}+H_{yx}\right)}{\partial z}$$

$$\varepsilon\frac{\partial E_{yz}}{\partial t}+\sigma_z E_{yz}=\frac{\partial\left(H_{xy}+H_{xz}\right)}{\partial z}$$

$$\varepsilon\frac{\partial E_{yx}}{\partial t}+\sigma_x E_{yx}=-\frac{\partial\left(H_{zx}+H_{zy}\right)}{\partial x}$$

$$\varepsilon\frac{\partial E_{zx}}{\partial t}+\sigma_x E_{zx}=\frac{\partial\left(H_{yz}+H_{yx}\right)}{\partial x}$$

$$\varepsilon\frac{\partial E_{zy}}{\partial t}+\sigma_y E_{zy}=-\frac{\partial\left(H_{xy}+H_{xz}\right)}{\partial y}$$

$$\mu\frac{\partial H_{xy}}{\partial t}+\sigma_y^* H_{xy}=-\frac{\partial\left(E_{zx}+E_{zy}\right)}{\partial y}$$

$$\mu\frac{\partial H_{xz}}{\partial t}+\sigma_z^* H_{xz}=\frac{\partial\left(E_{yz}+E_{yx}\right)}{\partial z}$$

$$\mu\frac{\partial H_{yz}}{\partial t}+\sigma_z^* H_{yz}=-\frac{\partial\left(E_{xy}+E_{xz}\right)}{\partial z}$$

$$\mu\frac{\partial H_{yx}}{\partial t}+\sigma_x^* H_{yx}=\frac{\partial\left(E_{zx}+E_{zy}\right)}{\partial x}$$

$$\mu\frac{\partial H_{zx}}{\partial t}+\sigma_x^* H_{zx}=-\frac{\partial\left(E_{yz}+E_{yx}\right)}{\partial x}$$

$$\mu\frac{\partial H_{zy}}{\partial t}+\sigma_y^* H_{zy}=\frac{\partial\left(E_{xy}+E_{xz}\right)}{\partial y}\quad . \qquad \text{(Eq. 3-9)}$$

Here the electric and magnetic conductivities are chosen to satisfy matching impedance condition [136]:

$$\frac{\sigma_\alpha}{\varepsilon_0} = \frac{\sigma_\alpha^*}{\mu_0} \text{ for } \alpha = x, y, z. \qquad \text{(Eq. 3-10)}$$

Note that for $\sigma_x = \sigma_y = \sigma_z$ and $\sigma_x^* = \sigma_y^* = \sigma_z^* = 0$ the set of 12 equations above yields the Maxwell equations. This signifies that all physical media such as vacuum, electrical conductor, etc. can be represented as particular cases of the absorbing medium [138]. Figure 3-23 shows upper-right part of a computational domain surrounded by the PML layer.

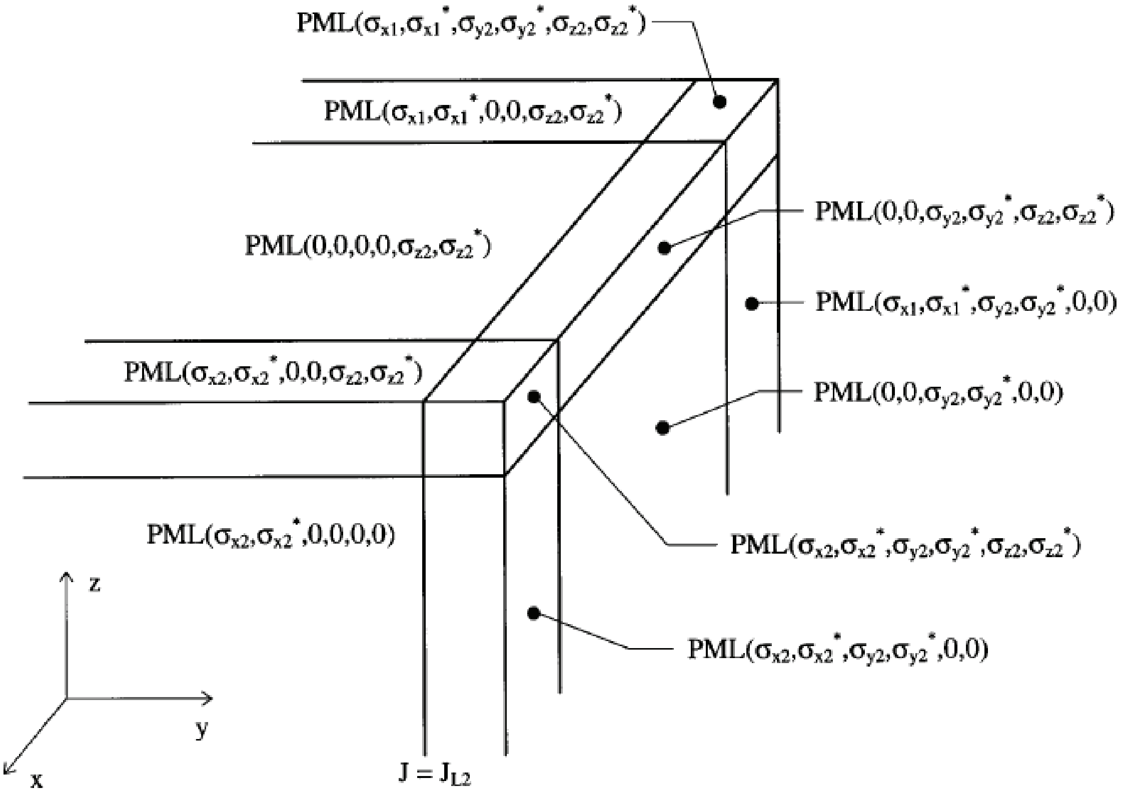

Figure 3-23. Upper-right part of a computational domain surrounded by the PML layer [139].

Theoretically, there is no reflection at the interface between the vacuum surrounding the scatterer and the absorbing layer. Some reflections result, however, from the perfectly conducting conditions on the outer boundary of the layer. This artificial reflection depends on the layer thickness δ and the conductivity profile $\sigma_\alpha(\rho)$. Reflection coefficient at an angle of incidence θ is given by

$$R(\theta) = [R(0)]^{\cos\theta} \qquad \text{(Eq. 3-11)}$$

where

$$R(0) = \exp\left(-\frac{2}{\varepsilon_0 c}\right)\int_0^\delta \sigma_\alpha(\rho)d\rho \qquad \text{(Eq. 3-12)}$$

Conductivity of a PML is varied from zero at the interface with the computational domain to a maximum value $\sigma_{\alpha,\max}$ at the outer egde of the layer:

$$\sigma_\alpha(\rho) = \sigma_{\alpha,\max}\left(\frac{\rho}{\delta}\right)^n \text{ for } \alpha = x, y, z. \qquad \text{(Eq. 3-13)}$$

The corresponding reflection coefficient is given by

$$R(0) = \exp\left(-\frac{2}{n+1}\right)\left(\frac{\sigma_{\alpha,\max}\delta}{\varepsilon_0 c}\right). \qquad \text{(Eq. 3-14)}$$

In early experiments *n*=1 and *n*=2 cases were considered [136]. *n*=2 is typically used, while *n*=4 is sometimes employed to reduce reflections further [128, 140, 141].

Because they use 12 field components in the PML region, the 3D FDTD algorithms using PML boundaries require very large computational resources. Most calculations performed for this project using the PML method concern very short (several microns long) portions of dielectric structures. In particular, FDTD with PML is used to assess reflections from abrupt dielectric interfaces where only a short length of the device on both sides of the interface is considered.

3.3.2 FDTD simulations of abrupt interfaces

While BPM is extremely efficient for modeling adiabatic transfer of optical power transfer between the modes of the ATG structure and those of passive waveguides, this method fails to account for reflections as it cannot handle backward-propagating power because of fundamental paraxial limitation. FDTD method with PML boundary conditions is used here to assess reflections at interfaces when there is an abrupt change in refractive index. Calculations were performed by Fuwan Gan.

FDTD calculations in three dimensions are very computationally demanding. Because computational resources and time available for such calculations are necessarily limited, computational domain has to be reduced to make simulations possible. A limited computational window is obtained by considering a short length of the device, several microns on each side of the interface.

To determine the limit of accuracy of our FDTD calculations before we proceed to evaluate reflections from abrupt interfaces using the same method, we computed backward-traveling optical power in a bulk ridge waveguide of 4 μm x 1.05 μm cross-section. The waveguide is composed of material with index n_{bulk}=3.22 on InP substrate. Theoretically, there should be no reflection in such waveguide, and calculated reflection is solely due to imperfections in numeric methods. FDTD simulations yield R=3.82x10^{-5} for propagation from passive waveguide towards the ATG. The source of the discrepancy is the boundary condition which can be improved at a cost of additional computational resources [139]. The above accuracy was judged to be sufficient because it allows to prove that reflections into the SOA from the tips of adiabatic tapers are on the order of 10^{-5}, adequately low for operating SOA as a single-pass device.

Next we look as a butt-coupled junction between two bulk waveguides of the same cross-section as above with bulk refractive indices of 3.22 and 3.42, respectively. The latter is the highest index of any material used in our ATG structure. Therefore, the calculated reflection should represent a limiting case. According to FDTD calculations, $R=7.28\text{x}10^{-4}$ for this junction. This value can be estimated by solving for the fundamental mode of the waveguides before and after the junction and substituting effective indices n_{eff1} and n_{eff2} into the following formula:

$$R = \frac{\left(n_{eff\,2} - n_{eff\,1}\right)^2}{\left(n_{eff\,2} + n_{eff\,1}\right)^2}. \qquad \text{(Eq. 3-15)}$$

In this case, $n_{\text{eff2}}=3.3566$, $n_{\text{eff1}}=3.1798$, and $R=7.31\text{x}10^{-4}$ in excellent agreement with the values obtained by FDTD simulation, even despite the fact that the higher-index section of the waveguide supports more than one mode.

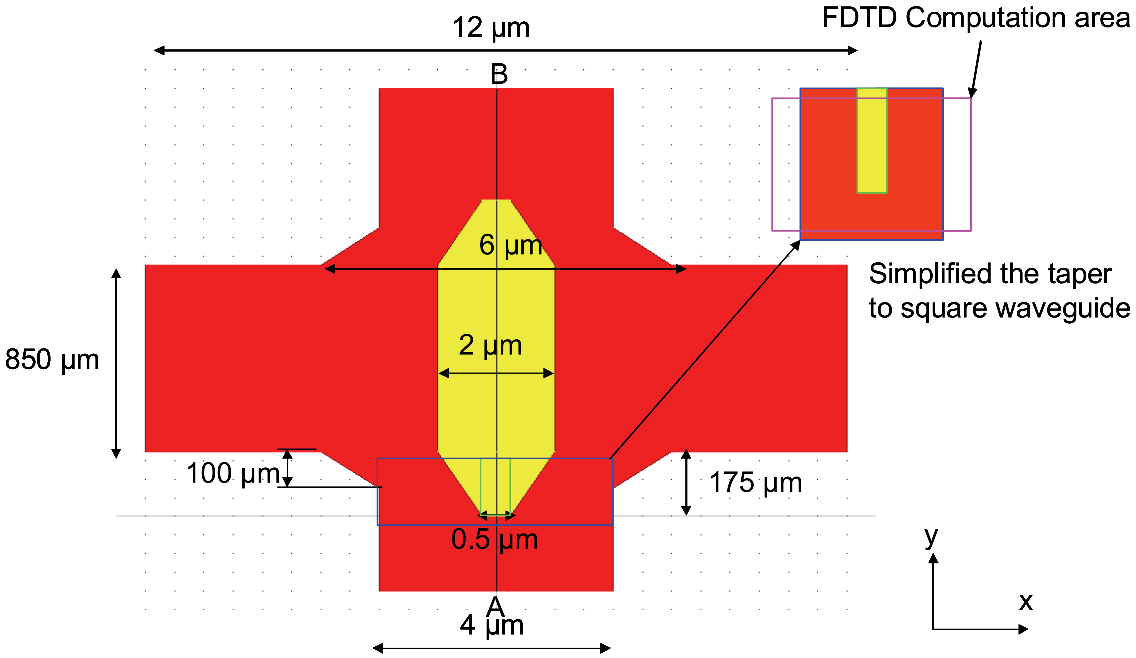

Figure 3-24. Simplification of taper tip for FDTD modeling.

Now we calculate the fraction of reflected energy at the tip of the adiabatic taper in the ATG structure presented earlier in this chapter. The very short initial portion of the taper is represented in FDTD model as having a constant width, as shown in Figure 3-24. This is largely accurate due to the finite step in mask writing. The simulation yields R=4.05x10^{-5} for a wave propagating from the passive waveguide toward the ATG, as illustrated in Figure 3-25, and R=3.68x10^{-5} for a wave propagating from the ATG toward the passive waveguide (Figure 3-26). In Figure 3-25, a wavefront is incident on the interface from the passive waveguide. The wave propagation along the specified direction is shown at three sequential time stamps. Figure 3-26 is similar to Figure 3-25, but the direction of propagation is reversed. The FDTD simulations yield a significantly higher reflection value than the estimate based on effective index. The effective index calculation yields R=3.38x10^{-8} (with n_{eff2}=3.1793, n_{eff1}=3.1805).

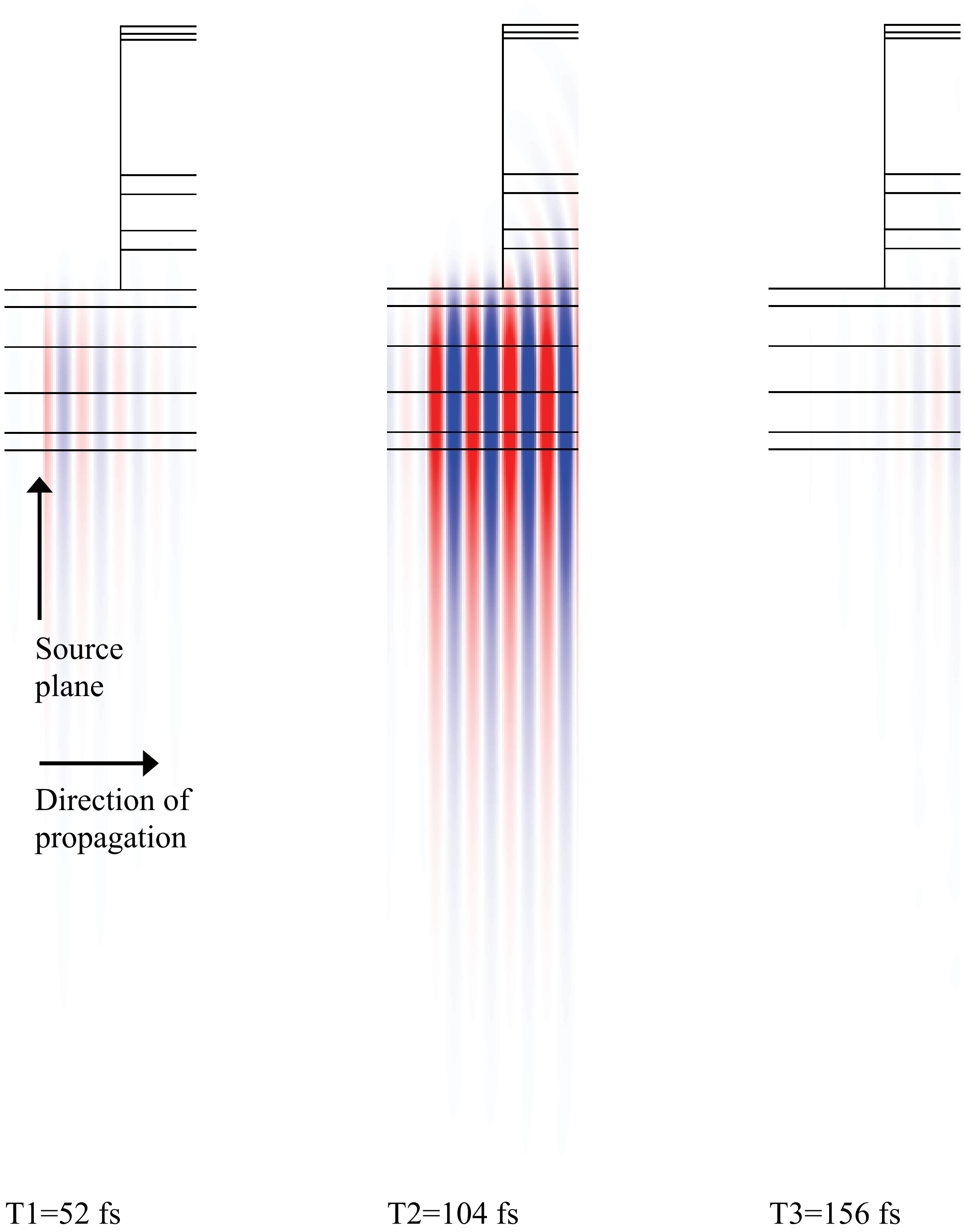

Figure 3-25. Optical power propagation by FDTD from passive waveguide to ATG.

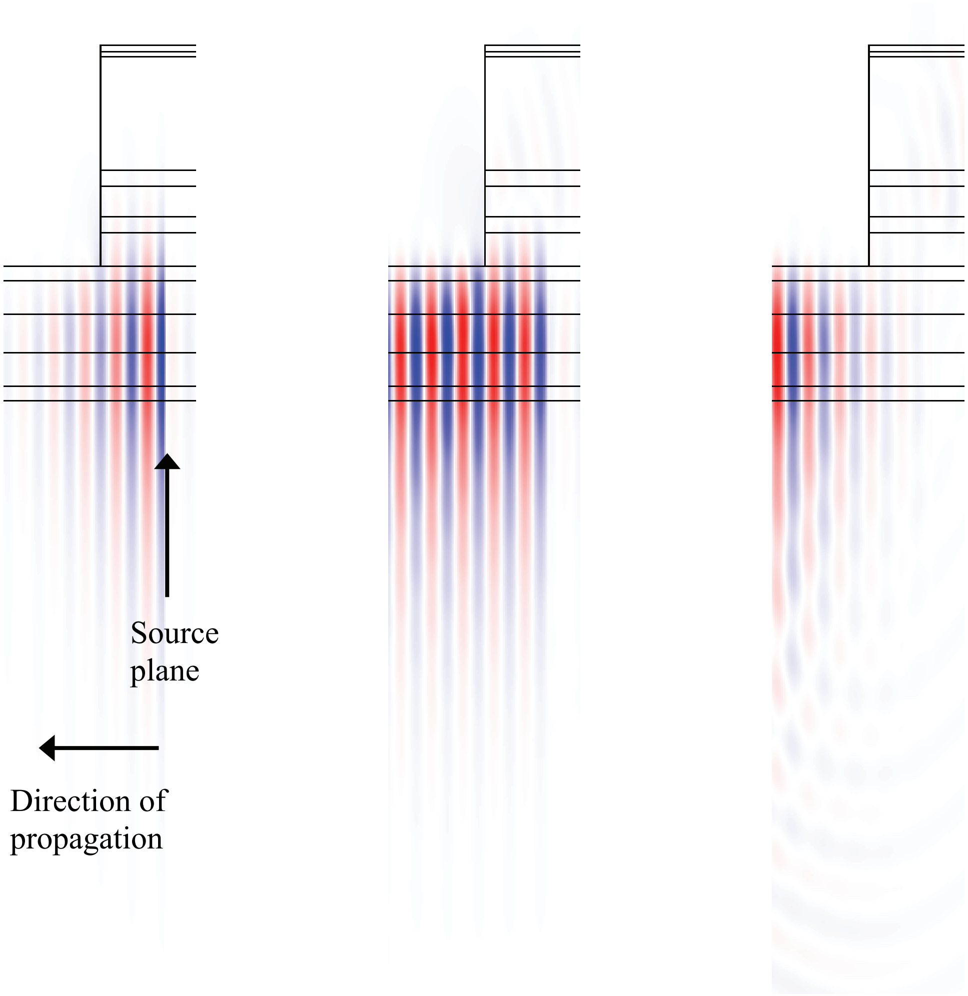

T1=52 fs T2=104 fs T3=156 fs

Figure 3-26. Optical power propagation by FDTD from ATG to passive waveguide.

Since reflection coefficient obtained by FDTD is on the order of the numeric error, the only reliable conclusion that can be drawn from the FDTD result in this case is that reflections from the taper tip are on the order of or lower, that is, sufficiently low for a successful operation of an SOA. Estimate based on effective index calculations suggests that R is well below the limit of FDTD accuracy in this case.

Comparison with FDTD results shows that calculating reflections based on local effective indices before and after the junction offers a simple, accurate, and time-efficient approach to estimating reflected optical power. This method is especially applicable to single-mode structures.

3.4 Overall loss in passive waveguides and couplers

In order to determine the amount of amplification required of the amplifiers in the circuit, it is necessary to estimate the total loss suffered by a signal passing through the optical logic unit cell. The overall loss has four sources: loss in passive ridge waveguides, bending loss in waveguide turns, coupling loss in taper couplers, and loss in MMIs.

Waveguide loss coefficient α can be estimated by considering the level of doping of passive waveguide layers. A typical loss coefficient is 3 $\text{cm}^{-1}/10^{18}\ \text{cm}^{-3}$ for n-doped materials. The passive layers in our semiconductor structure are doped at a level of $5\text{x}10^{17}\ \text{cm}^{-3}$. An optical signal passes through approximately 3.5 mm of passive waveguides as it propagates through the optical logic unit cell. Thus, the overall loss in passive waveguides is approximately 2.3 dB.

An optical signal passing through the unit cell negotiates three S-bends: one preceding and two following the Mach-Zehnder interferometer. Each S-bend consists of two 37.5° turns with a radius of curvature of approximately 300 μm. According to our simulations, each turn produces 0.65 dB of loss, for a total loss of 3.9 dB due to waveguide bends. Note that the curved waveguides also suffer from ordinary waveguide losses, thus, their length is included in the estimate within the previous paragraph.

As the signal is coupled from the passive waveguide into an SOA and back, it passes through two taper couplers. We have designed taper couplers with 96% efficiency, corresponding to a loss of 0.18 dB per taper. Total loss due to two taper couplers is 0.36 dB. As we have shown in Chapter 2, loss in MMIs of our design does not exceed 0.25 dB. The loss experienced by a signal passing through two MMIs is at most 0.5 dB.

If an SOA in the circuit is not biased with injected current, a signal passing through it will experience waveguide loss. The loss coefficient we used for the SOA simulations presented in the next chapter is 13.3 cm^{-1}. This figure is consistent with confinement factor $\Gamma=0.4$, with the remaining 0.6 fraction of optical energy distributed approximately equally between n-doped and p-doped layers. In the absence of bias current, loss in 0.85 mm long SOA is approximately 4.9 dB. However, this loss is accounted for by the SOA gain simulations. The loss in an unbiased SOA does not need to be included in the balance of loss which has to be compensated for by an SOA gain.

Let us consider additional losses which may arise from imperfections in processing described earlier in this work. In particular, severely underetched trench between MMI output waveguides may present up to 0.3 dB of additional loss. If efficiency of taper couplers is reduced from 96% to 90% due to the 0.5 μm width reduction of the upper taper, as described in Section 3.2.2.4, each taper coupler will introduce an additional 0.3 dB of loss. If both the underetching of trenches and the SOA ridge width reduction are present, these fabrication imperfections result in extra 1.2 dB loss.

To summarize, a signal passing through a perfectly fabricated all-optical logic unit cell experiences approximately 7.0 dB of loss due to losses in ridge waveguides, waveguide bends, adiabatic taper couplers and MMIs. Additional losses may arise from imperfections in fabrication. In the next chapter we will determine whether the amount of gain provided by nonlinear SOAs is sufficient to offset the 7.0 dB loss. If the gain is insufficient, the problem should be rectified by including additional linear amplifiers into the circuit.

96. Gaumont, E.G., C.; Gentner, J.L.; Pinquier, A.; Laube, G. *Butt coupling process for InP based photonic integrated circuits*. in *International Conference on Indium Phosphide and Related Materials*. 1996.

97. Pommereau, F.M., R.; Martin, B.; Rao, E.V.K.; Gaborit, F.; Leclerc, D.; Porcheron, C.; Renaud, M. *Optimisation of butt coupling between deep-ridge and buried ridge waveguides for the realisation of monolithically integrated wavelength selectors*. in *International Conference on Indium Phosphide and Related Materials*. 1999.

98. M. Renaud, D.K., N. Sahri, S. Silvestre, D. Prieto, F. Dorgeuille, F. Pommereau, J.Y. Emery, E. Grard, H.P. Mayer. *SOA-based optical network components*. in *Electronic Components and Technology Conference*. 2001.

99. J. Leuthold, et al., *Multimode interference couplers for the conversion and combining of zero- and first-order modes.* Journal of Lightwave Technology, 1998. **16**(7): p. 1228 –1239.

100. H.-G. Bach, W.S., G.G. Mekonnen, R. Steingruber, A. Seeger, W. Passenberg, W. Ebert, G. Jacumeit, Th. Eckhard, R. Ziegler, A. Beling, B. Schmauss, A. Munk, Th. Engel, A. Umbach. *50 GHz c for RZ and NRZ modulation format comprising InP-OEICs*. in *European Conference on Optical Communication*. 2001.

101. Xia, F., V.M. Menon, and S.R. Forrest, *Photonic integration using asymmetric twin-waveguide (ATG) technology: part I-concepts and theory.* Selected Topics in Quantum Electronics, IEEE Journal of, 2005. **11**(1): p. 17-29.

102. L.M. Lam, C.W.K., H.P. Ho, E.Y.B. Pun, K.S. Chan, Z.N. Fan, P.K. Chu, *Plasma immersion Ar+ ion implantation induced disorder in strained InGaAsP multiple quantum wells.* Electronics Letters, 1998. **34**(8): p. 817-818.

103. D. Hofstetter, H.P.Z., J.E. Epler, *Ridge waveguide DBR laser with nonabsorbing grating and transparent integrated waveguide.* Electronics Letters, 1995. **31**(12): p. 980-982.

104. Hutchings, D.C., *Determination of nonresonant optical nonlinearities in undisordered and disordered semiconductor superlattices* in *Quantum Electronics and Laser Science Conference*. 1999. p. 207 -208.

105. Marsh, J.H. *InP-based monolithic integrated circuits based on quantum well intermixing technology*. in *Lasers and Electro-Optics Society*. 2001

106. A. McKee, C.J.M., G. Lullo, A.C. Bryce, R.M. De La Rue, J.H. Marsh, C.C. Button, *Monolithic integration in InGaAs-InGaAsP multiple-quantum-well structures using laser intermixing.* IEEE Journal of Quantum Electronics 1997. **33**(1): p. 45-55.

107. H.S. Lim, B.S.O., Y.L. Lam, Y.C. Chan, V. Aimez, J. Beauvais, J. Beerens. *Photonic integration of InGaAs/InGaAsP laser using low energy arsenic implantation induced disordering for quantum well intermixing*. in *The Pacific Rim Conference on Lasers and Electro-Optics*. 1999.

108. S.L. Ng, H.S.D., H.S. Lim, B.S. Ooi, Y.L. Lam, Y.C. Chan, P. Dowd, V. Aimez, J. Beauvais, J. Beerens. *Polarisation-dependent performance of multiple wavelength electro-absorption intensity modulator arrays on a single InGaAs/InGaAsP chip*. in *IEEE Lasers and Electro-Optics Society*. 2001.

109. Thornton, R.L. *Impurity induced layer disordering and its importance in optoelectronic device fabrication* in *Lasers and Electro-Optics Society* 1994.

110. T.K. Sudoh, M.K., Y. Nakano, K. Tada, *Wavelength trimming by photoabsorption-included disordering for multiple-wavelength distributed-feedback laser arrays.* IEEE Photonics Technology Letters 1997. **9**(7): p. 887-888.

111. Hee Taek Yi, et al. *Effect of dielectric-semiconductor capping layer combination on the dielectric cap quantum well disordering of InGaAs/InGaAsP quantum well structure*. in *The Pacific Rim Conference on Lasers and Electro-Optics*. 1999.

112. Cheolhwan Kim; May-Arrioga, D.L., P.; Newman, P.; Pamulapati, J. . *Monolithically integrated ultrafast all-optical demultiplexer switch* in *Lasers and Electro-Optics Society* 2000.

113. D. Hofstetter, H.P.Z., J.E. Epler, P. Riel, *Monolithically integrated DBR laser, detector, and transparent waveguide fabricated in a single growth step.* IEEE Photonics Technology Letters, 1995. **7**(9): p. 1022-1024.

114. S.A. Bradshaw, J.H.M., R.W. Glew, *Extended cavity lasers formed by fluorine induced quantum well disordering.* IEE Colloquium on Applications of Quantum Well Technologies, 1993: p. 7/1-7/4.

115. Shimada, N.F., Y.; Uemukai, H.; Suhara, T.; Nishihara, H.; Larsson, A., *Monolithic integration of laser and passive elements using selective QW disordering by RTA with SiO2 caps of different thicknesses.* IEEE Journal on Selected Topics in Quantum Electronics, 2001. **7**(2): p. 350 - 354.

116. Shimada, N.F., Y.; Uemukai, M.; Suhara, T.; Nishihara, H.; Larsson, A.;. *Selective disordering of InGaAs strained quantum well by rapid thermal annealing with SiO2 caps of different thicknesses for photonic integration*. in *Semiconductor Laser Conference*. 2000.

117. Khurgin, J.B., et al., *Reduced crosstalk semiconductor optical amplifiers based on Type-II quantum wells.* Photonics Technology Letters, IEEE, 2002. **14**(3): p. 278-280.

118. Ribot, H., P. Sansonetti, and A. Carenco, *Improved design for the monolithic integration of a laser and an optical waveguide coupled by an evanescent field.* Quantum Electronics, IEEE Journal of, 1990. **26**(11): p. 1930-1941.

119. P.V. Studenkov, M.R.G., S.R. Forrest, *Efficient coupling in integrated twin-waveguide lasers using waveguide tapers.* IEEE Photonics Technology Letters, 1999. **11**(9): p. 1096-1098.

120. P.V. Studenkov, M.R.G., J.C. Dries, S.R. Forrest, *Monolithic integration of a quantum-well laser and an optical amplifier using an asymmetric twin-waveguide structure.* IEEE Photonics Technology Letters, 1998. **10**(8): p. 1088-1090.

121. P.V. Studenkov, F.X., M. Gokhale, and S. Forrest, *Assymmetric twin-waveguide 1.55um wavelength laser with a distributed bragg reflector.* IEEE Photonics Technology Letters, 2000. **12**(5): p. 468.

122. Forrest, S.R., et al. *Integrated photonics using asymmetric twin-waveguide structures*. in *International Conference on Indium Phosphide and Related Materials*. 2000.

123. Vusirikala, V., et al., *1.55-μm InGaAsP-InP laser arrays with integrated-mode expanders fabricated using a single epitaxial growth.* Selected Topics in Quantum Electronics, IEEE Journal of, 1997. **3**(6): p. 1332-1343.

124. S. Saini, J. Michel, and L.C. Kimerling, *Index Contrast Scaling for Optical Amplifiers.* Journal of Lightwave Technology, 2003. **21**(10): p. 2368-2376.

125. F. Xia, J.T., M. Gokhale, P. Studenkov, J. Wei, W Lin and S. Forrest, *An assymmetric twin –waveguide high bandwidth photodiode using a lateral taper coupler.* IEEE Photonics Technology Letters, 2001. **13**(8): p. 845.

126. P. Studenkov, M.G., J. Wei, W Lin, I Glesk, P. Prucnal and S. , *Monolithic integration of an all optical mach-zehnder demultiplexer using an asymmetric twin-waveguide structure.* IEEE Photonics Technology Letters, 2001. **13**(6): p. 600.

127. P.V. Studenkov, M.R.G., J. Wei, W.C. Lin, I. Glesk, P.R. Prucnal, S.R. Forrest. *Integrated, asymmetric twin-waveguide ultrafast all-optical switch*. in *Lasers and Electro-Optics Society*. 2000.

128. C. Manolatou, et al., *Coupling of modes analysis of resonant channel add-drop filters* Quantum Electronics, IEEE Journal of, 1999. **35**(9): p. 1322 –1331.

129. Kawanishi, H., K. Kishino, and Y. Suematsu, *AlGaAs integrated twin-guide lasers with distributed Bragg reflectors.* Quantum Electronics, IEEE Journal of, 1977. **13**(9): p. 818-818.

130. Suematsu, Y., M. Yamada, and K. Hayashi, *Integrated twin-guide AlGaAs laser with multiheterostructure.* Quantum Electronics, IEEE Journal of, 1975. **11**(7): p. 457-460.

131. Studenkov, P., *Photonic Integration Using Asymmetric Twin-Waveguides*, in *Department of Electrical Engineering*. 2001, Princeton University.

132. Menon, V.M., *Personal communication*. 2005: City University of New York.

133. B.E. Little, et al., *Microring resonator arrays for VLSI photonics.* IEEE Photonics Technology Letters 2000. **12**(3): p. 323 -325.

134. Jurgens, T.G., et al., *Finite-difference time-domain modeling of curved surfaces [EM scattering].* Antennas and Propagation, IEEE Transactions on, 1992. **40**(4): p. 357-366.

135. Taflove, A., *Computational electrodynamics : the finite-difference time-domain method*. Artech House antennas and propagation library. 2000, Boston: Artech House.

136. J.-P. Berenger, *Perfectly matched layer for the FDTD solution of wave-structure interaction problems.* IEEE Transactions on Antennas and Propagation, 1996. **44**(1): p. 110-117.

137. Berenger, J.-P., *A perfectly matched layer for the absorption of electromagnetic waves.* Journal of Computational Physics, 1994. **114**: p. 185–200

138. Berenger, J.-P., *Three-dimensional perfectly matched layer for the absorption of electromagnetic waves.* Journal of Computational Physics, 1996. **127**(2): p. 363-379.

139. M.H. Shih, et al., *Alignment-relaxed 1.55 um multiquantum well lasers fabricated using standard buried heterostructure laser processes.* Electronics Letters, 1995. **31**(13): p. 1058-1060.

140. Yu, C.-P. and H.-C. Chang, *Yee-mesh-based finite difference eigenmode solver with PML absorbing boundary conditions for optical waveguides and photonic crystal fibers.* Optics Express, 2004. **12**(25): p. 6165-6177.

141. Berenger, J.-P., *A perfectly matched layer for free-space simulation in finite-difference computer codes.* Annales des Telecommunications, 1996. **51**(1-2): p. 39-46.

4 Semiconductor Optical Amplifier

In this chapter, we begin by stating the basic physical principles of SOA operation. Next we list the range of SOA applications in photonic integrated circuits as linear amplifiers and non-linear components. We compare the SOA with an Erbium-doped fiber amplifier (EDFA) in order to gain insight into desirable characteristics of linear optical amplifiers. We briefly review methods for overcoming gain compression in SOAs used as linear amplifiers. Next we discuss use of SOAs for all-optical signal processing, addressing techniques for reducing pattern-dependent behavior.

In the later part of this chapter we present a simple numerical model of pulse propagation in the SOA that allows us to assess gain and nonlinear phase for a wide range of signal wavelengths and energies. We use the model to calculate the dependence of small signal gain (SSG), output saturation power, nonlinear phase, and amplified spontaneous emission (ASE) power on SOA parameters such as SOA length and injection current density. Finally, based on simulation results we draw several conclusions about design of SOAs for linear and non-linear operation.

4.1 Physical principles behind semiconductor optical amplifier operation

When light of frequency ω is incident on a semiconductor of bandgap energy E_g, photons can interact with carriers through interband transition, provided that $\omega > \frac{E_g}{\hbar}$. A photon with energy slightly greater than E_g is absorbed by an electron transition between the valence and conduction bands. Since there is only a limited number of states that can participate in the transition, a sufficiently intense light beam can saturate the absorption. When the passive semiconductor is replaced by a semiconductor optical amplifier, a bias current drives the electrons into the conduction band, inverting the free carrier population. The incident beam is amplified because additional photons are produced by stimulated electron-hole recombination. Net optical gain occurs when stimulated emission is more prevalent than absorption. The amplification can also be saturated since only a limited number of states can participate in transitions that give rise to optical gain. Thus, the principle behind SOA operation can be described as a band-filling nonlinearity, the creation of a population inversion that causes stimulated emission to be more prevalent than absorption [142]. In other words, interband nonlinearities (those related to carrier transitions between valence and conduction band) govern saturation of gain and absorption [143]. After the SOA gain is saturated by an optical pulse, gain recovers by carrier injection on the scale of 1 ns. For optical pulses much shorter than a nanosecond, intraband dynamics become important. Intraband phenomena refer to those causing carrier redistribution within the same band [144].

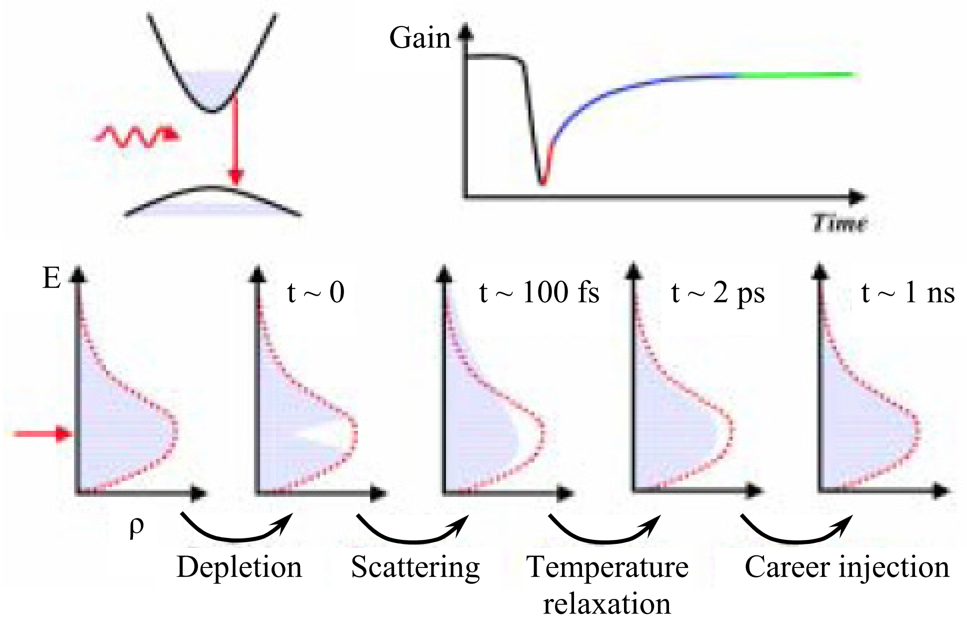

Figure 4-1. Carrier and gain dynamics [145].

After a short pulse is injected into an SOA and stimulated emission occurs, carrier distribution recovers to equilibrium by means of four major physical mechanisms. Each of these mechanisms dominates on a particular time scale [144, 146, 147] (Figure 4-1). Stimulated emission causes recombination of carriers in the narrow range of energies around the photon energy of the optical pulse. This reduction in carrier density is referred to as spectral hole burning and can be considered instantaneous. Carrier-carrier scattering restores the Fermi-Dirac distribution of the carriers within hundreds of femtoseconds after the pulse leaves the SOA. The overall number of carriers is smaller than before the arrival of the optical pulse because the carriers are depleted by stimulated emission. In addition, average carrier temperature is increased since lower-energy carriers are the ones removed. Establishment of a Fermi-Dirac distribution at a higher temperature and lower carrier density than that of the band is called carrier heating. Next the distribution relaxes to the lattice temperature due to phonon interactions. The time constant associated with this process is called temperature relaxation time and is on the order of a few picoseconds. Eventually the original carrier distribution is restored by carrier injection on approximately a nanosecond time scale. Figure 4-1 illustrates carrier distribution evolution in an SOA active region [145].

A typical SOA represents an active ridge waveguide in which carrier confinement and optical guiding is achieved in a double heterojunction. Design of the SOA heterostructure deals with the same issues as a typical semiconductor laser design. One of the main advantages of a double heterostructure design for an SOA is that the thickness of an active layer can be dramatically reduced. A smaller active region thickness allows an amplifier to demonstrate a substantial gain even at very low injected current densities. The doping profile is chosen to confine carriers to the active region, which is much shorter than the carriers' diffusion length. In addition, the active layer is designed to have a larger index of refraction than that of the cladding layers, causing confinement of light to an active region of smaller thickness than the wavelength of light [142]. While the high-index layers provide vertical confinement, the etched ridge provides horizontal optical confinement.

A semiconductor laser needs a cavity confined between highly reflective facets in order to provide positive feedback to the system. To operate an SOA as a broadband single-pass device, the SOA must have very low facet reflectivity to avoid the creation of resonator modes, especially if SOA provides high gain. Cavity resonance causes gain ripple, reduced carrier density, reduced gain bandwidth, lower output saturation power, and higher noise figure. One approach to combating reflections is anti-reflection coating (ARC) of the facets. Reflectivity as low as 10^{-3} has been reported using ARC [148]. TiO_2/SiO_2 layers are typically used for anti-reflection coating [149, 150]. Another popular method is tilting the active WG to have light reflect away from the active region. Low reflectivity of $<10^{-5}$ has been reported in the literature for the angled waveguide design [142]. Yet another method involves the use of a window region when the waveguide is terminated before the facet causing the optical mode to expand so that less optical power is reflected back into the active region. Usually some combination of the above methods is used to achieve sufficiently low reflectivity of the SOA facets [144, 151, 152].

When SOAs are employed in all-optical switching schemes, the data signal is usually weak enough to produce little effect on the carrier dynamics while the control signal is typically intense enough to alter the carrier density. The signal experiences conditions created by the control pulse. For pulses of wavelength close to that corresponding to SOA bandgap, the change in refractive index varies approximately linearly with the change in carrier density [143]. In other words, the refractive index is intensity-dependent or non-linear. Phase change of the signal pulse is affected by the altered refractive index. If the signal pulse has a wavelength higher than λ_g the active material, it will not be absorbed or amplified by the active material, but will still be affected by the refractive index changes induced by the control pulse.

An SOA can be biased to operate in three regimes: absorption, transparency, and gain. When an SOA is biased in the absorption regime (little or no current to the device), an intense control pulse is absorbed, resulting in an increase of carrier density in the conduction band. The data signal then sees a decrease in the index of refraction and experiences amplification due to stimulated emission. If an SOA is biased in the gain regime (large external current), an intense control signal causes stimulated emission and depletes the carrier density in the conduction region [153]. The data signal then experiences a larger refractive index due to a decreased population inversion. For an SOA biased in the transparency regime (just enough current to balance the carrier density in the conduction band and the valence band), the control signal has little effect on the carrier density, and the data pulse does not experience a change in index or intensity. In an all-optical network, SOAs can be used for amplification of signals, introducing a phase shift, or for switching applications [153]. For amplification, an SOA needs to be biased in the regime where the gain is approximately linear, while switching schemes employ nonlinear behavior of the SOAs [154-156].

4.2 Applications of semiconductor optical amplifiers in photonic integrated circuits

SOAs boast many of the same attractive features as widely used semiconductor lasers: small size, simple electrical pumping, broad spectral range, integrability into photonic circuits and potential for mass production. In SOAs, the choice of gain peak wavelength is determined by the selection of active material. SOA-based devices can be designed to achieve low optical and electrical power consumption, high speed, and low polarization dependence.

SOAs are employed in photonic integrated circuits both for linear amplification and nonlinear operation. Strong nonlinearities and fast gain dynamics make SOAs useful for all-optical signal processing applications [147]. The same characteristics cause difficulties when the SOA is operated as a linear amplifier [145]. Examples of linear applications are power boosters following an optical source, repeaters, and pre-amplifier before a photodetector. Non-linear applications include all-optical wavelength conversion, all-optical switching, wavelength selection, and regeneration including reamplification, dispersion compensation and clock recovery [149, 157].

4.3 Semiconductor Optical Amplifiers for Linear Amplification

4.3.1 Comparison of semiconductor optical amplifier and Erbium-doped fiber amplifier

Although the first SOA was demonstrated as early as 1964 [158], it was not until the mid-1990s that SOAs with low polarization sensitivity, high gain, and high saturation power were achieved [159]. When the Erbium-doped fiber amplifier (EDFA) was invented in 1987 [160], EDFA began competing with the SOA as an in-line amplifier. Currently, the EDFA sets a standard for linear amplification performance in optical communication systems. It is useful to examine what makes EDFA a linear amplifier of choice, to compare EDFA to SOA and determine what desirable linear amplifier characteristics can be achieved in a carefully designed SOA.

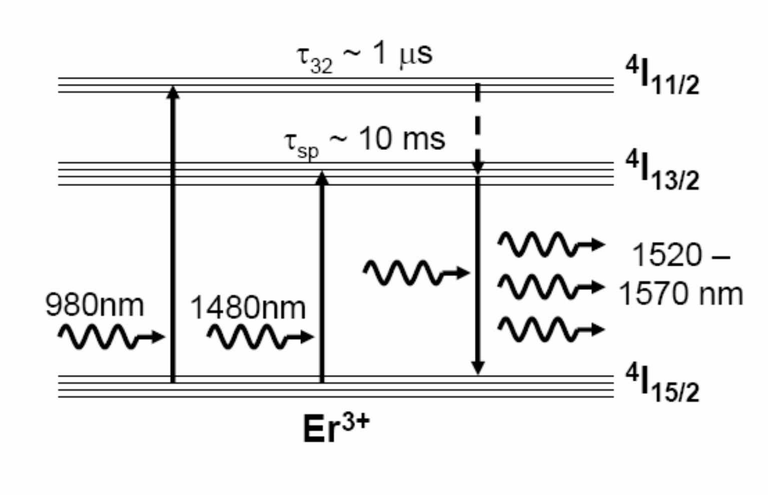

Figure 4-2. Erbium-Doped fiber amplifier [151].

The erbium-doped fiber amplifier is the most commonly used of rare-earth-doped silica fiber amplifiers. The position of gain peak depends on the dopant. EDFA amplifies 1.55 μm signals when pumped with a 980 nm or 1480 nm light source which excite Erbium ions to the second and first excited states, respectively. Light with wavelength between 1.52-1.57 μm experiences amplification by inducing stimulated emission in the Erbium ions (Figure 4-2). The EDFA is somewhat cumbersome as the basic setup includes pump laser, optical isolators, and wavelength-selective couplers in addition to the fiber itself. A typical fiber is 20 m long and provides about 25 dB of amplification. Because the EDFA can be efficiently inverted, the noise figure can be close to the theoretical limit for optical amplifiers of 3 dB. Due to the symmetry of the fiber core, gain in EDFA is virtually polarization-independent [151].

Carrier population recovery time in EDFA is on the order of 10^{-3} s. Very slow gain dynamics makes EDFAs excellent linear amplifiers by ensuring low cross-talk. Advantages of EDFA include easy, low-loss coupling to fibers, polarization insensitivity, virtual absence of cavity effects, and high output saturation power. The main disadvantages of EDFA are the need for optical pumping and large length. In addition, EDFA does not yield itself to monolithic integration.

Compared to the EDFA, the SOA features strong nonlinearity and fast gain dynamics. These characteristics make SOA inferior to EDFA for linear operation (as pre-amplifiers, boosters, in-line amplifiers). Because bit-period in a typical optical communication system is comparable with SOA carrier recovery time, pulses passing through an SOA suffer from distortion and cross-talk when the SOA device is operated under saturation. The SOA also has a higher noise figure than EDFA due to amplified spontaneous emission, usually around 6-8 dB [161, 162]. Currently the SOA cannot compete with EDFA in applications for long-haul transmission where superior linear amplifier performance is required. Nevertheless, SOAs do have important advantages that insure their place as linear amplifiers in PICs: they are much more compact, cheap, and integrable. In PICs high-performance linear amplifiers are typically not necessary. SOAs can be successfully employed as pre-amps and boosters in PIC with moderate gain requirements.

4.3.2 Materials with long carrier lifetime

One approach to designing SOAs with EDFA-like characteristics is to use semiconductor materials and structures with a long carrier lifetime [163]. In indirect-bandgap materials electrons and holes are separated either in real space or in momentum space. Consequently, carrier lifetime is increased by several orders of magnitude. When the carrier lifetime is increased to the microsecond scale, intersymbol interference is drastically reduced. The effects of ASE are also significantly decreased. Among indirect-bandgap SOA materials are quasi-indirect bandgap superlattice materials [164, 165] and Type II (staggered-alignment) delta-doped materials [163]. Khurgin et al. [166] propose an SOA based on a three-constituent AlGaInAs–AlGaAsSb–AlInAs (all lattice-matched to InP) type-II multiple quantum-well (QW) active region with reduced differential gain and enhanced carrier lifetime. In indirect-bandgap materials carrier lifetime as high as ~4 ms has been reported [163]. Such materials are used to realize SOA designs with dynamic response similar to that of an EDFA.

4.3.3 Gain-clamped semiconductor optical amplifiers (GC-SOA)

Gain clamping is used to reduce cross-talk and intersymbol interference. Distributed Bragg Reflectors (DBRs) are incorporated into the facets of the SOA to create wavelength-selective feedback in the cavity. The wavelength for lasing is chosen to lie outside the intended amplifier bandwidth. Laser wavelength of 1510 nm is usually used for SOAs whose bandwidth lies in the C-band (1530-1560 nm). In a GC-SOA carrier density saturates quickly due to lasing. Consequently, GC-SOA displays constant gain for a large range of output power. Lasing removes gain compression and turns off when laser energy is consumed. While gain is stabilized at a lower level compared to a standard SOA, the saturation power is increased [149, 151].

GenOA Corporation developed an SOA monolithically-integrated with a VCSEL. The gain of the amplifier is saturated when SOA is flooded with light from the VCSEL. The signals pass along the SOA while the laser light is directed vertically. GenOA's devices are claimed to be small, inexpensive, have low power requirements, and cover the full C-band [167].

4.3.4 Non-uniform current injection

Improved linear operation of an SOA can be obtained by setting up non-uniform carrier distribution along the length of the device. In particular, exponentially increased carrier distribution can be implemented by means of non-uniform current injection into the SOA. Lin et al. [168, 169] demonstrated an SOA gain profile with an increased saturation power by fabricating multiple electrodes and applying a nearly exponentially-increasing current to different electrodes along the SOA waveguide. Other researchers were able to obtain similar injection current profile by using a special etching pattern for the metal and p-conducting material [170]. An exponentially-increasing current injection profile was proven to reduce crosstalk and provide improved gain linearity at the same overall injection current level.

4.4 Semiconductor Optical Amplifiers for All-Optical Signal Processing

4.4.1 All-optical signal processing schemes

All-optical signal processing schemes using SOAs rely on cross-gain modulation (XGM), cross-phase modulation (XPM), or four-wave mixing (FWM). In XGM, changes in gain caused by the control pulse are experienced by the signal pulse. In XPM, changes in phase due to the control pulse affect the signal pulse. FWM occurs when three wavelengths interact in a nonlinear medium to give rise to a fourth wavelength. In XGM, a weak probe signal is modulated when the probe experiences reduced gain due to a high pump signal. Because XGM devices rely on maximizing carrier modulation, they suffer from significant chirp due to the fact that gain modulation is generally accompanied by phase modulation. In addition, XGM devices, such as wavelength converters, have little or no regenerative capability and often suffer from extinction ratio degradation—the facts that limits device cascadability. XPM systems can be used in order to avoid described problems. To exploit XPM, SOAs are inserted into the arms of an interferometer. The pump signal depletes the carrier density and modulates the refractive index experienced by the probe. The highly nonlinear XPM scheme is capable of reshaping the incoming data, improving of the extinction ratio, and redistribution of the noise on the input signal [171].

Carrier lifetime determines the duration of the trailing edge at the output. At high repetition rates, the trailing edge of a signal interferes with the time-slot of the subsequent bit and, as a consequence, pattern dependence is observed. The initial change in carrier density and gain in response to the first pulse is large, but for a pulse train the gain reduction is periodic as the gain recovers to approximately the same magnitude between adjacent pulses for a train of 1's. Differential-mode operation is used in order to utilize the fast response and avoid the effects of slow recovery. In differential mode, delayed attenuated signal pulse is copied to the second arm of a balanced interferometer. The phase difference between the signals in the upper and the lower arms of the interferometer is governed by the slope of the phase response rather than the absolute phase shift. The switching window is thus narrowed, masking the finite gain and phase recovery times of the individual SOAs. The energy of a signal pulse has to be chosen carefully in order to avoid driving the SOA toward transparency at high bit rates when a long string of "ones" is encountered. When net material gain reaches zero, no further change in gain or phase occurs. The differential scheme breaks down at high bit rates because the slope of the phase change decreases with each bit in a long string of 1's as the carriers are depleted [145, 154].

Below we discuss two approaches with a potential for overcoming pattern dependence in all-optical circuits employing SOAs.

4.4.2 Quantum Dot Semiconductor Optical Amplifiers

Quantum dot SOAs (QD-SOA) were recently proposed as a solution to undesirable patterning effects. An active region of a QD-SOA includes a number of quantum dot layers. The preferred method of fabrication of quantum dots is by self-assembly. In Stranski-Krastanov growth technique quantum dots assemble on top of a thin wetting layer (WL). Self-assembled InAs quantum dots on a GaAs substrate usually have a shape of a pyramid with a base of 10-15 nm and a height of 5-10 nm. Quantum dots self-organize due to a large lattice-mismatch between the substrate and the epilayer causing a significant strain in the epilayer. Quantum dots are produced as a structure with a minimum of free energy is established during growth. The WL thickness is typically below a nanometer [172]. The properties of the wetting layer are important for the device performance because WL acts as a reservoir of carriers for the quantum dot states (Figure 4-3). Carries from the WL are captured into the QD excited states by phonon-assisted and Auger-assisted processes. Relaxation from excited states to QD ground states occurs through similar mechanisms. Complete population inversion is much easer to obtain in a QD-SOA than in a bulk SOA where reservoir states are strongly coupled with optically active states. The discrete QD energy levels together with the wetting layer form what can be described as a three-level system similar to that of EDFA.

It is therefore reasonable to expect some of the desirable EDFA characteristics such as low noise figure and absence of pattern effects to be achievable with QD-SOAs.

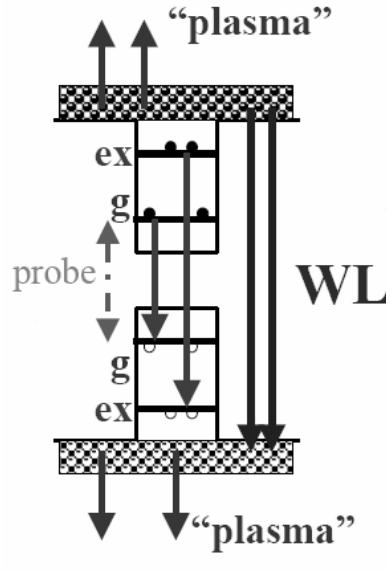

Figure 4-3. Quantum Dot SOA [172] (g is the ground state; ex is the excited state).

For high pumps, saturation is suppressed and QD-SOA displays excellent linear amplification properties. QD-SOA exhibit low modal gain due to small cross-sections of carrier-photon interaction (confinement factor). This, in turn, results in the need for long devices. High saturation power is achieved due to small confinement factor and the fact that WL acts as a highly filled reservoir of carriers separated from the ground state by significant energy. High saturation power in turn means that high levels of device gain are achievable for large device lengths. As with an EDFA, a large degree of population inversion ensures a noise figure close to the fundamental quantum limit of 3 dB.

QD-SOAs also display superior nonlinear properties owing to fast gain recovery due to the carrier reservoir in the upper states. Before light enters the device, ground state and excited state of QD as well as WL states are nearly completely inverted. After a light pulse enters the SOA, ground state is quickly depleted by stimulated emission, but recovers rapidly (on the scale of 150 fs) due to fast relaxation of electrons from excited state to ground state. The excited state is refilled by electrons from the wetting layer on a time scale of several picoseconds. Finally, the wetting layer carrier population recovers by injected current. If the bias current is high enough so that the saturated WL carrier density is large, the QD states remain inverted and pattern-free operation becomes possible [145].

Pattern-effect-free (PEF) amplification requires constant gain which can be achieved in a QD-SOA at sufficiently high pump current densities. Imagine that the most dense bit train (a train of 1s) is passing through an SOA. The minimum in carrier concentration N_{min} occurs after a 1 pulse. The population subsequently recovers to the level N_{max} before the next pulse. If N_c is the critical carrier density at which the modal gain reaches its maximum (that is, complete inversion is achieved), $N_{min}, N_{max}>N_c$ represents the condition for pattern-free operation [172].

When XPM schemes are used, pattern-free operation is achieved when two conditions are met. The first one is the same as for PEF amplification: constant gain at large pump currents due to complete inversion of working QD levels, as described above. The second one is constant differential refractive index $\frac{dn}{dN}$ as a function of carrier density. For QD active material, refractive index dependence on carrier density can be written as

$$n(N) = n_{QD}(N) + n_{WL}(N) + n_{plasma}(N). \qquad \text{(Eq. 4-1)}$$

That is, it includes contributions from the quantum dots, wetting layer, and plasma effect. The latter is given by Drude formula:

$$n_{plasma} = -\frac{q^2 N}{2 n_g \varepsilon_0 m_r \omega^2}, \qquad \text{(Eq. 4-2)}$$

where m_r is the reduced mass of the carriers and ω is the probe (small signal) frequency. Since refractive index due to plasma effect is linearly-dependent on carrier density, its contribution to the differential refractive index is constant. At large N differential refractive index is dominated by "plasma effects" due to complete population of quantum dot levels and therefore is also approximately constant [172].

Uskov et al. [173-175] argue that quantum dot active regions are superior to quantum well and bulk active regions because in QD-SOAs it is easier to achieve maximum gain and maximum gain is lower. Mork et al. [145] speculate that distinctive dynamical features of QD-SOAs will make them the linear amplifier of choice. In March 2005, Fujitsu Laboratories Ltd. reported QD-SOA which accomplishes both re-amplification and re-shaping of optical signals. This is the first semiconductor device that can carry out both functions required in order to eliminate waveform degradation and reduce noise. Fujitsu reports a 40% reduction in the noise-to-signal ratio when their QD-SOA was biased to produce 15 dB gain [176].

4.4.3 Use of keying to overcome pattern dependence

Intelligent use of balanced data keying schemes can be used to overcome pattern-dependent power fluctuations in PICs that employ SOAs. Standard return-to-zero ON-OFF keying (RZ-OOK) represents a "one" by a presence of an optical signal and "zero" by an absence of a signal. Such encoding is clearly unbalanced as the power level in optical devices depends directly on the number and sequential order of "ones" and "zeros" in the data stream. In SOA-based interferometric switches the SOAs are operated in saturation. At high data rates, both the phase and the gain in an SOA experience pattern-dependent modulation. In particular, carrier density is greatly depleted by a long string of "ones". Similarly, carrier population in an SOA will have a chance to recover more completely during a long sequence of "zeros" than it would during a short one. This leads to significant bit-to-bit intensity variation and poor extinction ratio. The problem can be remedied if constant-intensity encoding scheme is utilized [177].

Fortunately, similar data processing issues have been previously addressed in electrical domain. Electrical communication theory offers a number of possible solutions in a form of various bit balancing schemes. For example, 8B/10B encoding was patented by IBM. It uses a specific 10-bit sequence to represent every possible bit octet. Every such 10-bit data group contains either five "ones" and five "zeros", six "ones" and four "zeros", or four "ones" and six "zeros", ensuring a minimum number of consecutive "ones" and "zeroes". Such scheme can be directly applied to optical communication. One of the disadvantages of 8B/10B encoding is the necessary reduction in data rate [178].

Two encoding schemes popular in the electrical domain are Coded Mark Inversion (CMI) and Manchester Encoding [179] (Figure 4-4). Both ensure that energy level fluctuations in the circuit are limited regardless of data pattern. These two bit balancing schemes were recently adapted to optical domain.

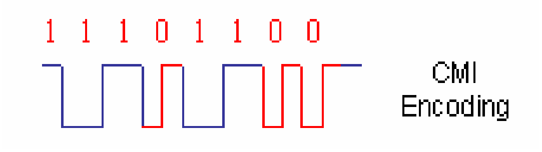

Coded Mark Inversion (CMI)

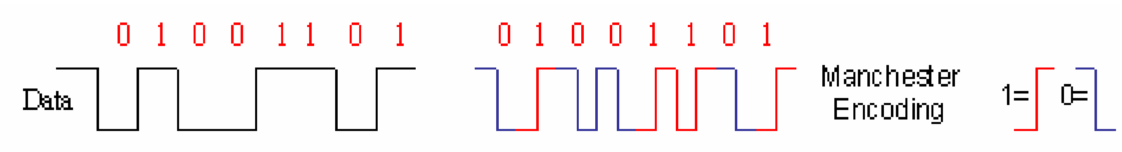

Manchester Encoding

Figure 4-4. Keying schemes [179].

In CMI, a "zero" is encoded by a low-to-high voltage transition, and a "one" is encoded by either a low or a high voltage depending on the state. If "one" follows a voltage high, "one" is encoded as a low. If "one" follows a voltage low, "one" is sent as a high. CMI causes a reduction in data rate by a factor of two. Pulse Position Modulation (PPM) could be seen as a derivative of CMI. When PPM scheme is employed, constant energy per bit is maintained as there is a pulse in every bit [180]. Hamilton, Robinson et al. [146, 180, 181] used binary PPM, encoding "zero" by a pulse in the first half of a bit slot and "one" by a pulse in the second half of a bit slot. At a data rate of 112.5 Gb/s (8.8 ps/bit), the difference in arrival time between a "one" and a "zero" was only 4.4 ps—much shorter than the gain recovery time of the SOA. This allowed for a significant reduction in patterning due to gain saturation as compared to RZ-OOK modulation format.

Manchester Encoding translates a "one" into a low-to-high voltage transition and a "zero" into a high-to-low transition [179]. Differential Phase Shift Keying (DPSK) is a derivative of Manchester Encoding. As with PPM, there is a pulse in every bit slot. A

180^{o} phase shift signifies “ones” and “zeros”. Chan et al. [177] proposes and demonstrates return-to-zero differential phase-shifted-keying (RZ-DPSK) modulation format in optical time-division-multiplexing (OTDM) systems. Instead of representing “ones” and “zeros” by different pulse energies, RZ-DPSK represents the “one” and “zero” bits by phase changes between the adjacent pulses. Consequently, RZ-DSPK offers constant optical energy per bit so as to alleviate pattern-dependent performance degradation in SOA-based demultiplexers. Experimental results showed that RZ-DPSK demonstrates superior performance and robustness compared to RZ-OOK encoding format [177].

4.5 Modeling

Two aspects of SOA modeling are addressed in this work: 1) the interaction between the optical field and the semiconductor material as pulses propagate along the device, 2) nonlinear phase experienced by a signal in an SOA operated in saturation. Coupled rate equations describe the dynamic dependence between the photon density and carrier density in an SOA. The original differential equations [182] are spatially and temporally discretized using first-order finite difference scheme. Next we use an ordinary differential equation solver in Matlab to solve for the time evolution.

Solving a set of finite element rate equations numerically yeilds optical power and carrier density at every point along an SOA for every point in time for a given input pulse. Once the optical power and carrier density are known, we can solve for nonlinear phase as well, as described below. Such modeling allows us to analyze optical amplification and phase of a single pulse passing through an SOA as well as effect of one optical pulse on the gain and refractive index experienced by a subsequent pulse.

4.5.1 Rate equations

Interaction between the free carriers and optical power density in the active region of an SOA is governed by coupled differential equations. For the purposes of numerical modeling, the SOA length is divided into short sections. Rate equations are adapted from [183]. They are modified to take into account wavelength-dependent gain and optical components of different wavelengths as in [144].

Finite element rate equations can be written for free carrier density *N* and *K* spectral components of photon density *S* for each slice *i* as follows:

$$\frac{dN_i}{dt} = \frac{I\eta}{qV_{act}} - (AN_i + BN_i^2 + CN_i^3) - \sum_{k=1}^{K} v_g g(\lambda_k, N_i) S_{i-1,k} \qquad \text{(Eq. 4-3)}$$

$$\frac{dS_{i,k}}{dt} = \frac{v_g}{\Delta z}(S_{i-1,k} - S_{i,k}) - \alpha_i v_g S_{i-1,k} + \Gamma v_g g(\lambda_k, N_i) S_{i-1,k} + \Gamma \beta B N_i^2 \qquad \text{(Eq. 4-4)}$$

where *I* is the injection current, *q* is the electron charge, η is the internal quantum efficiency, V_{act} is active region volume, Δz is the length of the SOA section with index *i*, *A*, *B*, and *C* are unimolecular (nonradiative), bimolecular (radiative), and Auger recombination rate coefficients, respectively, v_g is the group velocity, *g* is the total gain coefficient, N_{tr} is the transparency carrier density, α is the internal loss, Γ is the optical confinement factor, β is the spontaneous emission factor, $\hbar\omega$ and is the photon energy [183]. In calculation where the presence of ASE is neglected, the last term in Eq. 4-4 is omitted.

The total gain coefficient *g* is given by

$$g(\lambda_k, N_i) = \frac{g_m(\lambda_k, N_i)}{1 + \varepsilon_{tot} \sum_{k=1}^{K} S_k}, \qquad \text{(Eq. 4-5)}$$

where g_m is material gain and ε_{tot} is the total nonlinear gain compression factor. It consists of contributions from carrier heating and spectral hole burning [144]:

$$\varepsilon_{tot} = \varepsilon_{CH} + \varepsilon_{SHB} \,. \qquad \text{(Eq. 4-6)}$$

Dependence of modal gain on wavelength and carrier density is described in the next section.

The optical power is related to photon density in the following manner:

$$P_{i,k} = \hbar\omega \cdot S_{i,k} \cdot \frac{L_x L_y v_g}{\Gamma} \,. \qquad \text{(Eq. 4-7)}$$

Here, L_x and L_y are the width and the height of the SOA active region, respectively [183].

We consider the N and S at discrete times t spaced by an increment Δt to solve for time evolution of carrier density and photon density everywhere along the length of the SOA.

4.5.2 Parameterized gain model

In this work we use a polynomial gain model found in [184] and [185]. Leuthold et al. [185] developed the model based on their material gain measurements of bulk 1.55 µm InGaAsP on InP substrate. These measurements were carried out over a large range of carrier densities and a large spectral region. The polynomial model presented in [184, 185] not only provides a good fit to the experimental data over the whole measured range, but also shows stable convergence in simulation tools even when carrier densities exceed the usual range.

Material gain is modeled as a sum of a quadratic and a cubic function:

$$g_m(\lambda, N) = \begin{cases} c_N(\lambda - \lambda_z(N))^2 + d_N(\lambda - \lambda_z(N))^3 & \lambda < \lambda_z(N) \\ 0 & \lambda \geq \lambda_z(N) \end{cases} \qquad \text{(Eq. 4-8)}$$

Where

$$c_N = 3\frac{g_p(N)}{(\lambda_z(N) - \lambda_p(N))^2}, \tag{Eq. 4-9}$$

$$d_N = 2\frac{g_p(N)}{(\lambda_z(N) - \lambda_p(N))^3}. \tag{Eq. 4-10}$$

In Eqs. 4-9 and 4-10 $g_p(N)$ is the material gain versus carrier density at peak wavelength, $\lambda_p(N)$ is the carrier dependence of the peak wavelength, and $\lambda_z(N)$ the wavelength at which the gain falls to zero when λ is increased while carrier density is kept constant.

These functions are chosen to fulfill the following physical conditions for all values of N:

$$g_p(N) > 0 \tag{Eq. 4-11}$$

and

$$\lambda_z(N) > \lambda_p(N). \tag{Eq. 4-12}$$

Leuthold et al. propose approximating these functions by

$$g_p(N) = a_0(N - N_{tr}), \tag{Eq. 4-13}$$

$$\lambda_p(N) = \lambda_0 - b_0(N - N_{tr}), \tag{Eq. 4-14}$$

$$\lambda_z(N) = \lambda_{z_0} - z_0(N - N_{tr}), \tag{Eq. 4-15}$$

where the coefficients N_{tr}, a_0, λ_0, b_0, λ_{z0}, and z_0 are determined from experimental data. N_{tr} is the transparency carrier density at the band edge wavelength λ_0 of the active layer and λ_{z0} is the value of λ_z at the transparency carrier density [185]. To model gain in bulk 1.55 µm InGaAsP lattice-matched to InP, we utilize parameter values found in [144] and [185].

4.5.3 Wave propagation

For numerical simulations, we have discretized the SOA lengthwise into sections of length Δz. We then used a simple finite-difference time-domain (FDTD) model by employing a first order finite-difference spatial approximation of right-hand side of partial differential equation (PDE)

$$\frac{\partial S_k}{\partial t} = -v_g \frac{\partial S_k}{\partial z} - \alpha_i v_g S_k + \Gamma v_g g(\lambda_k, N) S_k + \Gamma \beta B N^2 . \qquad \text{(Eq. 4-16)}$$

The boundary condition at the inlet is determined by the intensity of the input signal. The approximation of the derivative $\frac{\partial S_k}{\partial z}$ corresponds to the first-order upwind scheme. First-order upwind scheme is defined as a forward-in-time, backward-in-space finite-difference approximation of the traveling wave equation [186, 187]. We used a standard ordinary differential equation (ODE) MATLAB solver in order to evaluate time evolution of the photon density components and carrier concentration.

In our numerical simulator we use square input pulses of finite duration. Since these input signals are discontinuous, due to the absence of diffusion in our model, the exact solution of PDE is discontinuous as well. Our first-order upwind scheme is expected to produce a false effect of smoothing this discontinuity, and we observed this in practice (Figure 4-5). This smoothing is solely an artifact of the numerical method and is not expected to have a significant effect on the results because the values of our interest are integral values over the entire pulse duration, namely, the output power and total phase [188].

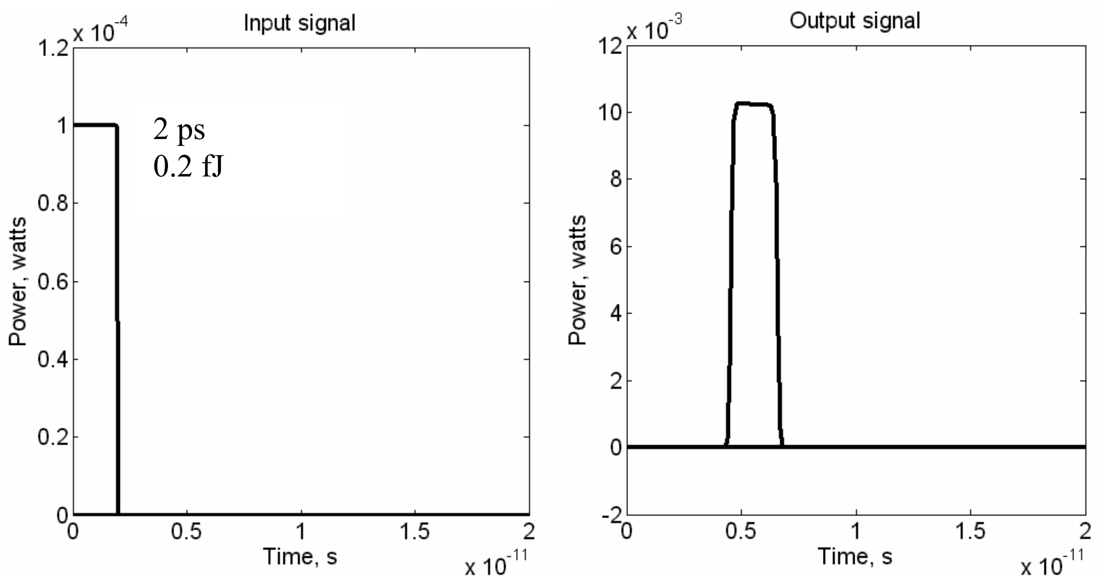

Figure 4-5. Typical input and output of the numeric simulator.

4.5.4 Nonlinear phase

Since our optical circuit employs SOAs for cross-phase modulation, phase behavior of optical signals must be considered. To estimate phase change of an optical signal in an SOA, it is necessary to model nonlinearities in refractive index of the active material. Here we take the most common approach to refractive index modeling: linewidth enhancement factor α is used to relate the refractive index modulation to the changes in gain coefficient in the active material. This relationship was first derived by Henry in 1982 [189]. The α-factor approach is attractive because it can be easily verified experimentally since it links two directly measurable parameters: variation in the gain and phase of the SOA output [144].

Henry originally defined α-factor as ratio of the changes in the real part of refractive index to the changes in the imaginary part of refractive index [189]:

$$\alpha_m = \frac{\Delta \mathrm{Re}(n)}{\Delta \mathrm{Im}(n)}\,. \tag{Eq. 4-17}$$

Subscript *m* stands for “material”, as in material gain g_m, and is used primarily in order to distinguish linewidth enhancement factor from internal waveguide loss coefficient α [144].

Currently α-factor is most often written as a function of partial derivatives of the real part of the refractive index the material gain g_m [190]:

$$\alpha_m = -\frac{4\pi}{\lambda_0}\frac{\frac{\partial n}{\partial N}}{\frac{\partial g_m}{\partial N}}. \qquad \text{(Eq. 4-18)}$$

α_m accounts only for changes in refractive index due to modulation of carrier density. Since gain is also affected by changes in the lattice temperature and distribution of carriers within a band, it is necessary to consider α-factor contributions due to these effects [191]. α-factor due to spectral hole burning (SHB) is considered to be close to zero because contribution of SHB to gain is symmetric with respect to gain [156]. Contribution from two-photon absorption can be neglected for SOA structures under consideration when they are operated with pulses longer than several hundreds of femtoseconds. The coupling between the refractive index and the lattice temperature variation is ignored because the lattice temperature dynamics are slow, on the order of microseconds [190]. Therefore, it is sufficient to take into consideration α-factor due to carrier heating (α_m) and due to changes in carrier density (α_{CH}) [144].

Nonlinear phase induced by changes in carrier density and carrier heating is given by

$$\varphi_i(N_i) = \varphi_i(N_{ref}) - \frac{1}{2}\Delta z\left(\alpha_m \Gamma(g_m(N_i) - g_m(N_{ref})) - \frac{\alpha_{CH}\varepsilon_{CH}S_i g_m(N_i)}{1+\varepsilon_{tot}S_i}\right) \qquad \text{(Eq. 4-19)}$$

where $\varphi_i(N_{ref})$ is the total phase accumulated by a signal in segment *i* at the reference carrier density N_{ref}. α_{CH} relates the phase change to carrier heating. This factor is considered a constant. α_m gives the phase change due to variation in carrier density. Dependence of α_m on the carrier density and wavelength is parameterized as follows [144, 184]:

$$\alpha_m(\lambda, N) = \alpha_{N_0} + \alpha_{N_1} e^{\alpha_{N_2}(\lambda - \lambda p(N)) + \alpha_{N_3}(N - N_{tr})}. \qquad \text{(Eq. 4-20)}$$

This parameterization is based on measurements of the material gain and refractive index in [184].

4.5.5 Simplifying assumptions

Reflection of optical power into the SOA from the end facets of the device is neglected completely. According to the analysis in Chapter 3, reflections are expected to be very low. Reflections from taper tips were estimated by FDTD calculations with perfectly matched layer boundary conditions to be on the order of 10^{-4} or lower. In fact, the approximation based on effective indices of fundamental modes before and after the junction yields reflection figure on the order of 10^{-8}. If the SOA is also tilted by approximately 7°, reflections are reduced further. In principle, anti-reflection coating can also be added to decrease reflectivity, although this method should not be necessary to use with the tapers. While in high-gain SOAs $R \sim 10^{-4}$ is often sufficiently high to cause gain ripple, we can be confident that reflection coefficient in our tapered devices can be reduced enough to make this effect negligible.

The majority of calculations performed in this work neglect the presence of amplified spontaneous emission in SOA. A model that does not include ASE can give adequate first approximations for the following reasons. Accounting for ASE is more crucial for linear amplifier applications than it is for non-linear SOA as the latter are saturated by optical signals whose levels are much higher than ASE component intensities. On the other hand, ASE plays a more prominent role in longer devices and devices operated at higher injection current density. Since moderate linear amplification can be performed by short SOAs at relatively low injection current densities, neglecting ASE in the first-generation simulation tool is justified.

4.6 Major examples

The goal of this SOA study is to determine whether it is feasible to develop linear and non-linear devices on the same wafer. It is especially attractive to achieve both functions using the same material layers. There is no mature commercial SOA CAD tool currently available. While developing a comprehensive CAD tool for SOAs would be extremely useful, it is unfortunately beyond the scope of this work. Here we show how valuable insights into SOA design can be gained from relatively simple modeling by examining relevant functional dependences of gain and phase shift on geometric and operational parameters of an SOA.

Requirements for linear SOAs in a balanced MZI include high linearity and moderate gain. In contrast, requirements for non-linear SOAs emphasize large nonlinearity, in particular, non-linear phase on the order of π. The level of gain in non-linear SOAs is not crucial. The second, nonlinear problem is more challenging and its requirements exert more influence on the design. Specifically, it is necessary to design devices with a high confinement factor in order to have an SOA saturate easily. Our estimates in this section will show that all SOAs on a PIC chip, those employed as linear amplifiers and those providing non-linear phase shift, can share composition and cross-sectional geometry. Requirements for linear or non-linear operation can be satisfied by an appropriate choice of SOA length and bias current density.

Nearly all SOAs modeled in this work share the same layer composition and cross-sectional geometry illustrated in Figure 3-3. $In_{0.56}Ga_{0.44}As_{0.93}P_{0.07}$ bulk active region has a thickness of 200 nm. It is surrounded by two 100 nm thick $In_{0.79}Ga_{0.21}As_{0.45}P_{0.55}$ cladding layers. Higher index of quaternary layers surrounded by InP material provides optical confinement in the vertical direction. A 2 μm wide, 1.05 μm high ridge is etched in the structure provides lateral optical confinement. Fundamental mode of the structure is calculated using BeamPROP. Confinement factor $\Gamma=0.4$ is determined by calculating the fraction of mode power within the active region. These cross-sectional parameters apply to every SOA simulated below, unless specified otherwise.

4.6.1 Amplified Spontaneous Emission

While our model does not include a rigorous treatment of amplified spontaneous emission (ASE), if offers us an opportunity to examine general trends of ASE power in SOA as a function of device length and injection current density. In order to study behavior of ASE output power, we examined ASE power as a function of injection current density for a relatively short (0.4 mm) (Figure 4-6) and a relatively long (1.5 mm) device (Figure 4-7). For simplicity, we considered only one component of ASE at 1560 nm, the wavelength corresponding to the gain peak. Since in physical devices ASE has a finite spectrum, the values obtained from the simplified calculations are not reliable. However, the trends that ASE power displays are still informative.

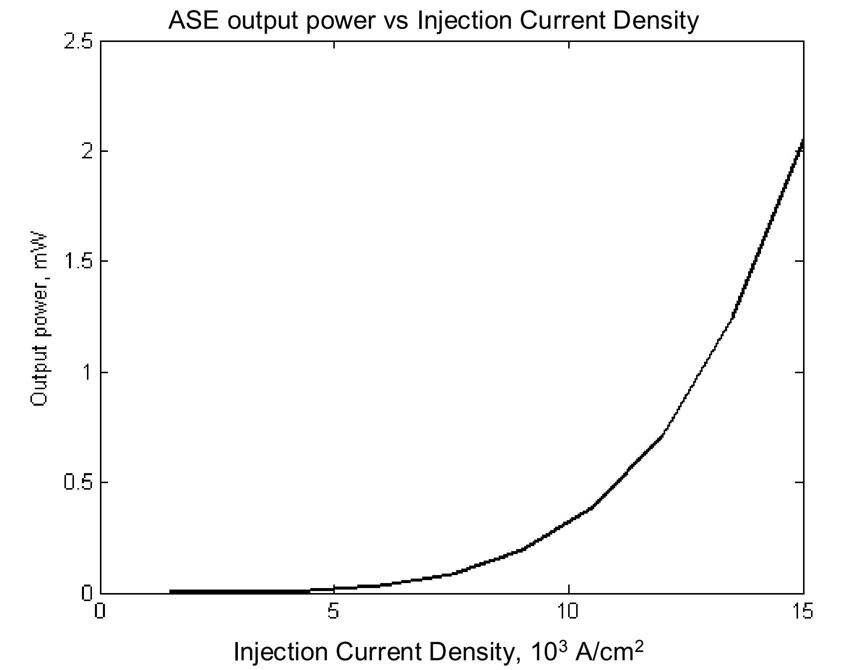

Figure 4-6. ASE power as a function of injection current density, L_{SOA}=0.4 mm.

The results roughly follow a P-I curve of a laser diode [144]. At low injection currents, the output is low and is dominated by spontaneous emission. Once injection current rises above a threshold value, stimulated spontaneous emission takes over and output power rapidly increases. For the longer device, the rise of output power slows down for increasing values of injected current density. This is an evidence of saturation behavior.

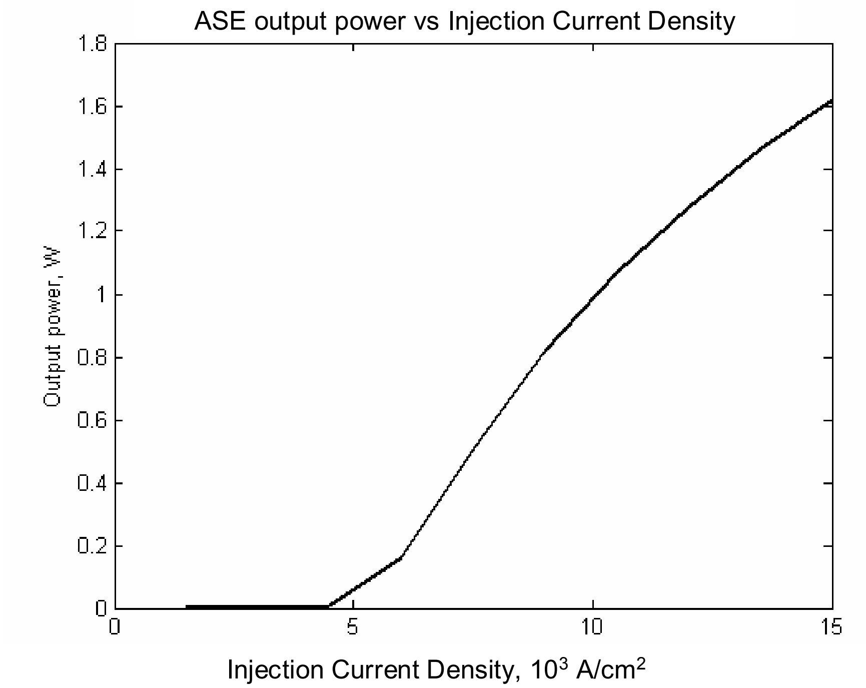

Figure 4-7. ASE power as a function of injection current density, L_{SOA}=1.5 mm.

To examine saturation of long SOAs by ASE in the absence of optical input, we look at output power as a function of SOA length for a constant current density of $8x10^3$ A/cm^2 (Figure 4-8). Predictably, the ASE output power increases with increasing SOA length when the length is moderate and displays saturation once device length is sufficiently large. According to Figure 4-8, ASE output power rises approximately linearly with increasing SOA length up to L_{SOA}~1 mm and remains constant for L_{SOA} greater than approximately 1.5 mm. We can conclude from these results that, for a particular injection current level, a sufficiently long SOA is saturated by ASE alone.

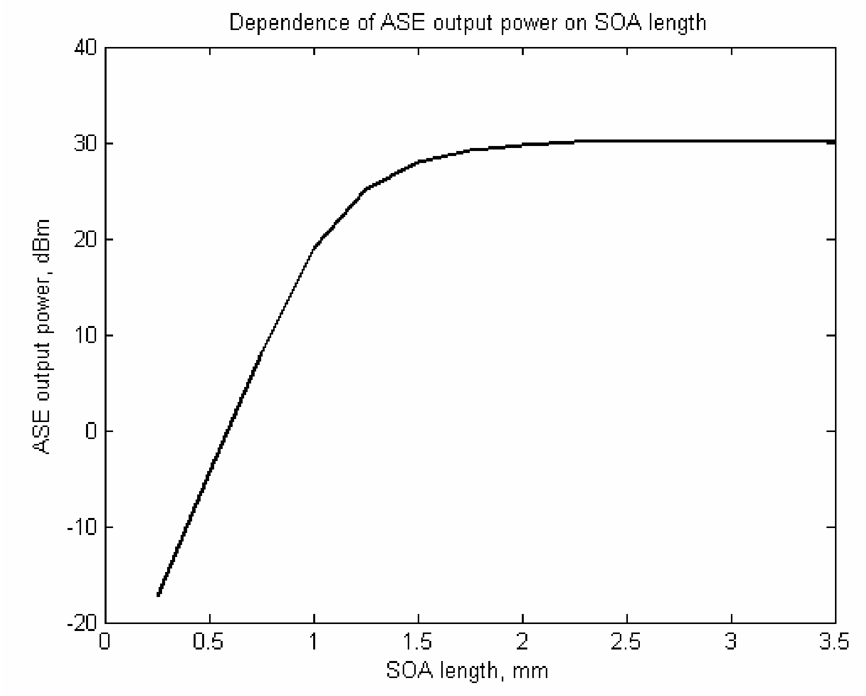

Figure 4-8. ASE power as a function of SOA length, J=8x10^3 A/cm^2.

4.6.2 Linear amplifier

4.6.2.1 Gain saturation

To operate a SOA as a linear amplifier, it is necessary to determine the range of device parameters and operating conditions where gain is essentially independent of optical signal energy or, in other words, unsaturated. A gain saturation curve, such as in Figure 4-9, confirms the validity of our model by demonstrating appropriate device behavior: reduction of gain with increasing input pulse energy. In particular, Figure 4-9 illustrates saturation in a 400 μm-long SOA operated at injection current of J=8x10^3 A/cm^2 injection current density. Gain is reduced by 3 dB for output power of 22 dBm. Corresponding input power is 4.5 dBm (~3 mW).

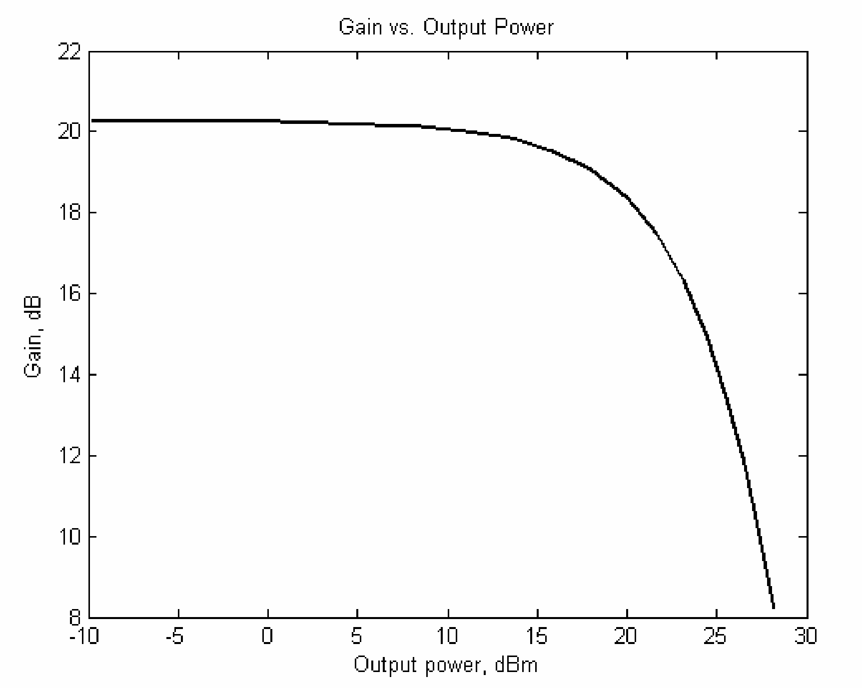

Figure 4-9. Gain saturation, L_{SOA}=0.4 mm, J=8x10^3 A/cm^2.

4.6.2.2 Small signal gain

Next we examine the dependence of small signal gain (SSG) on signal wavelength, SOA length, and injection current density. Small signal gain is the maximum gain achievable in an amplifier. SSG is attained when optical signal is sufficiently weak to cause negligible gain compression [144]. Figure 4-10 shows SSG as a function of signal wavelength. This dependence is inspected primarily to confirm proper behavior of the simulation program as the function is largely defined by our wavelength-dependent gain model (see Section 4.5.2). The gain peak occurs at a wavelength of ~1560 nm. Gain is reduced by 3 dB or more for wavelengths below 1535 nm and above 1580 nm.

Figure 4-11 shows SSG as a function of injection current density for 400 μm long device. As expected, SSG increases with a rising current density. Modest saturation behavior is observed because the carrier recombination rate increases more rapidly than carrier injection rate directly proportional to the injected current. The main contribution to the faster recombination rate is due to the cubic Auger recombination term, CN^3 [144].

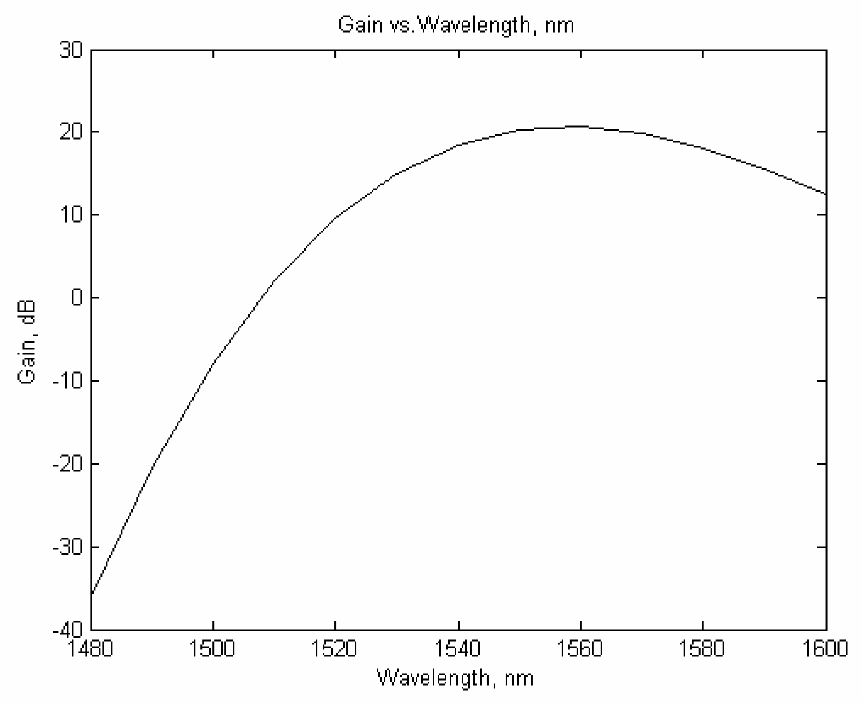

Figure 4-10. Small signal gain as a function of wavelength, L_{SOA}=0.4 mm, J=8x10^3 A/cm^2.

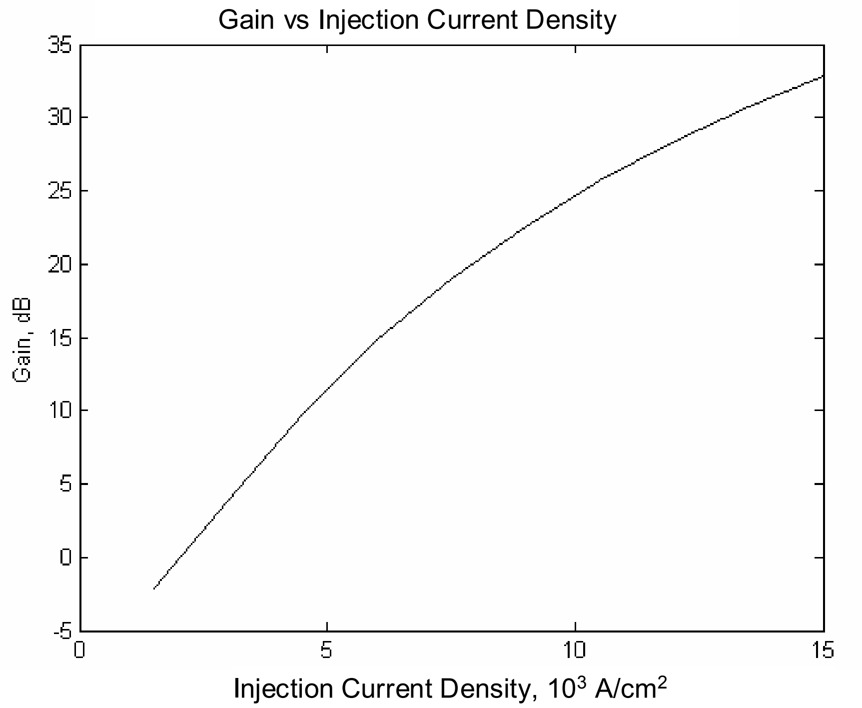

Figure 4-11. Small Signal Gain as a function of injection current density, L_{SOA}=0.4 mm.

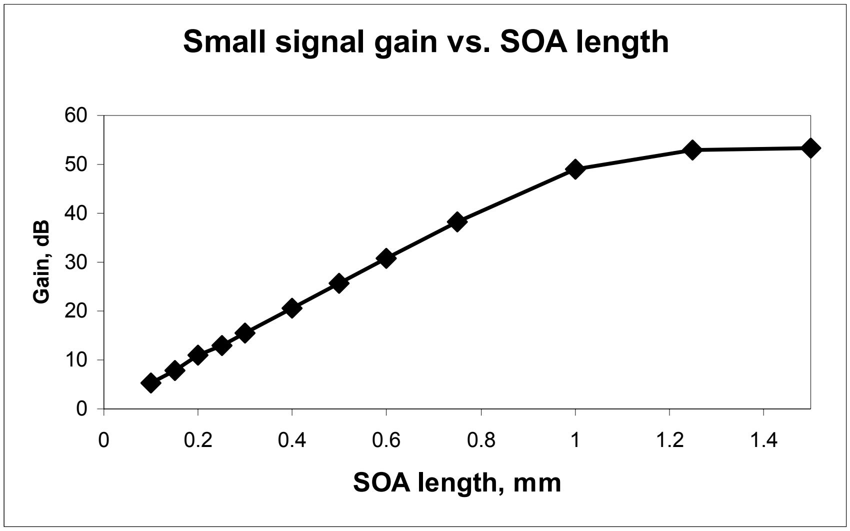

Figure 4-12. Small Signal Gain as a function of SOA length, J=8x10^3 A/cm^2.

Figure 4-12 illustrates dependence of SSG on SOA length for injection current density of J=8x10^3 A/cm^2. This injection current density was chosen as medium injection current density level based on the data for similar SOA devices described in

[144]. The plot shows that gain is approximately linear with SOA length for devices up to a length of about 1-1.2 mm.

4.6.3 Output saturation power

Output saturation power (P_{SATout}) corresponds to conditions when SOA gain is reduced by 3 dB from its SSG level. Dependence of P_{SATout} on confinement factor, SOA length, and injection current density was examined. Nominal values are Γ=0.4, L_{SOA}=400 μm, and J=8x10^3 A/cm^2. Confinement factor Γ was varied between 0.04 and 0.4 (active region thickness was scaled accordingly). Results are presented in Figure 4-13. For small values of confinement factor, P_{SATout} decreases with increasing Γ. For higher values of confinement factor, output saturation power remains approximately constant. SOA length L_{SOA} was varied between 0.1 mm and 1.0 mm (Figure 4-14). P_{SATout} decreases rapidly with increased SOA length for short devices, has a minimum near L_{SOA}=0.4 mm, and increases slowly for devices of L_{SOA}=0.5 mm or longer. Injection current density was varied between 3x10^3 A/cm^2 and 12x10^3 A/cm^2 (Figure 4-15). P_{SATout} falls with increasing injected current density for small values of J and remains steady for larger current densities. All these observations point to the fact that output saturation power is larger in SOAs providing low gain. P_{SATout} decreases to an approximately constant value when SSG becomes greater than 10 dB.

These results are in agreement with Occhi [144] and Eisenstein et al. [192] who state that for very short devices P_{SATout} decreases with increasing length while for longer devices P_{SATout} remains constant. We note that such behavior of output saturation power can be observed not only with respect to SOA length, but extends to other parameters affecting SOA gain, namely, confinement factor and injection current density.

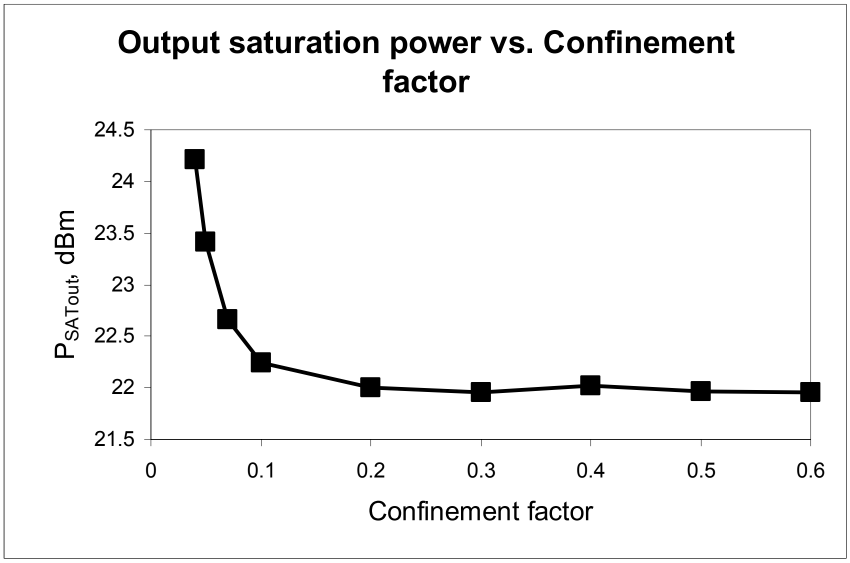

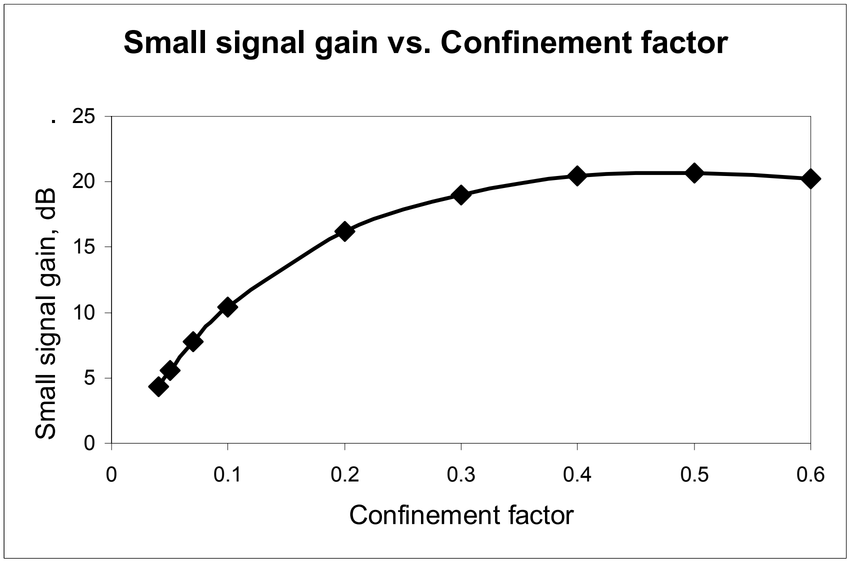

Figure 4-13. Output saturation power and small signal gain as a function of confinement factor, L_{SOA}=0.4 mm, J=8x10^3 A/cm^2.

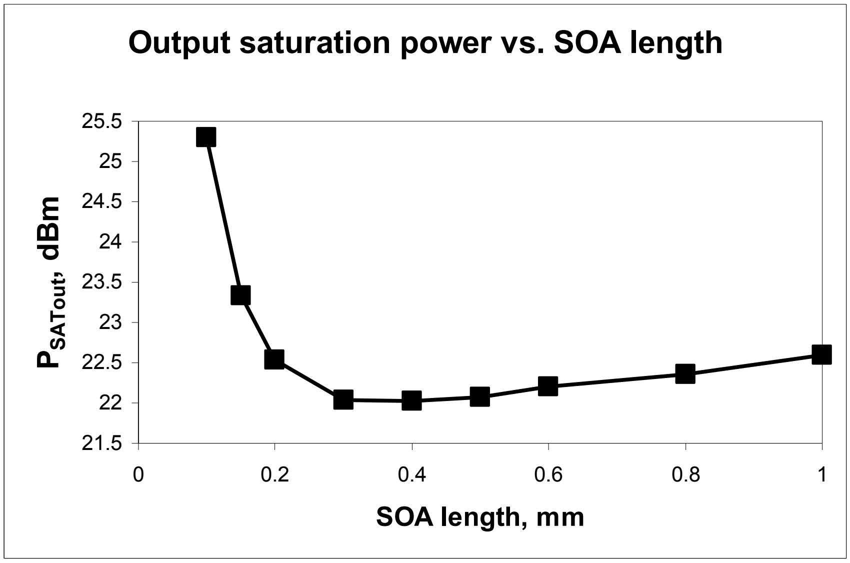

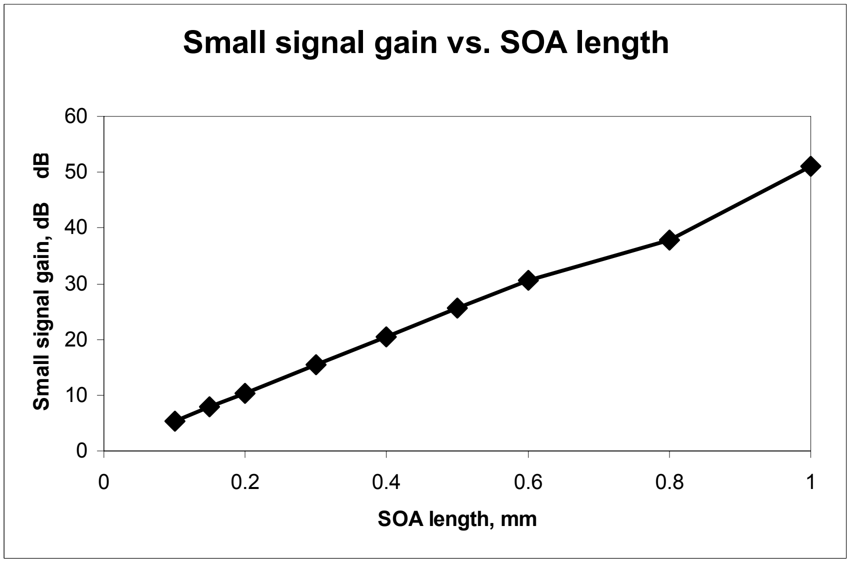

Figure 4-14. Output saturation power and small signal gain as a function of SOA length, J=8x10^3 A/cm^2.

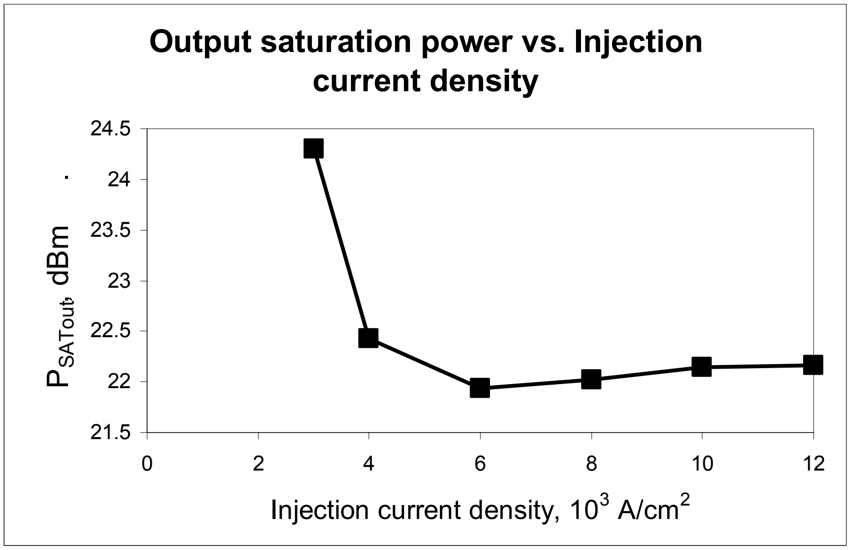

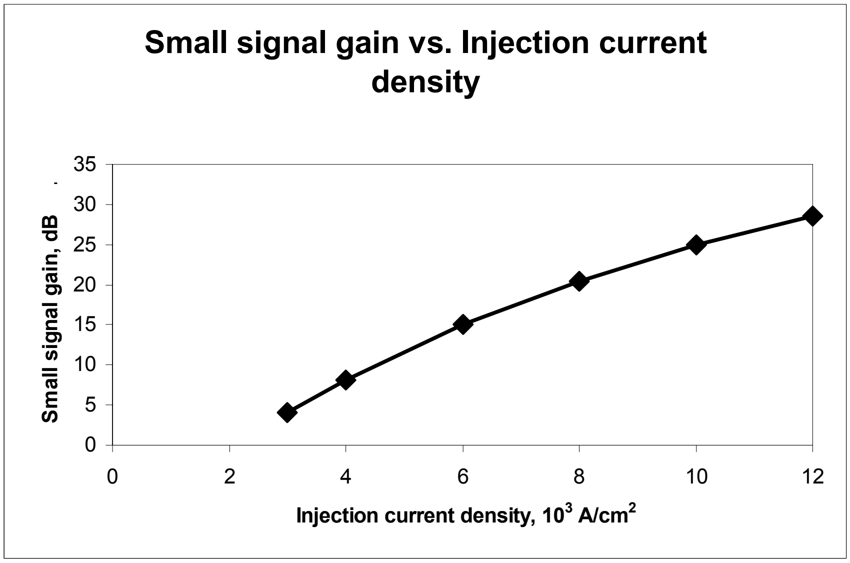

Figure 4-15. Output saturation power and small signal gain as a function of injection current density, L_{SOA}=0.4 mm.

4.6.4 Device Optimization

4.6.4.1 SOA for linear amplification

The goal of linear SOA optimization is to design a device which yields moderate gain for the lowest possible injection current. We chose to study SOA operation when a

2 ps long, 100 fJ pulse is used as an input. Devices were designed for 4 dB gain. Figure 4-16 shows dependence of SOA gain on device length and injection current density. SOA length was varied between 0.1 mm and 1.0 mm and injection current density was varied between 3×10^3 A/cm^2 and 12×10^3 A/cm^2.

There is clearly a tradeoff between device length and injection current density. A relatively high injection current density of 9×10^3 A/cm^2 is needed to achieve gain over 4 dB for the shortest SOA, 0.1 mm in length. A significantly longer device, L_{SOA}~0.7 mm, is required to achieve the same gain at the lowest injection current density of 3×10^3 A/cm^2. If injection current density is lowered further, the SOA will no longer function as an amplifier. For 0.7 mm long devices with the cross-section and composition designed for this work, current density of 3×10^3 A/cm^2 corresponds to 42 mA current. For 0.1 mm long devices, current density of 9×10^3 A/cm^2 corresponds to 18 mA current. We can conclude that in order to achieve desired gain while minimizing injected current, we should choose a short device. In Figure 4-17, the same data as in Figure 4-16 is represented in a different fashion in order to demonstrate that the shortest devices are optimal for linear amplification.

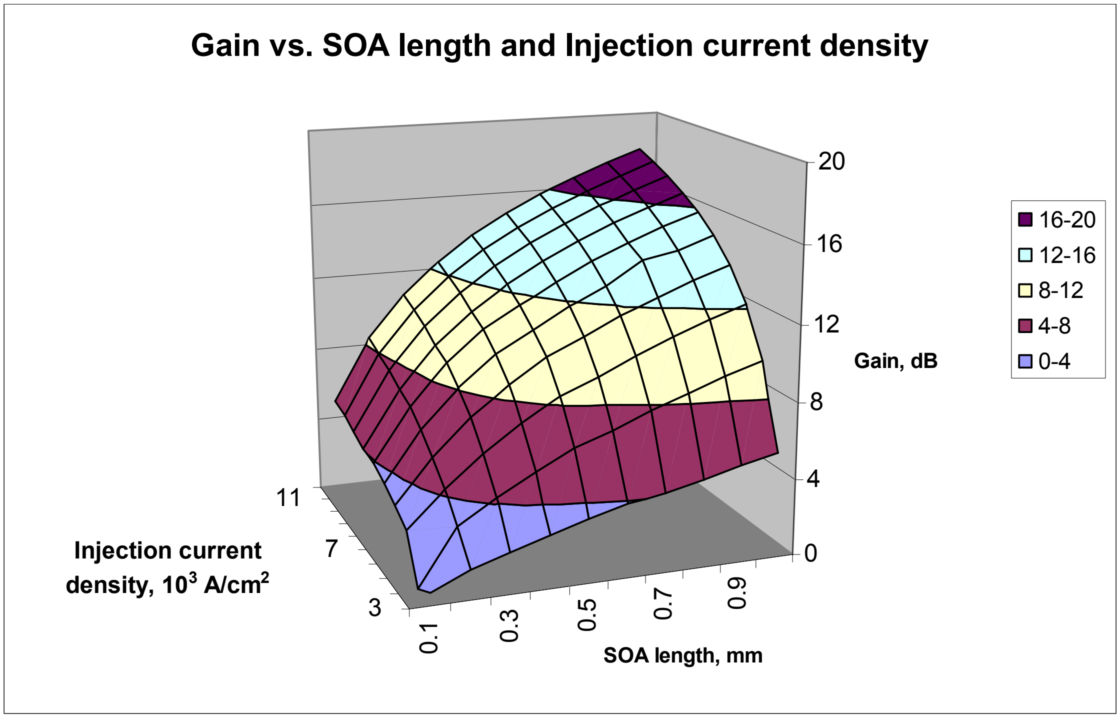

Figure 4-16. Gain as a function of SOA length and injection current density.

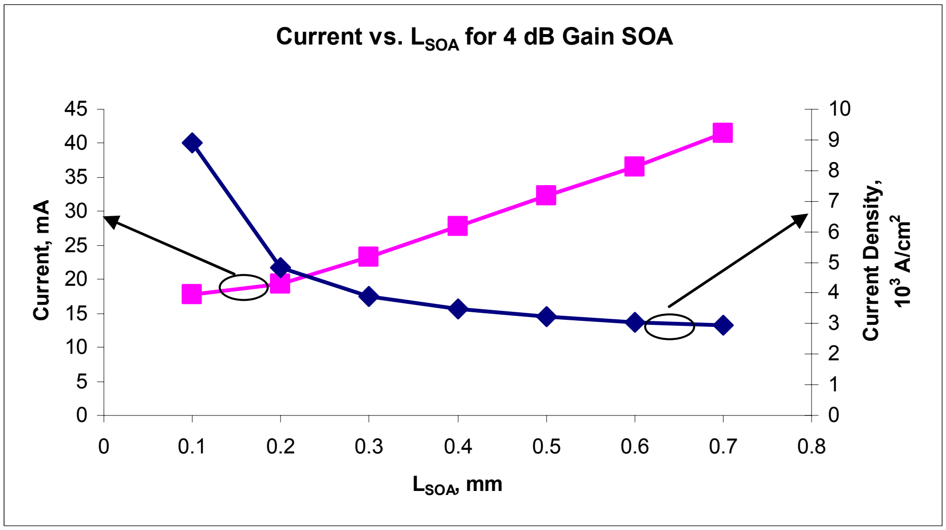

Figure 4-17. Bias current for different SOA lengths to achieve 4 dB gain.

In order to employ the SOA as a linear amplifier, linear behavior of the device must be examined. To evaluate linear performance, we compare gain experienced by 100 fJ pulse with gain experienced by a pulse with 50% more energy, 150 fJ. For a 0.1 mm long device operated at $9\text{x}10^3$ A/cm^2, gain decreases by 10% for a 150 fJ pulse compared to 100 fJ pulse. For a 0.7 mm long device operated at $3\text{x}10^3$ A/cm^2, gain decreases by 14% for a 150 fJ pulse compared to 100 fJ pulse. A shorter SOA operated at a higher injection current density displays better linearity than a longer device operated at a lower injection current density to achieve the same gain. These results are displayed in Table 4-1.

Signal Energy L_{SOA}, J	100 fJ	150 fJ	200 fJ
0.1 mm, 9 $\text{x}10^3$ A/cm^2	4.06 dB	3.61 dB	3.27 dB
0.7 mm, $3\text{x}10^3$ A/cm^2	4.15 dB	3.49 dB	2.98 dB

Table 4-1 Gain in long and short SOA as a function of input pulse energy.

4.6.4.2 SOA as a phase shift element

An SOA used as a phase shifter has to yield a nonlinear phase shift of π. As with the linear device optimization, we used 2 ps long, 100 fJ pulse as an input. SOA length was varied between 0.4 mm and 1.6 mm and injection current density was varied between $7\text{x}10^3$ A/cm^2 and $16\text{x}10^3$ A/cm^2. The values for both device length and current density are significantly higher than in the case of linear SOA since higher SOA length and injection current level are necessary to achieve nonlinear SOA operation.

Figure 4-18 illustrates nonlinear phase as a function of SOA length and injection current density. As expected, phase increases can be achieved by increasing either parameter, representing a tradeoff between device length and injection current density. The desired phase shift of greater than π can be produced in a 0.5 mm SOA by using a high injection current density of $16\text{x}10^3$ A/cm^2, corresponding to 160 mA of current. Required injection current density can be lowered if a longer SOA is used. For example, a 0.85 mm SOA needs injection current density of 7x10^3 A/cm^2 to produce π phase shift. Corresponding current is 119 mA.

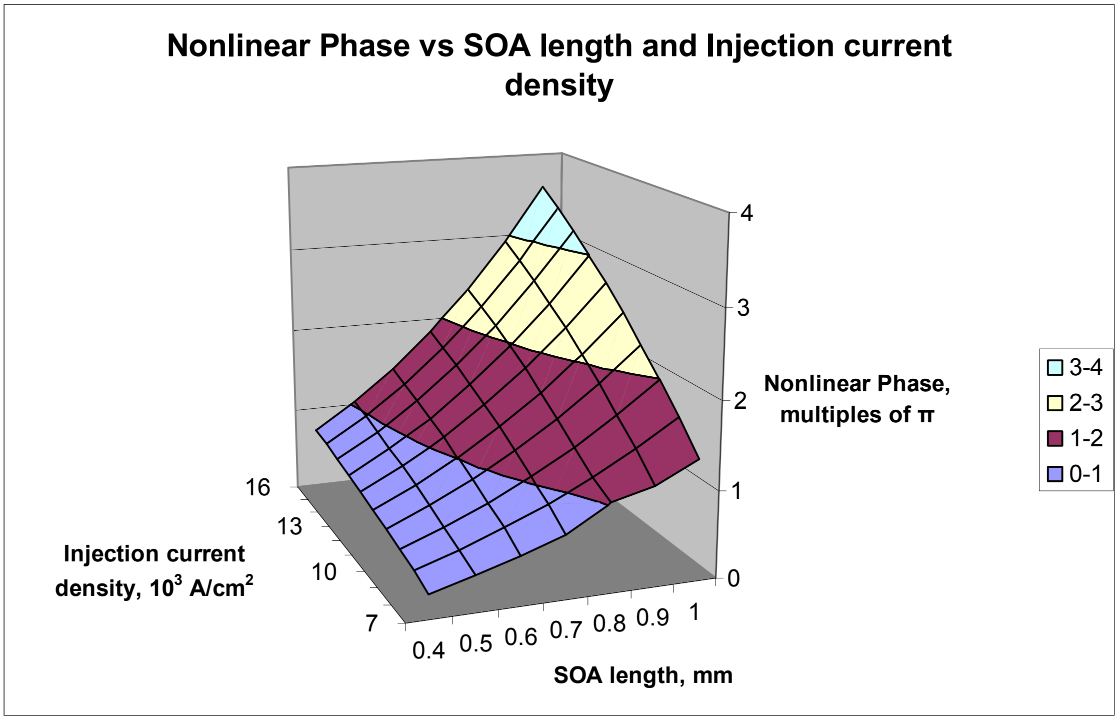

Figure 4-18. Nonlinear phase as a function of SOA length and injection current density.

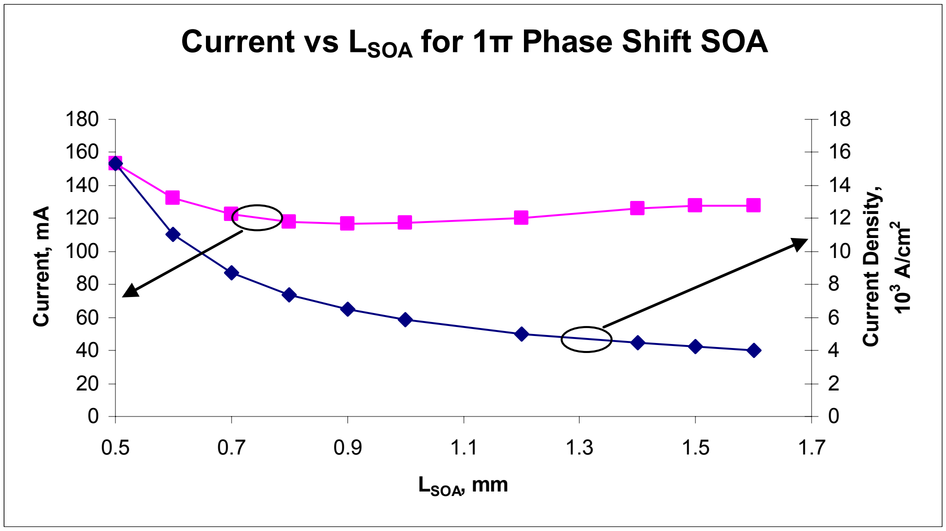

Figure 4-19. Nonlinear phase as a function of bias current.

Total current depends linearly on both the injection current density and SOA length. Nonlinear phase experiences a faster increase with the SOA length than it does with injection current density. Therefore, a longer SOA operating at a lower injection current density requires less total current to produce π phase shift than does a shorter SOA operating at a higher injection current density. Figure 4-19 shows that longer SOAs require less total current draw in order to achieve required phase shift. The observation that there is no further improvement beyond 0.85 mm SOA lengths is explained by saturation.

In our design of optical logic unit cell, 0.85 mm long SOAs are incorporated into the arms of Mach-Zehnder interferometer. The above calculations demonstrate that such SOAs produce required phase shift of π when biased at $J=7x10^3$ A/cm^2. The corresponding gain in 0.85 mm SOA is 13.9 dB.

4.6.5 Conclusions

We demonstrated a strategy for development of SOAs for linear amplification and phase shifting using the same layered semiconductor structure as designed for the passive ATG device. To satisfy requirements for a sufficiently large phase shift in a non-linear device, we chose a structure with a large confinement factor.

Linear devices can be obtained by choosing short SOA length and moderate injection current densities. There is a tradeoff between device length and injection current density. In order to use less total bias current and to attain higher linearity, short SOA should be chosen. Although a shorter device requires higher injection current density to yield target level of gain, total current drawn by such device is lower than that of a longer device operated at a higher current density.

Required phase shift can be achieved by building relatively long SOAs and operating them at a high injection current density. Nonlinear phase rises with increasing device length and injection current density, representing a tradeoff similar to that which applies to linear amplifiers. In the case of phase shifter SOA, total bias current is minimized by choosing a longer device operated at a lower injection current density. In other words, linear and non-linear SOAs can be optimally operated at similar injection current density levels, with non-linear devices having a significantly longer length.

Finally, we compare gain in a nonlinear SOA of the unit logic cell with the overall loss in the passive components and couplers found in Chapter 3. The chosen design includes 0.85 mm SOAs biased at $J=7x10^3$ A/cm^2. Each SOA produces 13.9 dB of gain when the circuit is operated with 2 ps, 100 fJ pulses. Therefore, we conclude that the gain in the nonlinear SOA compensates for the loss in the passive components of the unit logic circuit and provides an additional amplification. It is not necessary to include linear amplifiers in our design when it is operated with 2 ps, 100 fJ pulses.

142. B.E.A. Saleh and M.C. Teich, *Fundamentals of Photonics*. 1991: John Wiley and Sons, Inc.

143. M. J. Adams, et al., *Nonlinearities in Semiconductor Laser Amplifiers.* Optical and Quantum Electronics, 1995. **27**(1).

144. Lorenzo Occhi, *Semiconductor Optical Amplifiers Made of Ridge Waveguide Bulk InGaAsP/InP: Experimental Characterisation and Numerical Modelling of Gain, Phase, and Noise*. 2002, Eidgenössische Technische Hochschule Zürich.

145. Jesper Mørk, Mads L. Nielsen, and a.T.W. Berg, *The Dynamics of Semiconductor Optical Amplifiers: Modeling and Applications.* Optics and Photonics News, 2003(8): p. 42-48.

146. Bryan S. Robinson, *Semiconductor-based all-optical switching for optical time-division multiplexed networks*, in *Electrical Engineering and Computer Science*. 2003, Massachusetts Institute of Technology: Cambridge.

147. J. J. Chen, et al., *The gain decompression effect and its applications to very fast wavelength conversions.* Photonics Technology Letters, IEEE, 1997. **9**(6): p. 755-757.

148. T. Saito and T. Mukai, *Recent progress in semiconductor laser amplifers.* Journal of Lightwave Technology, 1988. **6**(11): p. 1656-1664.

149. Jean-Jacques Bernard and M. Renaud, *Semiconductor optical amplifiers.* OE magazine, 2001(9).

150. R. Prakasam, et al., *Practical approach to design and fabrication of antireflection coatings for semiconductor optical amplifiers.* Photonics Technology Letters, IEEE, 1996. **8**(4): p. 509-511.

151. Martin Hansson, *Optical Amplifiers*. 2005, Dept. of Electrical Engineering, Linköping University: Sweden.

152. S. Kitamura, et al., *Angled facet S-bend Semiconductor optical Amplifiers for high-gain and large extinction ratio.* IEEE Photonic Technology Letters 1999. **11**(7): p. 788-790.

153. K. Djordjev, S.J.C., W.J. Choi, S.J. Choi, I. Kim and P. Dapkus, *Two-segment spectrally inhomogeneous traveling wave semiconductor optical amplifiers applied to spectral equalization.* IEEE Photonic Technology Letters, 2002. **14**(5): p. 603-605.

154. E.M. Koontz, *The Development of Components for Ultrafast All-Optical Communication Networks*, in *Electrical Engineering and Computer Science*. 2000, Massachusetts Institute of Technology: Cambridge.

155. R.J. Manning, et al., *Semiconductor Laser Amplifiers for Ultrafast All-Optical Signal Processing.* of Optical Society of America B, 1997. **14**: p. 3204.

156. K. Hall, et al., *Subpicosecond gain and index nonlinearities in InGaAsP diode lasers.* Optical Commununications, 1994. **111**: p. 589-612.

157. A. Markina, G. S. Petrich, and L. A. Kolodziejski, *Towards Integrated Photonic Circuits*. 2002, Research Laboratory of Electronics, Massachusetts Institute of Technology.

158. A. Corchia, et al. *Dispersion compensation using mid-span spectral inversion without frequency shift,*. in *ECOC*. 1998. Madrid.

159. Ch. Holtmann, *Polarization Insensitive Semiconductor Optical Amplifiers in InGaAsP/InP for 1.3 um Wavelengths Exploiting Bulk Ridge-Waveguide Structure*. 1997, ETH.

160. H. Ghafouri-Shiraz, *The principles of semiconductor laser diodes and amplifiers : analysis and transmission line laser modeling*. 2004, London: Imperial College Press.

161. L. Chrostowski, et al. *Study of long-wavelength directly modulated VCSEL transmission using SOA amplifiers*. 2001.

162. M. E. Marhic, et al., *Toward Practical Fiber Optical Parametric Amplifiers and Oscillators.* Optics and Photonics News, 2004(9): p. 19-25.

163. Fow-Sen Choa, *Ultra-Broadband Gain Materials*. 2002, Department of Computer Science and Electrical Engineering, University of Maryland Baltimore County.

164. Y. Ding, et al. *Growth and characterization of GaAs/AlAs superlattices: evidence of quasi-indirect transition between miniband*. in *CLEO* 2002. Long Beach, CA.

165. M. Xiaodong, et al. *Growth and characterization of GaAs/AlAs superlattices: evidence of quasi-indirect transition between minibands*. 2002.

166. J. B. Khurgin, et al., *Reduced crosstalk semiconductor optical amplifiers based on Type-II quantum wells.* Photonics Technology Letters, IEEE, 2002. **14**(3): p. 278-280.

167. Phil Harvey, *Genoa Amps Up*, in *Light Reading*. 2001.

168. Jie Lin, et al., *A low-crosstalk semiconductor optical amplifier.* Photonics Technology Letters, IEEE, 2004. **16**(2): p. 392-394.

169. Jie Lin, Junping Zhang, and Fow-Sen Choa. *Low-crosstalk semiconductor optical amplifiers*. 2002.

170. J. H. Chen, X.Z., F. S. Choa. *Design consideration of semiconductor optical amplifier linearity*. in *IEEE LEOS Annual Meeting*. 1997. San Francisco, CA.

171. InPhenix, *The Enhanced Functionalities of Semiconductor Optical Amplifiers and their Role in Advanced Optical Networking*. 2004: Livermore, CA.

172. A.V. Uskov, *Potential of Quantum Dot Semiconductor Optical Amplifiers for high-speed optical processing*. 2004.

173. A.V. Uskov, et al., *Carrier-induced refractive index in quantum dot structures due to transitions from discrete quantum dot levels to continuum states.* Applied Physics Letters, 2004. **84**(2).

174. A.V. Uskov, T.W. Berg, and J. Mork. *Quantum dot semiconductor optical amplifiers: possibility of amplification of high bit rate pulse trains without patterning effects*. in *Quantum Electronics Conference*. 2003.

175. A.V. Uskov, T.W. Berg, and J. Mork, *Theory of pulse-train amplification without patterning effects in quantum-dot semiconductor optical amplifiers.* Quantum Electronics, IEEE Journal of, 2004. **40**(3): p. 306 – 320.

176. Fujitsu. *Fujitsu Develops World's First Semiconductor Optical Amplifier with Signal Waveform Re-shaping Function at 40Gbps, Uses quantum dots to eliminate waveform degradation and significantly reduce noise*. 2005 [cited 2005 April 6]; Available from: http://www.fujitsu.com/global/news/pr/archives/month/2005/20050304-01.html.

177. K. Chan, et al., *Mitigation of Pattern-Induced Degradation in SOA-Based All-Optical OTDM Demultiplexers by Using RZ-DPSK Modulation Format.* IEEE Photon. Tech. Lett., 2003. **15**(9): p. 1264-1266.

178. *Data Encoding Techniques*. 2005 [cited 2005 August 10]; Available from: http://www.rhyshaden.com/encoding.htm.

179. *Engineering Definitions*. 2005 [cited 2005 May 11]; Available from: http://www.interfacebus.com/Definitions.html.

180. Scott A. Hamilton, et al., *100 Gb/s Optical Time-Division Multiplexed Networks.* Journal of Lightwave Technology, 2002. **20**(12): p. 2086-2100.

181. B. S. Robinson, S. A. Hamilton, and E. P. Ippen, *Demultiplexing of 80-Gb/s pulse-position modulated data with an ultrafast nonlinear interferometer.* Photonics Technology Letters, IEEE, 2002. **14**(2): p. 206-208.

182. A. E. Siegman, *Lasers*. 1986, Mill Valley, CA: University Science Books.

183. D. Luerssen, et al., *Thermal profiling: locating the onset of gain saturation in semiconductor optical amplifiers.* Photonics Technology Letters, IEEE, 2004. **16**(7): p. 1625-1627.

184. J. Leuthold, et al., *Multimode interference couplers for the conversion and combining of zero- and first-order modes.* Journal of Lightwave Technology, 1998. **16**(7): p. 1228 –1239.

185. J. Leuthold, et al., *Material gain of bulk 1.55 um InGaAsP/InP semiconductor optical amplifers approximated by a polynomial model.* Journal of Applied Physics, 2000. **87**(1): p. 618-620.

186. J.C. Strikwerda, *Finite Difference Schemes and Partial Differential Equations*. Mathematics Series. 1989: Wadsworth & Brooks/Cole.

187. L.N. Trefethen, *Finite Difference and Spectral Methods for Ordinary and Partial Differential Equations*, in *Cornell University Lecture Notes*. 1996.

188. D. Vasilyev, *Personal communication*. 2005: Cambridge, MIT.

189. C. H. Henry, *Theory of the linewidth of semiconductor lasers.* Quantum Electronics, IEEE Journal of, 1982. **18**(2): p. 259-264.

190. L. A. Coldren and S.W. Corzine, *Diode Lasers and Photonic Integrated Circuits*. 1995: John Wiley and Sons, Inc.

191. C. Z. Ning, *Partial and total alpha parameters in semiconductor optical devices.* Applied Physics Letters, 1998. **72**(15): p. 1887-1889.

192. G. Eisenstein, et al., *Length dependence of the saturation characteristics in 1.5-μm multiple quantum well optical amplifiers.* Photonics Technology Letters, IEEE, 1990. **2**(11): p. 790-791.

5 Summary and Directions for Future Work

5.1 Summary

5.1.1 Passive devices

We justified the use of Beam Propagation Method for long devices with constant or slowly-varying cross-section: passive ridge waveguides, multimode interference couplers, and adiabatic taper couplers. We demonstrated how dilute InGaAsP/InP structures can be used in place of difficult-to-manufacture bulk quaternary material with low arsenic concentration. This improvement in material quality and manufacturability comes at a cost of somewhat increased polarization sensitivity. We determined that the effective index of ridge waveguides is highly insensitive to etch depth variation, but somewhat sensitive to variations in quaternary material composition. If material composition variation results in a higher index of the quaternary material, single-mode waveguide can still be fabricated by reducing the ridge width.

We assessed two types of losses in curved waveguides: those due to the waveguide bend and those due to mode mismatch at the transition point between waveguides of different curvatures. We described unsuccessful attempts to calculate bending losses using standard BPM software and proceeded to compute the losses using finite-difference method with cylindrical PML. Curved waveguides with a typical cross-section used in this project and a bending radius of 300 μm or higher experience loss of 1.5 dB or less. We also demonstrated a method for optimizing offsets between waveguides of different curvature using BPM techniques.

Comparison between approximate theoretical results and BPM simulations reveal that theoretical estimates are not sufficiently accurate to be used alone in design of multimode interference devices. Instead, analytic approximations provide a starting point for MMI design while BPM simulations offer a more accurate method for determining required length of the multimode waveguide section. We detailed the design process for 1x2 and 2x2 3 dB MMI splitters. We also demonstrated the use of 2x2 MMI as a combiner. Although such device is considerably less compact than a 2x1 MMI combiner, it does not suffer from the same reflections as an 2x1 MMI combiner does when the two inputs are out of phase. Both 1x2 and 2x2 MMIs were shown to be fairly insensitive to the length variations of the multimode section. MMI efficiency remains well within 90% of the maximum value for 10 micron deviation from the optimal MMI length. Imbalance in the 1x2 splitter is extremely small, on the order of 10^{-2}-10^{-3} dB. Imbalance in 2x2 devices is below 0.2 dB. The MMIs display polarization sensitivity, but can be designed to perform sufficiently well for both polarizations.

We determined that moderate underetching of trenches between the pairs of input and output waveguides has nearly no effect on MMI performance. While severe underetching reduces MMI efficiency by only 0.2-0.3 dB, it gives rise to unwanted oscillatory behavior in the output waveguides. We explain this behavior by an interaction of the fundamental mode of the structure with the higher-order modes created due to remaining high-index material in the trench.

5.1.2 Interfaces between passive and active devices

We detailed optimization process for the ATG tapers using BPM method. Efficiency of a taper coupler increases with taper length, with exponential couplers demonstrating an advantage over linear couplers only for a limited intermediate range, 125-175 μm in our case. We argue that efficiency of linear and exponential tapers is nearly identical outside of this intermediate range. The adiabatic condition is easily satisfied in long tapers and is poorly satisfied in short tapers of either shape. Next, we demonstrate that the design of the layered ATG structure is based on a combination of efficiency optimization results and fabrication considerations.

We assessed the effects of possible fabrication defects on coupling efficiency of ATG tapers. It was determined that overetching of the upper ATG ridge does not reduce coupler efficiency noticeably unless the upper ridge is reduced by more than 0.3 μm. The possibility of the thin tip of the taper breaking off is also not a serious threat to coupler performance. When the slope of the linear taper is fixed, coupler efficiency depends primarily on the initial width of the taper. For our design, the most efficient tapers were found to have an initial width of ~0.8 μm. Considering the slope of our taper, this width corresponds to the location approximately one coupling length before the resonance point. Nearly constant efficiency is displayed by the tapers with a smaller tip, while efficiency falls off sharply for tapers starting at width over 0.9 μm. Since it seems unlikely that a taper tip breaks off at such a significant width, the taper break-off does not represent a serious fabrication concern. Finally, we ruled out rotational misalignment of the upper ridge with respect to the lower ridge as a significant threat to taper coupler performance.

We used FDTD with PML to calculate reflections from the ATG taper tip and to compare it to the reflections from a similar butt-coupling interface. A butt-coupled junction between two bulk waveguides of 4 μm x 1.05 μm cross-section with bulk refractive indices of 3.22 and 3.42 represents a limiting case because 3.42 is the highest index of any semiconductor material used in this project. According to our calculations, $R=7.28\text{x}10^{-4}$ for this junction. Reflectivity of a taper tip is expected to be at least several orders of magnitude lower than that of a butt-coupled junction described above. The FDTD simulation yields a reflection $R\sim4\text{x}10^{-5}$, which is on the order of the numeric error of the FDTD implementation used in this project. We also established that reflection coefficient can be accurately estimated based on local effective indices on two sides of the junction. In contrast to FDTD, the effective index method is fast and requires modest computational resources. An estimate based on effective indices yields a reflection $R\sim10^{-7}$. Based on the two sets of calculations, we can confidently conclude that reflections from the taper tip are sufficiently low for a successful operation of an SOA as a single pass device.

5.1.3 Semiconductor Optical Amplifiers

We reviewed the physical basis of the SOA operation and the use of SOAs in linear and non-linear applications. We then proceeded to explore gain and non-linear phase in an SOA as functions of device parameters using a numerical model. Our model of light propagation in an SOA is based on the rate equations for carrier and photon density in the device. Gain is defined parametrically as a function of carrier density and wavelength of light.

To test the model, we produced small signal gain (SSG) curves with respect to wavelength, SOA length, and injection current density. We calculated a gain saturation curve and showed that SOA gain is lowered when optical input power is increased to further demonstrate that our model yields appropriate device behavior.

Dependence of the output saturation power P_{SATout} on confinement factor, SOA length, and injection current density was examined. We found that P_{SATout} decreases with increasing confinement factor, device length, and injection current density. However, these dependences hold only for SOAs which provide up to about 10 dB of small signal gain. The output saturation power for higher-gain SOAs is approximately constant.

We presented an optimization strategy for a linear and a non-linear SOA design using the same semiconductor layer structure. The designed heterostructure is characterized by a large confinement factor chosen in order to achieve required phase shift in non-linear SOAs. The goal of the linear SOA design was to produce a device that yields 4 dB gain for 2 ps, 100 fJ signals at a wavelength of 1550 nm while minimizing bias current. Similarly, a non-linear SOA was to produce phase shift of π for the same input pulse. We clearly demonstrated a tradeoff between SOA length and injection current density for both linear and non-linear devices.

We concluded that linear SOAs should be built by choosing short SOA lengths and moderate injection current densities. A short SOA needs a higher injection current density to produce the required gain, while the total bias current is smaller than that required for longer devices. In addition, a short SOA biased at higher injection current density displays better linearity than a long SOA designed for the same level of gain and biased at lower injection current density. In contrast, non-linear SOAs should be long and operated at moderate injection current densities in order to produce required phase shift while minimizing bias current. We conclude that linear and non-linear SOAs can be optimally operated at similar injection current density levels, provided that non-linear SOAs are significantly longer than linear SOAs.

Based on our analysis of passive components in Chapter 2 and adiabatic taper couplers in Chapter 3, we were able to estimate the total loss suffered by a signal passing through the optical logic unit cell. The overall loss from passive components determines the amount of amplification that has to be supplied by the amplifiers in the circuit. The sources of the loss include the loss in passive ridge waveguides, bending loss in waveguide turns, coupling loss in taper couplers, and loss in MMIs. If the design presented in our work is implemented flawlessly, overall loss from passive components and couplers is estimated to be 7.0 dB. The SOA employed in the circuit as a phase shifter provides 13.9 dB of gain, which is more than sufficient to offset the loss from the passive components. The gain in this nonlinear SOA is still sufficient to offset the circuit loss even if several of the fabrication deficiencies discussed in Chapter 2 and Chapter 3 are present.

5.2 Future directions

The basic implementation of optical logic unit cell does not address the issues of timing, reflections, and separating multiple co-propagating wavelengths. Resolving these issues is crucial for cascadability of individual unit logic cells.

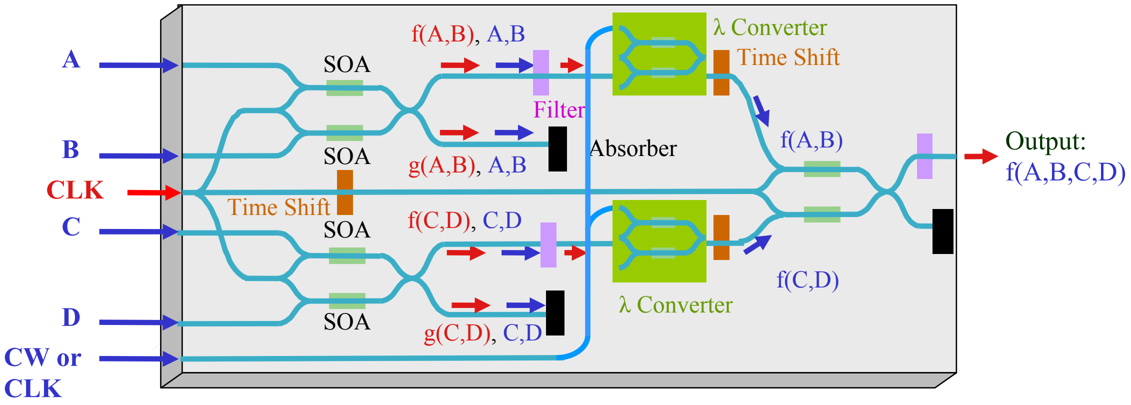

Figure 5-1. Cascading multiple unit cells to perform operation f(A,B,C,D) [49].

Figure 5-1 presents an example of cascading multiple unit cells to perform a multi-stage logic operation [49], such as, for example, (A xor B) xor (C xor D). The circuit consists of three unit cells: 1) f(A, B), 2) f(C, D), and 3) the last stage. In order to operate properly, this optical circuit requires a number of additional devices. The time delays need to be introduced in order to match optical path lengths to control the timing. The filters have to be added to remove unwanted wavelengths, such as those used for clock or control signals. Additionally, the wavelength converters should be employed to resolve ambiguity between the data and the control signals. The absorbers need to be included to eliminate the back reflections into the logic stages. Multiple wavelength clocks/control signals are required for cascading optical logic elements.

Future generations of design and modeling tools for photonic integrated circuit design need to include design libraries containing optical components with standardized input and output characteristics in addition to accurate and robust simulation software. Design methodologies also need to allow the various circuit elements to be connected in clearly specified, predictable ways. Standard circuit designs should take into account the needs of circuit testing and manufacturability.

Near-term efforts should concentrate on developing more sophisticated and effective tools for modeling active device operation. Improved model should include a bi-directional light propagation within the device and an accurate model of amplified spontaneous emission (ASE). For accurate modeling of pulse propagation in the presence of ASE, initial values of carrier and photon densities should be determined by finding a steady state due to ASE in absence of injected signal. The same steady-state values should be used in calculations of nonlinear phase.

Since modeling of passive devices and taper couplers is relatively well-developed, the next round of simulations should be informed by measurements performed on the designed devices. Several goals can be achieved by comparing simulation results with measured values. First of all, reliability of simulation methods can be assessed. Second, measured waveguide losses due to sidewall roughness can be incorporated into the numerical model. Additionally, deviations from intended device dimensions due to variations in fabrication can be evaluated. During our design of the first-generation devices, the fabrication tolerance calculations were based on speculations about likely imperfections in device processing. In designing next generation of devices, the fabrication tolerance calculations can be performed based on measured variations in previously fabricated devices.

Appendix A Optical Logic Unit Cell Heterostructure Design

Layer	Layer Purpose	Thickness	Doping
$In_{0.56}Ga_{0.44}As_{0.93}P_{0.07}$	Contact Layer	50 nm	p-type at > 2 x 10^{18} cm^{-3}
$In_{0.79}Ga_{0.21}As_{0.45}P_{0.55}$		30 nm	p-type at > 1 x 10^{18} cm^{-3}
InP	Ridge	600 nm	p-type Graded: 2.5 x 10^{17} cm^{-3} at the bottom 1 x 10^{18} cm^{-3} at the top
$In_{0.79}Ga_{0.21}As_{0.45}P_{0.55}$	Etch-stop	10 nm	p-type at 2.5 x 10^{17} cm^{-3}
InP		50 nm	p-type at 2.5 x 10^{17} cm^{-3}
InP		50 nm	Undoped
$In_{0.79}Ga_{0.21}As_{0.45}P_{0.55}$	Cladding	100 nm	Undoped
$In_{0.56}Ga_{0.44}As_{0.93}P_{0.07}$	Active	200 nm	Undoped
$In_{0.79}Ga_{0.21}As_{0.45}P_{0.55}$	Cladding	100 nm	Undoped
InP		50 nm	Undoped
InP		150 nm	n-type at 5 x 10^{17} cm^{-3}
$In_{0.79}Ga_{0.21}As_{0.45}P_{0.55}$	Passive Waveguide Quaternary #1	100 nm	n-type at 5 x 10^{17} cm^{-3}
InP		200 nm	n-type at 5 x 10^{17} cm^{-3}
$In_{0.79}Ga_{0.21}As_{0.45}P_{0.55}$	Passive Waveguide Quaternary #2	250 nm	n-type at 5 x 10^{17} cm^{-3}
InP		200 nm	n-type at 5 x 10^{17} cm^{-3}
$In_{0.79}Ga_{0.21}As_{0.45}P_{0.55}$	Passive Waveguide Quaternary #3	100 nm	n-type at 5 x 10^{17} cm^{-3}
InP		200 nm	n-type at 5 x 10^{17} cm^{-3}
InP	Buffer Layer	300 nm	n-type graded: ~substrate level at the bottom 5 x 10^{17} cm^{-3} at the top
InP	SUBSTRATE		n-type at 3-6 x 10^{18} cm^{-3}

Appendix B Design Files for RSoft Simulations

The following pages contain three sample computer aided design (CAD) files used for RSoft BeamPROP simulations. The first file contains the passive ridge waveguide design. The second file contains the 2x2 multimode interference (MMI) structure. The third file is used for asymmetric twin waveguide (ATG) simulations. The comments in these files are preceded by a % sign. The comments have been added for reference and should be removed before running these simulations.

- **Dilute Waveguide**

```
%Parameters are defined

HInP1 = 0.2% InP layer thickness
H_ridge = Hfiber_guide+Hact% ridge height
Hact = 0.2+2*0.1+0.2% SOA thickness, not needed here
Hclad1 = 0.1% InGaAsP layer thickness 1 in dilute WG
Hclad2 = 0.25% InGaAsP layer thickness 2 in dilute WG
Hetstop = 0
Hfiber_guide = 3*HInP1+2*Hclad1+Hclad2+Hspacer+Hetstop% passive WG
thickness
Hspacer = 0
Lin = 100% input WG length
Lmmi = 961/2% MMI length
Lout = 100% output WG length
Lpass = 200
Lsoa = 300
NInP = 3.17% here and below—refractive indices
Nact = 3.45
Nclad = 3.29
Ncon = 3.32
Netstop = 3.25
Phase2 = 0% phase on the 2nd input relative to the 1st input
Wmmi = 18% MMI width
Wpass = 4% passive WG width
alpha = 0% loss coefficient
```

```
background_index = 3.17% substrate index
color_circuit = 15
color_outline = 0
color_scale = spectrum.scl
color_surface = 0
cover_index = 1
delta = 0
dimension = 3
eim = 0
exwidth = 0
exwidth2 = 0
free_space_wavelength = 1.55
grid_size = 0.02
grid_size_y = 0.05
height = 5
index_display_mode = DISPLAY_CONTOURMAPXY
k0 = (2*pi)/free_space_wavelength
launch_file = IQEpass.m00% This file contains fundamental mode of the
passive WG.  Input file is required for running this CAD file.
launch_position = -Wmmi/6%  positions of input and output waveguides of
2x2 MMI
launch_type = LAUNCH_FILE
mode_output_format = OUTPUT_NONE
monitor_step_size = 0.4
p_f = 0% fraction of power in the 2nd input
polarization = 0
profile_type = PROF_STEPINDEX
rate = 1
run_output = 0
slab_height = 0.01
slice_display_mode = DISPLAY_CONTOURMAPXZ
slice_output_format = OUTPUT_NONE
slice_position_y = 0
step_size = 0.4
structure = STRUCT_MULTILAYER
vector = 1
w_gap = 2
width = 4%  default width of a waveguide in this ciruit

%Layer structure is defined below.  The table includes layer heights
and indices.
layer_table 0
      height_1 = HInP1
       index_1 = NInP
      height_2 = Hclad1
       index_2 = Nclad
      height_3 = HInP1
       index_3 = NInP
      height_4 = Hclad2
       index_4 = Nclad
      height_5 = HInP1
       index_5 = NInP
      height_6 = Hclad1
       index_6 = Nclad
      height_7 = Hspacer
       index_7 = NInP
      height_8 = 0.2
```

```
        index_8 = NInP
      height_9 = 0.1
        index_9 = Nclad
      height_10 = 0.2
        index_10 = 3.42
      height_11 = 0.1
        index_11 = Nclad
      height_12 = 0.6
        index_12 = NInP
end layer_table

layer_taper 0
end layer_taper

user_taper 1
end user_taper

scan_info 1
end scan_info

segment 1
      combine_mode = COMBINE_MERGE
      position_taper = TAPER_LINEAR
      begin.x = 0
      begin.z = 0
      begin.height = Hfiber_guide
      end.x = 0
      end.z = 1000
      end.height = Hfiber_guide
end segment

pathway 1
end pathway

monitor 1
end monitor
```

- **2x2 MMI**

```
%Parameters are defined

H1 = HInP1+Hclad1+Hspacer+Hetstop% waveguide height in the trench,
severe underetching
H2 = 2*HInP1+Hclad1+Hclad2+Hspacer+Hetstop% waveguide height in the
trench, moderate underetching
HInP1 = 0.2% InP layer thickness
H_ridge = Hfiber_guide+Hact% ridge height
Hact = 0.2+2*0.1+0.2% SOA thickness, not needed here
Hclad1 = 0.1% InGaAsP layer thickness 1 in dilute WG
Hclad2 = 0.25% InGaAsP layer thickness 2 in dilute WG
Hetstop = 0
Hfiber_guide = 3*HInP1+2*Hclad1+Hclad2+Hspacer+Hetstop% passive WG
thickness
Hspacer = 0
Lin = 100% input WG length
Lmmi = 961/2% MMI length
Lout = 100% output WG length
Lpass = 200
Lsoa = 300
NInP = 3.17% here and below—refractive indices
Nact = 3.45
Nclad = 3.29
Ncon = 3.32
Netstop = 3.25
Phase2 = 0% phase on the 2nd input relative to the 1st input
Wmmi = 18% MMI width
Wpass = 4% passive WG width
alpha = 0% loss coefficient
background_index = 3.17% substrate index
color_circuit = 15
color_outline = 0
color_scale = spectrum.scl
color_surface = 0
cover_index = 1
delta = 0
dimension = 3
eim = 0
exwidth = 0
exwidth2 = 0
free_space_wavelength = 1.55
grid_size = 0.02
grid_size_y = 0.05
height = 5
index_display_mode = DISPLAY_CONTOURMAPXY
k0 = (2*pi)/free_space_wavelength
launch_file = IQEpass.m00% This file contains fundamental mode of the
passive WG.  Input file is required for running this CAD file.
launch_position = -Wmmi/6%  positions of input and output waveguides of
2x2 MMI
launch_type = LAUNCH_FILE
mode_output_format = OUTPUT_NONE
monitor_step_size = 0.4
p_f = 0% fraction of power in the 2nd input
polarization = 0
```

```
profile_type = PROF_STEPINDEX
rate = 1
run_output = 0
slab_height = 0.01
slice_display_mode = DISPLAY_CONTOURMAPXZ
slice_output_format = OUTPUT_NONE
slice_position_y = 0
step_size = 0.4
structure = STRUCT_MULTILAYER
vector = 1
w_gap = 2
width = 4%  default width of a waveguide in this ciruit

%Layer structure is defined below.  The table includes layer heights
and indices.
layer_table 0
      height_1 = HInP1
       index_1 = NInP
      height_2 = Hclad1
       index_2 = Nclad
      height_3 = HInP1
       index_3 = NInP
      height_4 = Hclad2
       index_4 = Nclad
      height_5 = HInP1
       index_5 = NInP
      height_6 = Hclad1
       index_6 = Nclad
      height_7 = Hspacer
       index_7 = NInP
      height_8 = 0.2
       index_8 = NInP
      height_9 = 0.1
       index_9 = Nclad
      height_10 = 0.2
       index_10 = 3.42
      height_11 = 0.1
       index_11 = Nclad
      height_12 = 0.6
       index_12 = NInP
end layer_table

layer_taper 0
end layer_taper

user_taper 1
end user_taper

%This portion of the script allows to vary one of the parameters, here—
Phase2
scan_info 1
      variable = Phase2
      start = 0
      finish = 180
      increment = 60
      scanprefix = Phase2-2
end scan_info
```

```
%This is a scan within the first scan, varying p_f
scan_info 2
      variable = p_f
      start = 0.5
      finish = 0.5
      increment = 0.5
end scan_info

%Lateral device layout is defined in terms of segments
%Output 1
segment 1
      begin.x = -Wmmi/6
      begin.z = 0 rel end segment 7
      begin.height = Hfiber_guide
      end.x = 0 rel begin segment 1
      end.z = Lout rel begin segment 1
      end.height = Hfiber_guide
end segment

%Output 2
segment 2
      begin.x = Wmmi/6
      begin.z = 0 rel end segment 7
      begin.height = Hfiber_guide
      end.x = 0 rel begin segment 2
      end.z = Lout rel begin segment 2
      end.height = Hfiber_guide
end segment

%Input 2
segment 3
      begin.x = Wmmi/6
      begin.z = -Lin
      begin.height = Hfiber_guide
      end.x = 0 rel begin segment 3
      end.z = 0
      end.height = Hfiber_guide
end segment

% Input 1
segment 4
      begin.x = -Wmmi/6
      begin.z = -Lin
      begin.height = Hfiber_guide
      end.x = 0 rel begin segment 4
      end.z = 0
      end.height = Hfiber_guide
end segment

%Channel 1, inactive, needed for defining monitor pathways
segment 5
      profile_type = PROF_INACTIVE
      position_taper = TAPER_LINEAR
      begin.x = -Wmmi/6
      begin.z = 0 rel begin segment 7
      begin.height = Hfiber_guide
```

```
      end.x = 0 rel begin segment 5
      end.z = 0 rel end segment 7
      end.height = Hfiber_guide
end segment

%Channel 2, inactive, needed for defining monitor pathways
segment 6
      profile_type = PROF_INACTIVE
      position_taper = TAPER_LINEAR
      begin.x = Wmmi/6
      begin.z = 0 rel begin segment 7
      begin.height = Hfiber_guide
      end.x = 0 rel begin segment 6
      end.z = 0 rel end segment 7
      end.height = Hfiber_guide
end segment

%Multimode section
segment 7
      begin.x = 0
      begin.z = 0
      begin.height = Hfiber_guide
      begin.width = Wmmi
      end.x = 0 rel begin segment 7
      end.z = Lmmi rel begin segment 7
      end.height = Hfiber_guide
      end.width = Wmmi
end segment

%Material in the output trench due to underetching, height can be 0,
H1, or H2
segment 8
      color = 1
      begin.x = -8.326672685e-017 rel end segment 7
      begin.z = 0 rel end segment 7
      begin.height = 0
      begin.width = w_gap
      end.x = 0 rel begin segment 8
      end.z = Lout rel begin segment 8
      end.height = 0
      end.width = w_gap
end segment

%%Material in the input trench due to underetching, height can be 0,
H1, or H2

segment 9
      color = 1
      begin.x = 0
      begin.z = -Lin
      begin.height = 0
      begin.width = w_gap
      end.x = 0 rel begin segment 7
      end.z = 5
      end.height = 0
      end.width = w_gap
end segment
```

```
%Each pathway consists of an input WG, output WG, and channel inside
the MMI section between the input and output WGs.  Pathways are used
for monitoring energy.
pathway 1
      4
      5
      1
end pathway

pathway 2
      2
      6
      3
end pathway

%Monitor 1 keeps track of total power in computational window
monitor 1
      pathway = 1
      monitor_type = MONITOR_TOTAL_POWER
      monitor_tilt = 0
      monitor_mode = 0
      monitor_file = IQEpass.m00
end monitor

%Monitor 2 keeps track of power in output waveguide 1
monitor 2
      pathway = 1
      monitor_type = MONITOR_FILE_POWER
      monitor_tilt = 0
      monitor_mode = 0
      monitor_file = IQEpass.m00
end monitor

%Monitor 3 keeps track of power in output waveguide 2

monitor 3
      pathway = 2
      monitor_type = MONITOR_FILE_POWER
      monitor_tilt = 0
      monitor_mode = 0
      monitor_file = IQEpass.m00
end monitor

%Fundamental mode of the passive WG is launched into input 1 at -Wmmi/6
launch_field 1
      launch_pathway = 1
      launch_type = LAUNCH_FILE
      launch_tilt = 0
      launch_mode = 0
      launch_mode_radial = 1
      launch_position = -Wmmi/6
      launch_file = IQEpass.m00
end launch_field

%Fundamental mode of the passive WG is launched into input 2 at Wmmi/6
```

```
%The input is scaled by a factor of p_f and has a relative phase of
Phase2 with respect to input 1
launch_field 2
      launch_pathway = 2
      launch_type = LAUNCH_FILE
      launch_tilt = 0
      launch_mode = 0
      launch_mode_radial = 1
      launch_position = Wmmi/6
      launch_file = IQEpass.m00
      launch_power = p_f
      launch_phase = Phase2
end launch_field
```

- **ATG**

```
%Parameters are defined

HInP1 = 0.2% InP layer thickness
H_ridge = Hfiber_guide+Hact% ridge height
Hact = 0.2+2*0.1+0.1% SOA thickness
Hcap = 0.7 %cap layer thickness
Hclad1 = 0.1% InGaAsP layer thickness 1 in dilute WG
Hclad2 = 0.25% InGaAsP layer thickness 2 in dilute WG
Hetstop = 0
Hfiber_guide = 3*HInP1+2*Hclad1+Hclad2+Hspacer+Hetstop% passive WG
thickness
Hsoa = H_ridge+Hact %height of SOA ridge, without the cap—for triple
ridge design only
Hspacer = 0
Lflare = Ltapertotal/1.75 %length of the flair on the passive WG
Lflare2 = 40 %alternative value of flair length
Lpass = 200
Lsoa = 300 %SOA length
Ltaper = 0 %in two-section tapers, length of the 1st section
Ltaper2 = Ltapertotal-Ltaper %in two-section tapers, length of the 2nd
section
Ltapertotal = 175 %total taper length
%refractive indices of materials
NInP = 3.17
Nact = 3.45
Nclad = 3.29
Wmidtaper = 0.5+0.005*Ltaper %in two-section tapers, width of the taper
at the point where the two sections meet
Wpass = 4 %passive WG width
Wsoa = 2 %width of the middle ridge
alpha = 0 %waveguide loss coefficient
background_index = 3.17% substrate index
boundary_max = 6
boundary_min = -6
color_outline = 0
color_scale = spectrum.scl
color_surface = 0
cover_index = 1
delta = 0 % upper taper width reduction
dimension = 3
domain_max = Ltapertotal+100
domain_min = -20
eim = 0
exwidth = 0
exwidth2 = 0
farfield_output = 1
field_output_format = OUTPUT_REAL_IMAG_3D
free_space_wavelength = 1.55
grid_size = 0.05
grid_size_y = 0.05
height = 5
index_display_mode = DISPLAY_CONTOURMAPXY
k0 = (2*pi)/free_space_wavelength
launch_file = IQEpass.m00
launch_type = LAUNCH_FILE
```

```
mode_output_format = OUTPUT_REAL_IMAG_3D
monitor_output = 0
polarization = 0
profile_type = PROF_STEPINDEX
rate = 1
run_output = 0
slab_height = 0.01
slice_display_mode = DISPLAY_CONTOURMAPYZ
slice_output_format = OUTPUT_REAL_IMAG_3D
slice_position_y = 3.5
structure = STRUCT_MULTILAYER
vector = 1
width = 4 %default WG width
width_active = 8 %active region ridge width in triple-ridge design
z1 = 0 % Length of the missing tip of a taper

%Layer structure is defined below.  The table includes layer heights
and indices.
layer_table 0
      height_1 = HInP1
       index_1 = NInP
      height_2 = Hclad1
       index_2 = Nclad
      height_3 = HInP1
       index_3 = NInP
      height_4 = Hclad2
       index_4 = Nclad
      height_5 = HInP1
       index_5 = NInP
      height_6 = Hclad1
       index_6 = Nclad
      height_7 = Hspacer
       index_7 = NInP
      height_8 = 0.2
       index_8 = NInP
      height_9 = 0.1
       index_9 = 3.29
      height_10 = 0.2
       index_10 = 3.42
      height_11 = 0.1
       index_11 = 3.29
      height_12 = Hcap
       index_12 = NInP
      height_13 = 0
       index_13 = 3.29
      height_14 = 0
       index_14 = 3.42
end layer_table

layer_taper 0
end layer_taper

%The following lines allows us to simulate tapers of arbitrary shape,
here—parabolic ones
user_taper 1
      type = UF_EXPRESSION
      expression = 1.5*z^2
```

```
end user_taper

%This portion of the script allows to vary one of the parameters, here—
z1
scan_info 1
      variable = z1
      start = 0
      finish = 175
      increment = 5
      scanprefix = break5
end scan_info

%Lateral device layout is defined in terms of segments
%Long passive WG, the two ends serve as input and output of the circuit
segment 1
      combine_mode = COMBINE_MERGE
      position_taper = TAPER_LINEAR
      begin.x = 0
      begin.z = -200
      begin.height = Hfiber_guide
      end.x = 0
      end.z = Ltapertotal*2+Lsoa+100
      end.height = Hfiber_guide
end segment

%Middle ridge, SOA layers without a cap
segment 2
      color = 2
      position_taper = TAPER_LINEAR
      width_taper = TAPER_EXPONENTIAL
      begin.x = 0
      begin.z = Ltapertotal
      begin.height = Hsoa
      begin.width = Wsoa
      end.x = 0
      end.z = Ltapertotal+Lsoa
      end.height = Hsoa
      end.width = Wsoa
end segment

%This segment currently does not serve any purpose.  Possible ridge for
contacts.
segment 3
      combine_mode = COMBINE_MERGE
      position_taper = TAPER_LINEAR
      width_taper = TAPER_LINEAR
      begin.x = 0
      begin.z = Ltapertotal
      begin.height = Hfiber_guide
      begin.width = 8.5+delta
      end.x = 0
      end.z = Ltapertotal+Lsoa
      end.height = Hfiber_guide
      end.width = 8.5+delta
end segment

%Second flair on the passive WG, “down” flair
```

```
segment 4
      combine_mode = COMBINE_MERGE
      position_taper = TAPER_LINEAR
      width_taper = TAPER_LINEAR
      begin.x = 0
      begin.z = Ltapertotal+Lsoa
      begin.height = Hfiber_guide
      begin.width = 6
      end.x = 0
      end.z = Ltapertotal+Lsoa+Lflare
      end.height = Hfiber_guide
      end.width = 4
end segment

%Top ridge containing SOA and cap layers
segment 5
      color = 2
      position_taper = TAPER_LINEAR
      width_taper = TAPER_EXPONENTIAL
      begin.x = 0
      begin.z = Ltapertotal
      begin.height = H_ridge
      begin.width = Wsoa+delta
      end.x = 0
      end.z = Ltapertotal+Lsoa
      end.height = H_ridge
      end.width = Wsoa+delta
end segment

%This segment is redundant in double-ridge design.
segment 6
      color = 14
      position_taper = TAPER_LINEAR
      width_taper = TAPER_LINEAR
      begin.x = 0
      begin.z = Ltapertotal
      begin.height = Hsoa
      begin.width = Wsoa+delta
      end.x = 0
      end.z = Ltapertotal+Lsoa
      end.height = Hsoa
      end.width = Wsoa+delta
end segment

%First flair on the passive WG, “up” flair
segment 7
      position_taper = TAPER_LINEAR
      width_taper = TAPER_LINEAR
      begin.x = 0
      begin.z = Ltapertotal-Lflare
      begin.height = Hfiber_guide
      begin.width = 4
      end.x = 0
      end.z = Ltapertotal
      end.height = Hfiber_guide
      end.width = 6
end segment
```

```
%Taper “up”:  for single-section taper, this is the entire taper; in
double-taper design, this is the “thick” section of the taper
segment 8
      color = 14
      width_taper = TAPER_LINEAR
      begin.x = 0
      begin.z = Ltaper+z1
      begin.height = Hsoa
      begin.width = Wmidtaper+delta+(Wsoa-Wmidtaper)/175*z1
      end.x = 0
      end.z = Ltapertotal
      end.height = Hsoa
      end.width = Wsoa+delta
end segment

%This is the first (thin) section of the “up” taper in two-section
design; inactive in one-taper design
segment 9
      profile_type = PROF_INACTIVE
      combine_mode = COMBINE_MERGE
      color = 14
      width_taper = TAPER_LINEAR
      begin.x = 0
      begin.z = 0
      begin.height = Hsoa
      begin.width = 0.5+delta-0.5
      end.x = 0
      end.z = Ltaper
      end.height = Hsoa
      end.width = Wmidtaper+delta
end segment

%Taper “down”:  for single-section taper, this is the entire taper; in
double-taper design, this is the “thick” section of the taper
segment 10
      color = 14
      width_taper = TAPER_LINEAR
      begin.x = 0
      begin.z = Ltapertotal+Lsoa
      begin.height = Hsoa
      begin.width = Wsoa+delta
      end.x = 0
      end.z = Ltapertotal+Lsoa+Ltaper2
      end.height = Hsoa
      end.width = Wmidtaper+delta
end segment

%This is the second (thin) section of the “down” taper in two-section
design; inactive in one-taper design
segment 11
      profile_type = PROF_INACTIVE
      color = 14
      position_taper = TAPER_LINEAR
      width_taper = TAPER_LINEAR
      begin.x = 0
      begin.z = Ltapertotal+Lsoa+Ltaper2
```

```
      begin.height = Hsoa
      begin.width = Wmidtaper+delta
      end.x = 0
      end.z = 2*Ltapertotal+Lsoa
      end.height = Hsoa
      end.width = 0.5+delta
end segment

%The pathway for monitors
pathway 1
      1
      7
      5
      9
      10
      11
      4
      6
      8
end pathway

%This monitor keeps track of total power in computational window
monitor 1
      pathway = 1
      monitor_type = MONITOR_TOTAL_POWER
      monitor_tilt = 0
      monitor_mode = 0
end monitor

%This monitor keeps track of power in the fundamental mode of the
passive WG
monitor 2
      pathway = 1
      monitor_type = MONITOR_FILE_POWER
      monitor_tilt = 0
      monitor_mode = 0
      monitor_file = IQEpass.m00
end monitor

%This monitor keeps track of power in the fundamental mode of the full-
width ATG
monitor 3
      pathway = 1
      monitor_type = MONITOR_FILE_POWER
      monitor_tilt = 0
      monitor_mode = 0
      monitor_file = IQEact.m00
end monitor
```

Appendix C MATLAB Programs

The following pages provide the MATLAB code for modeling of semiconductor optical amplifiers.

- run_simulation.m

```
%This script calculates gain and nonlinear phase for a specific set of
%device parameters.  vary_parameter.m allows to perform parameter scans
and
%produce plots of gain and phase as a function of a parameter.
%
%This script makes a provision for two input pulses at two distinct
%wavelength.  The script also has a provision for up to five ASE
%components, currently spaced by 10 nm in the range between 1540 nm and
%1580 nm.  Note, however, that such handling of ASE is inaccurate.

% Only one non-zero pulse should be present for each wavelength.  Use
% delays as appropriate to offset the pulses.
% wavelengths and times of impulses:
light_impulse_params.lambda(1) = 1550e-9; %1528e-9; % wavelength in m
light_impulse_params.time1(1) = 2e-12; % duration of the first impulse
(which is assumed to start at t=0)
light_impulse_params.time2(1) = 2e-12; % duration of the second impulse
(which turnes on after specified delay)
light_impulse_params.delay(1) = 25e-12;% delay between two impulses
% power of impulses:
light_impulse_params.amp1(1) = 0.05; % power of the first impulse in
watts;
light_impulse_params.amp2(1) =0; % power of the second impulse in
watts;
% second wavelength...
light_impulse_params.lambda(2) = 1560e-9; %1528e-9; % wavelength in m
light_impulse_params.time1(2) = 2e-12; % duration of the first impulse
(which is assumed to start at t=0)
light_impulse_params.time2(2) = 2e-12; % duration of the second impulse
(which turnes on after specified delay)
light_impulse_params.delay(2) = 0;% delay between two impulses
% power of impulses:
light_impulse_params.amp1(2) = 0;% power of the first impulse in watts;
light_impulse_params.amp2(2) =0;% power of the second impulse in watts;
```

```
%ASE components
light_impulse_params.lambda(3) = 1540e-9;
light_impulse_params.lambda(4) = 1550e-9;
light_impulse_params.lambda(5) = 1560e-9;
light_impulse_params.lambda(6) = 1570e-9;
light_impulse_params.lambda(7) = 1580e-9;

for i=3:7
   light_impulse_params.time1(i) = 0;
   light_impulse_params.time2(i) = 0;
   light_impulse_params.delay(i) = 0;
   light_impulse_params.amp1(i) = 0;
   light_impulse_params.amp2(i) =0;
end;

% triggers to take into account ASE for corresponding wavelengths:
light_impulse_params.account_for_ASE(1) = false;
light_impulse_params.account_for_ASE(2) = false;
for i=3:7
    light_impulse_params.account_for_ASE(i) = false;
end;

% SOA parameters
SOA_params.gamma = 0.4;  % transverse confinement factor
SOA_params.ng = 3.42; % index of refraction
SOA_params.vg = 299792458/SOA_params.ng; % photon group speed in the
medium (cw is the phase speed)
SOA_params.Lx = 0.85e-3;%   % length of the SOA, in m
SOA_params.Ly = 2e-6;   % 2 um width
SOA_params.Lz = 0.2e-6;  % 0.2 um depth of active region, in m; gamma
is linearly proportional to Lz; scale if varying gamma
SOA_params.beta = 0.0004; % spontaneos emission factor (1e-4 to 1e-5
according to Coldren/Corzine, page 444)
SOA_params.alpha_i = 1330; % internal loss, in m^-1
SOA_params.eta = 0.74;  % internal quantum efficiency
SOA_params.A = 1e5;     % nonradiative recombination rate, in 1/s
SOA_params.B = 1e-16;   % bimolecular recombination coefficient in
m^3/s, Coldren/Corzine, page 31
SOA_params.C = 8e-41;   % Auger recombination rate in m^6/s,
Coldren/Corzine, page 159
SOA_params.Ntr = 1.28e24;
SOA_params.I = 6e7;   % bias current DENSITY in A/m^2
SOA_params.g0 = 320000; % if wavelength-independent gain model is used
SOA_params.InputLoss = 0;%-1.7833; % input loss, measured in dB

SOA_params.epsilon_tot = 4.5e-23; %1/m^3
SOA_params.epsilon_ch = 3e-23;
SOA_params.alpha_ch = 1.0;

%------------------------ parameters specific for phase computation ---
----
%from Lorenzo Occhi, Semiconductor Optical Amplifiers Made of Ridge
Waveguide Bulk InGaAsP/InP:
%Experimental Characterisation and Numerical Modelling of Gain, Phase,
and Noise. 2002,
%Eidgenössische Technische Hochschule Zürich
% alpha parameter values:
```

```
SOA_params.alpha_N0 = 5.7;
SOA_params.alpha_N1 = 1.56;
SOA_params.alpha_N2 = 17*1e6;       %   1/m
SOA_params.alpha_N3 = 3e-25;        %   1/m^3
SOA_params.lambda_0 = 1582e-9;      %   band edge wavelength, m
SOA_params.b_0 = 2e-26*1e-6;        %   parameter for lambda_p
calculation, m^4;
SOA_params.N_0 =1.28e24;            %   transparency carrier density at
the lambda_0 wavelength
SOA_params.lambda_z0 = 1660e-9;     %
SOA_params.z0 = -2.5e-27*1e-6;
SOA_params.a0 = 2.75e-20;

npts = 1000; % discretization by x:
time = [0:1e-13:2.5e-11]; % times for which we want to find values of
outputs: [starting time:step:END time]
%   **********   NOTE: Time of the phase computation is the END time
********
%if you change time step, also change lines 102-103
(total_input_energy(i)=sum(input)*1e-13; etc)
% calling the main routine
[input, output, N_shadow, distr_N, distr_S, time] =
calculate_soa_impulse(light_impulse_params, SOA_params, npts, time);

% extract the last timestep's S:
S_last = distr_S(end,:);
S_last_column_wise = reshape(S_last', npts, []);
% computing the phase shift corresponding to the variations to N only
phase = compute_phase(N_shadow, distr_N(end, :), SOA_params,
light_impulse_params.lambda, S_last_column_wise)

total_input_energy=sum(input)*1e-13 % energy in input pulse; 1e-13 is
timestep
total_output_energy=sum(output)*1e-13 % energy in output pulse

input_dBm=10*log10(total_input_energy/2e-15) % input power in dBm
output_dBm=10*log10(total_output_energy/2e-15) % output power in dBm

amplification=total_output_energy./total_input_energy % amplification
amplification_dB=10*log10(amplification) % amplification in dB

% plot graphs...
PLOT_IN_OUT=1; % set PLOT_IN_OUT to 0 to suppress output and input
plots

if ( PLOT_IN_OUT == 1)
figure;
plot(time, input, 'LineWidth', 3);
set(gca, 'FontSize', 16);
title('Input signal');
xlabel('Time, s');
ylabel('Power, watts');

figure;
plot(time, output, 'r-', 'LineWidth', 3);
set(gca, 'FontSize', 16);
title('Output signal');
```

```
xlabel('Time, s');
ylabel('Power, watts');
end;

phase

% movie generation...

CREATE_MOVIE = 1; % turn this to zero if you do not want to create a
movie

dx = SOA_params.Lx/npts;
speed_of_movie = 1;
if (CREATE_MOVIE == 1)
    fprintf('Generating the movie sequence...\n');
    % Now we'll generate an animation
    figure;
    for f=1:length(time)/speed_of_movie
        ind_of_time = speed_of_movie*f;
        subplot(2,1,1);
        plot([dx:dx:SOA_params.Lx], distr_N(ind_of_time, :),
'LineWidth', 2);
        axis([0 SOA_params.Lx 0 max(max(distr_N))]);
        title(strcat('Carrier density, time=',
num2str(time(ind_of_time)), 's'));
        subplot(2,1,2);
        plot([dx:dx:SOA_params.Lx], reshape(distr_S(ind_of_time, :),
npts, [])', 'LineWidth', 2);
        axis([0 SOA_params.Lx 0 max(max(distr_S))]);
        title(strcat('Photon density, time=',
num2str(time(ind_of_time)), 's'));
        xlabel('Length along SOA, m')
        M(:,f) = getframe(gcf);
    end
    delete(gcf);

    % uncomment the following lines to save the movie file
    % disp('saving movie to avi file')
    % Create a title axis to play the movie in
    %movie2avi(M,'result1.avi','compression','Indeo5');
end
```

- vary_parameter.m

```
% Script for varying one of the parameters and plotting graphs of phase
and
% amplification versus the chosen parameter.

phase = [];
amplification = [];
max_output_power = [];
I = NaN;
Lx = NaN;
amp1 = NaN;
gamma = NaN;
lambda = NaN;

% the following are nominal values. Disregard the nominal value of the
parameter which we are
% varying below
%-------------------------------------------------------------------
% times of impulses:
% wavelengths and times of impulses:
light_impulse_params.lambda(1) = 1550e-9; %1528e-9; % wavelength in m
light_impulse_params.time1(1) = 2e-12; % duration of the first impulse
(which is assumed to start at t=0)
light_impulse_params.time2(1) = 2.00e-12; % duration of the second
impulse (which turnes on after specified delay)
light_impulse_params.delay(1) = 0;%25.01e-12; % delay between two
impulses
% power of impulses:
light_impulse_params.amp1(1) =0.05;%1;%1e-6; % power of the first
impulse in watts;
light_impulse_params.amp2(1) =0; % power of the second impulse in
watts;

% triggers to take into account ASE for corresponding wavelengths:
light_impulse_params.account_for_ASE(1) = false;

% SOA parameters
SOA_params.gamma = 0.4;  % transverse confinement factor
SOA_params.ng = 3.42; % index of refraction
SOA_params.vg = 299792458/SOA_params.ng; % photon group speed in the
medium (cw is the phase speed)
SOA_params.Lx = 0.85e-3;%   % length of the SOA, in m
SOA_params.Ly = 2e-6;   % 2 um width
SOA_params.Lz = 0.2e-6;  % 0.2 um depth of active region, in m; gamma
is linearly proportional to Lz; scale if varying gamma
SOA_params.beta = 0.0004; % spontaneos emission factor (1e-4 to 1e-5
according to Coldren/Corzine, page 444)
SOA_params.alpha_i = 1330; % internal loss, in m^-1
SOA_params.eta = 0.74;  % internal quantum efficiency
SOA_params.A = 1e5;     % nonradiative recombination rate, in 1/s
SOA_params.B = 1e-16;   % bimolecular recombination coefficient in
m^3/s, Coldren/Corzine, page 31
SOA_params.C = 8e-41;   % Auger recombination rate in m^6/s,
Coldren/Corzine, page 159
SOA_params.Ntr = 1.28e24;
```

```
SOA_params.I = 6e7;   % bias current DENSITY in A/m^2
SOA_params.g0 = 320000; % if wavelength-independent gain model is used
SOA_params.InputLoss = 0;%-1.7833; % input loss, measured in dB

SOA_params.epsilon_tot = 4.5e-23; %1/m^3
SOA_params.epsilon_ch = 3e-23;
SOA_params.alpha_ch = 1.0;

%------------------------ parameters specific for phase computation ---
----
%from Lorenzo Occhi, Semiconductor Optical Amplifiers Made of Ridge
Waveguide Bulk InGaAsP/InP:
%Experimental Characterisation and Numerical Modelling of Gain, Phase,
and Noise. 2002,
%Eidgenössische Technische Hochschule Zürich
% alpha parameter values:
SOA_params.alpha_N0 = 5.7;
SOA_params.alpha_N1 = 1.56;
SOA_params.alpha_N2 = 17*1e6;       %   1/m
SOA_params.alpha_N3 = 3e-25;        %   1/m^3
SOA_params.lambda_0 = 1582e-9;      %   band edge wavelength, m
SOA_params.b_0 = 2e-26*1e-6;        %   parameter for lambda_p
calculation, m^4;
SOA_params.N_0 =1.28e24;            %   transparency carrier density at
the lambda_0 wavelength
SOA_params.lambda_z0 = 1660e-9;     %
SOA_params.z0 = -2.5e-27*1e-6;
SOA_params.a0 = 2.75e-20;

npts = 1000; % discretization by x:
time = [0:1e-13:2e-11]; % times for which we want to find values of
outputs: [starting time:step:END time]
%if you change time step, also change lines 134-135
(total_input_energy(i)=sum(input)*1e-13 etc.)
%   **********   NOTE: Time of the phase computation is the END time
********

%********************** uncomment / comment here lines depending on
what you are varying *******************
% span of parameters we want to calculate in the format
% first_value:step:last_value
% gamma = 0.08:0.005:0.12; % if you vary gamma. Lz = gamma/2e6!
%Lx = 0.25e-3:0.25e-3:1.5e-3; % if you vary length
%I = 1.5e7:1.5e7:15e7; % if you vary current density
I = 3e7:1e7:7e7; % in this example we vary current density
%amp1 = 0.05:0.025:0.1; % if you vary amplitude (power) of input signal
%amp1 = logspace(-9, 0, 10); % if you vary amplitude (power) and want a
logarithmic distribution of points
%lambda = 1480e-9:20e-9:1600e-9; % if you vary lambda

%The following section of the code recognized which parameter we are
varying
if (~isnan(gamma))
    prm = gamma;
    str = '\Gamma';
    case_switch = 1;
elseif(~isnan(Lx))
```

```
    prm = Lx;
    str = 'Length of the SOA, m';
    case_switch = 2;
elseif(~isnan(I))
    prm = I;
    str = 'Injection Current Density, A/m^2';
    case_switch = 3;
elseif(~isnan(lambda))
    prm = lambda;
    str = 'Wavelength, m';
    case_switch = 4;
elseif(~isnan(amp1))
    prm = amp1;
    str = 'Input power, Watts';
    case_switch = 5;
end;

if (isnan(gamma))
    gamma = SOA_params.gamma.*ones(size(prm)); end;
if (isnan(Lx))
    Lx = SOA_params.Lx.*ones(size(prm)); end;
if (isnan(I))
    I = SOA_params.I.*ones(size(prm)); end;
if (isnan(lambda))
    lambda = light_impulse_params.lambda.*ones(size(prm)); end;
if (isnan(amp1))
    amp1 = light_impulse_params.amp1.*ones(size(prm)); end;

for i=1:length(prm)

    SOA_params.gamma = gamma(i);
    SOA_params.Lx = Lx(i);
    SOA_params.I = I(i);

    %SOA_params.Lz = SOA_params.gamma/2e6; %uncomment this line if
varying gamma

    light_impulse_params.amp1 = amp1(i);
    light_impulse_params.lambda = lambda(i);

    % calling the main routine
    [input, output, N_shadow, distr_N, distr_S, time] =
calculate_soa_impulse(light_impulse_params, SOA_params, npts, time);

    % computing the phase shift corresponding to the variations to N
only
    phase(i) = compute_phase(N_shadow, distr_N(end, :), SOA_params,
light_impulse_params.lambda, distr_S(end,:)');

    total_input_energy(i)=sum(input)*1e-13; % energy in the input
pulse, 1e-13 is time step
    total_output_energy(i)=sum(output)*1e-13; % energy in the output
pulse
    amplification(i)=total_output_energy(i)/total_input_energy(i); %
amplification
    amplification_dB(i)=10*log10(amplification(i)); % amplification in
dB
```

```
end;

%*** plotting phase vs parameter
figure;
plot(prm, phase,'c-','LineWidth', 2);
title(strcat('Dependence of the phase on the ', str));
ylabel('Phase difference, radians');
xlabel(str);

%%%%% plot gain vs. parameter
figure;
plot(prm, amplification_dB,'-m');
title(strcat('Gain vs. ', str));
ylabel('Gain, dB');
xlabel(str)

% to produce a gain saturation curve when varying amplitude (input
power)
% plot gain vs output power
%figure;
%semilogx(total_output_energy/light_impulse_params.time1(1),
amplification_dB,'c-','LineWidth', 2);
%title(['Gain vs Output Power', str]);
%ylabel('Gain, dB');
%xlabel('Output power, W');
```

- calculate_soa_impulse.m

```
% solver for the time-dependence of the output of the SOA.

function [input, output, N_shadow, distr_N, distr_S, time] =
calculate_soa_impulse(light_params, SOA_params, npts, time, N_distr)

% npts - number of discretization points by x
% time - times for which we want to evaluate our system.

% It's assumed that the first signal (#1) starts at time zero.  The 2nd
pulse starts after time_delay.
%
% N_distr - optional argument, if it is provided, this is an initial
% concentration of the carriers

% outputs:
% - input light amplitude (watts)
% - output light amplitude (watts)
% - distributions of carriers and photons
% - time samples, corresponding to these distributions (seconds)

% fundamental constants
c=299792458; % speed of light in vacuum, in m/s
h=6.6262e-34; % Planck's constant in Js
q=1.602e-19;   % absolute value of the electron charge in C

% parsing from the parameters
gamma = SOA_params.gamma;
lambdas = light_params.lambda;
Ly = SOA_params.Ly;
Lz = SOA_params.Lz;
vg = SOA_params.vg;
Lx = SOA_params.Lx;
beta = SOA_params.beta;
alpha_i = SOA_params.alpha_i;
eta = SOA_params.eta;
ng = SOA_params.ng;
A = SOA_params.A;
B = SOA_params.B;
C = SOA_params.C;
Ntr = SOA_params.Ntr;
I = SOA_params.I;
InputLoss = SOA_params.InputLoss;

dx=Lx/npts; % step in space
EPs =h.*c./light_params.lambda;
n_lambdas = length(light_params.lambda);

% calculating the initial carrier concentration. We assume the SOA
before
% the impulse to be fully inversely populated. This population is
goverened
% by the rates of injection and recombination.

% solving equation a0 - AN - BN^2 - CN^3 = 0
```

```
a0 = I*eta/(q*Lz);
N_shadow = a0/A;
while (abs(a0 - A*N_shadow - B*N_shadow^2 - C*N_shadow^3) > a0*1e-13)
    deriv = -A - 2*B*N_shadow - 3*C*N_shadow^2;
    N_shadow = N_shadow - (a0 - A*N_shadow - B*N_shadow^2 -
C*N_shadow^3)/deriv;
end;

% Now we have initial condition: N(x)=N_shadow. Fix the zero time.

% N_shadow
if (~exist('N_distr'))
    N = N_shadow*ones(npts,1);
else
    N = N_distr;
end;

S = zeros(n_lambdas*npts,1);

options = odeset('AbsTol', 1e10);
[time, distr] = ode45(@eval_time_deriv, time, [N; S], options,
light_params, SOA_params);

distr_N = distr(:,1:npts);
distr_S = distr(:,npts+1:end); %serialized...
out_S = distr_S(:,npts-1:npts:end); % time points x n_lambdas
output = (out_S*diag(EPs./gamma)).*(Lz*Ly*vg);

% forming input vector
for i_lambda = 1:n_lambdas
    input(i_lambda,1:length(time)) =
light_params.amp1(i_lambda).*(reshape(time, 1,[]) <
light_params.time1(i_lambda)) + ...
    light_params.amp2(i_lambda).*(reshape(time, 1,[]) >
light_params.delay(i_lambda) & reshape(time, 1,[]) <
light_params.delay(i_lambda) + light_params.time2(i_lambda));
end;

input = input';
```

- eval_time_deriv.m

```
function dfdt = eval_time_deriv(t, x, light_params, SOA_params)

% % fundamental constants
c=299792458; % speed of light in vacuum, in m/s
h=6.6262e-34; % planck constant in Js
q=1.602e-19;   % absolute value of the electron charge in C

gamma = SOA_params.gamma;
lambdas = light_params.lambda;
Ly = SOA_params.Ly;
Lz = SOA_params.Lz;
vg = SOA_params.vg;
Lx = SOA_params.Lx;
beta = SOA_params.beta;
alpha_i = SOA_params.alpha_i;
eta = SOA_params.eta;
ng = SOA_params.ng;
A = SOA_params.A;
B = SOA_params.B;
C = SOA_params.C;
Ntr = SOA_params.Ntr;
I = SOA_params.I;
g0 = SOA_params.g0;
InputLoss = SOA_params.InputLoss;

EPs =h.*c./light_params.lambda;

%*****extra parameters for wavelength-dependent gain
alpha_N0 = SOA_params.alpha_N0;
alpha_N1 = SOA_params.alpha_N1;
alpha_N2 = SOA_params.alpha_N2;
alpha_N3 = SOA_params.alpha_N3;
lambda_0 = SOA_params.lambda_0;
b_0 = SOA_params.b_0;
N_0 = SOA_params.N_0;
lambda_z0 = SOA_params.lambda_z0;
z0 = SOA_params.z0;
a0 = SOA_params.a0;
epsilon_tot=SOA_params.epsilon_tot;
%********end of extra parameters for wavelength-dependent gain
% ---------------- end of SOA parameters ----------------------------%

n_of_ASE = sum(light_params.account_for_ASE);
n_lambdas = length(light_params.lambda);

npts = floor(size(x,1)/(1 + n_lambdas));
dx=Lx/npts;
N = x(1:npts);
S = x(npts+1:end);

%input loss
amp1_after_losses = light_params.amp1.*10^(InputLoss/10);
amp2_after_losses = light_params.amp2.*10^(InputLoss/10);
```

```
%carrier concentration at the beginning of the channel
S_0 = zeros(n_lambdas,1);
% adding first impulse
for i_lambda = 1:n_lambdas
    if (t < light_params.time1(i_lambda))
        S_0(i_lambda,1) = S_0(i_lambda,1) +
gamma*amp1_after_losses(i_lambda)/(EPs(i_lambda)*(Ly*Lz*vg));
    end;
    % adding second impulse
    if (t > light_params.delay(i_lambda) && t <
light_params.delay(i_lambda) + light_params.time2(i_lambda))
        S_0(i_lambda,1) = S_0(i_lambda,1) +
gamma*amp2_after_losses(i_lambda)/(EPs(i_lambda).*(Ly*Lz*vg));
    end;
end;

% ***********************

% for each section dx:
lambda_z = lambda_z0 - z0.*(N - N_0);
lambda_p = lambda_0 - b_0.*(N - N_0);
gp = a0.*(N - N_0);
c_N = 3.*(gp./(lambda_z - lambda_p).^2);
d_N = 2.*(gp./(lambda_z - lambda_p).^3);

gm = zeros(npts,n_lambdas);
for i_lambda = 1:n_lambdas
    ind = find(lambdas(i_lambda) < lambda_z);
    gm(ind,i_lambda) = c_N(ind).*(lambdas(i_lambda) - lambda_z(ind)).^2
+ d_N(ind).*(lambdas(i_lambda) - lambda_z(ind)).^3;
end;
% ************************

% evaluating the derivative dx/dt...
S_col_wise = reshape(S, npts, n_lambdas);
S_prev = [S_0'; S_col_wise(1:end-1,:)];

dNdt = I*eta/(q*Lz) - (A.*N + B.*N.^2 + C.*N.^3) -
sum(vg.*(gm.*S_col_wise)./(1 + epsilon_tot.*S_col_wise),2);
for i_lambda = 1:n_lambdas
    % NOTE: last term is responsible for ASE
    % The ability of this script to handle ASE is limited, especially
in cases of multiple
    % spectral components of ASE is limited because the coefficient
beta/n_of_ASE is inaccurate.

    if (light_params.account_for_ASE(i_lambda))
        dSdt((i_lambda-1)*npts+1:i_lambda*npts,1) =
vg*(S_prev(:,i_lambda) - S_col_wise(:,i_lambda))./dx -
alpha_i*vg*S_col_wise(:,i_lambda) +
gamma*vg.*gm(:,i_lambda).*S_col_wise(:,i_lambda)./(1 +
epsilon_tot.*S_col_wise(:,i_lambda)) + gamma*beta*B.*(N.^2)./n_of_ASE;
    else
        dSdt((i_lambda-1)*npts+1:i_lambda*npts,1) =
vg*(S_prev(:,i_lambda) - S_col_wise(:,i_lambda))./dx -
alpha_i*vg*S_col_wise(:,i_lambda) +
```

```
gamma*vg.*gm(:,i_lambda).*S_col_wise(:,i_lambda)./(1 +
epsilon_tot.*S_col_wise(:,i_lambda));
    end;
end;
dfdt = [dNdt; dSdt];
```

- compute_phase.m

```
function phis = compute_phase(N_shadow, N, SOA_params, lambdas,
S_column_wise)

% computing phase resulting from distribution of carriers (N)
% and photons (S) along SOA

% % fundamental constants
c=299792458; % speed of light in vacuum, in m/s
h=6.6262e-34; % planck constant in Js
q=1.602e-19;   % absolute value of the electron charge in C

gamma = SOA_params.gamma;
Ly = SOA_params.Ly;
Lz = SOA_params.Lz;
vg = SOA_params.vg;
Lx = SOA_params.Lx;
beta = SOA_params.beta;
alpha_i = SOA_params.alpha_i;
eta = SOA_params.eta;
ng = SOA_params.ng;
A = SOA_params.A;
B = SOA_params.B;
C = SOA_params.C;
Ntr = SOA_params.Ntr;
I = SOA_params.I;
g0 = SOA_params.g0;
InputLoss = SOA_params.InputLoss;

n_lambdas = length(lambdas);

EPs =h*c./lambdas;

% additional parameters for phase computation...
alpha_N0 = SOA_params.alpha_N0;
alpha_N1 = SOA_params.alpha_N1;
alpha_N2 = SOA_params.alpha_N2;
alpha_N3 = SOA_params.alpha_N3;
alpha_ch = SOA_params.alpha_ch;
epsilon_ch = SOA_params.epsilon_ch;
epsilon_tot = SOA_params.epsilon_tot;
lambda_0 = SOA_params.lambda_0;
b_0 = SOA_params.b_0;
N_0 = SOA_params.N_0;
lambda_z0 = SOA_params.lambda_z0;
z0 = SOA_params.z0;
a0 = SOA_params.a0;

% ---------------- end of SOA parameters ----------------------------%
npts = length(N);
dx=Lx/npts;

% reference N:
N_ref=N_shadow;
```

```
% alpha_ref:
lambda_p_ref = lambda_0 - b_0*(N_ref - N_0);

for i_lambda = 1:n_lambdas

    lambda = lambdas(i_lambda);
    alpha = alpha_N0 + alpha_N1*exp(alpha_N2*(lambda - lambda_p_ref) +
alpha_N3*(N_ref - N_0));

    % gm_ref computation...
    lambda_z = lambda_z0 - z0*(N_ref - N_0);
    lambda_p = lambda_0 - b_0*(N_ref - N_0);
    gp = a0*(N_ref - N_0);
    c_N = 3*(gp/(lambda_z - lambda_p)^2);
    d_N = 2*(gp/(lambda_z - lambda_p)^3);
    if (lambda < lambda_z)
        gm_ref = c_N*(lambda - lambda_z)^2 + d_N*(lambda - lambda_z)^3;
    else
        gm_ref = 0;
    end;

    phi = 0;
    phi_x=zeros(npts,1);
    phi_x_total=zeros(npts,1);

    % for each section dx:
    for i = 1:npts

        % wavelength-dependent gain model:
        lambda_z = lambda_z0 - z0*(N(i) - N_0);
        lambda_p = lambda_0 - b_0*(N(i) - N_0);
        gp = a0*(N(i) - N_0);
        c_N = 3*(gp/(lambda_z - lambda_p)^2);
        d_N = 2*(gp/(lambda_z - lambda_p)^3);
        if (lambda < lambda_z)
            gm = c_N*(lambda - lambda_z)^2 + d_N*(lambda - lambda_z)^3;
        else
            gm = 0;
        end;
        phi_x_total(i)=phi;
        phi_x(i)=- 0.5*dx*alpha*gamma*(gm - gm_ref); %phase per dx

        phi = phi - 0.5*dx*alpha*gamma*(gm - gm_ref); %total phase

        % adding the last term of the phase formula:

        phi = phi +
0.5*dx*alpha_ch*epsilon_ch*sum(S_column_wise(i,:))*gm/(1 +
epsilon_tot*sum(    S_column_wise(i,:)));
    end;
    phis(i_lambda) = phi;
end;

    % plots to visualize how the phase is accumulated along the SOA
length
    PLOT_PHASE=0; % PLOT_PHASE=1 if plots are desired
    if (PLOT_PHASE == 1)
```

```
  figure;
        subplot(3,1,1);
        plot([dx:dx:Lx], N, 'LineWidth', 2);
     %   axis([0 Lx 0 max(N)]);
       title('Carrier density');
    %  title(strcat('Carrier density, length=', num2str(Lx*1e6),
'um'));
       subplot(3,1,2);
        plot([dx:dx:Lx], phi_x, 'r-', 'LineWidth', 2);
      % axis([0 Lx 0 max(phi_x)]);
        title('phase per dx');
        subplot(3,1,3);
        plot([dx:dx:Lx], phi_x_total, 'g-', 'LineWidth', 2);
  %      axis([0 Lx 0 max(phi_x_total)]);
        title('total phase');
        xlabel('Length along SOA, m')
    end
```